Ana Elisa Fernandes Oliveira

Bachelor of Science in Biomedical Engineering

An innovative wearable device to evaluate motor symptoms during deep brain stimulation surgery

Dissertation submitted in partial fulfilment of the requirements for the degree of

Master of Science in
Biomedical Engineering

Coordinator: Prof. Dr. João Paulo Cunha, Associate Professor at FEUP and Senior Researcher at INESC TEC

Co-coordinator: Prof. Dr. Pedro Vieira, Associate Professor at FCT-UNL

FACULDADE DE CIÊNCIAS E TECNOLOGIA
UNIVERSIDADE NOVA DE LISBOA

September, 2019

An innovative wearable device to evaluate motor symptoms during deep brain stimulation surgery

Acknowledgements

I would like to start by thanking Professor Doutor João Paulo Cunha for the opportunity he has given me to be part of the BRAIN group, and in particular, the chance of contributing to such a special project, as the iHandU project. I want to acknowledge your time, dedication and your wise advice during this master thesis.

Also, to all the BRAIN members, for integrating me so well in the group. To Vítor, not only for your technical support during this project, but also for your friendship. And to Erwan, for all the lunches, the talks, the laughs and of course for the patience to teach me!

A very special and massive gratitude to Duarte. For all your time, patience, availability and will to teach me. For all your great advices and for always pushing me to my best. I am pretty sure that, without your help, my way would be one billion times harder! As I always say, thank you Duarte!

To our student hall group. For all the things we have been through together. In special, to Tomás, despite only meeting you a year ago, our friendship is important to me and I truly appreciate your effort in keeping it.

To Letícia, my best friend! Four and a half years sharing the same room, the courses, the activities, the experiences, the laughs and the cries. With us, it is all about sharing! Thank you, my sweet girl, only after you I started to believe in friendship.

To my lovely boyfriend, Tiago. Thank you for being the best, for loving me and for always being by my side, no matter what. For being the person who makes me laugh the most and for always saying the words that comfort me. To me you are the one and you will always be.

Last but not least, I own a truly acknowledgment to my family. To my grandmother for being my role model. To my parents, who are capable of doing everything for me and for my siblings. Thank you for believing in me and for having the special gift of making me feel better in any situation. And to my brother and sister, two of the most important people in the world to me! To Nandinho, for elevating my concept of love to another level and to Carolina, for being with me since birth and for always protecting me.

Abstract

The technological advancement observed over the past few years and the increasingly interest of the overall population in this field explains the arising of wearable devices, which provide an extensive list of advantages for their users in different areas. In the healthcare field, wearable systems are being used for personal health monitoring, sports performance improvement or as support diagnostic tool. In particular, the BRAIN group from INESCTEC developed a wearable system, named iHandU, which provides a real time quantitative evaluation of rigidity changes during Deep Brain Stimulation (DBS) surgeries.

The iHandU system is intended for patients with movement neurological disorders. The system is based on an algorithm that quantifies the improvement of rigidity during DBS surgeries, helping doctors to define stimulation sites and parameters. The main input of the referred algorithm is the gyroscope data of the patient's hand during the movement of symptoms evaluation. This data is achieved through a wearable device placed on the patient's hand, which, beside other components, includes an inertial sensor.

The main goal of this master thesis was to enhance the iHandU system hardware. So, force sensors were added to measure the force doctors make in patient's hand during the symptoms evaluation, since this variable can influence the quantification results. Furthermore, older components were replaced by low power and smaller size ones, by what the system firmware was also remade. In addition, a web application for data visualization and reproducibility tests of the inertial data provided by the produced devices was tested. In addition, a follow-up of the development of a band textile, where the hardware will be placed during surgery, was also conducted during this master thesis.

In the end, these goals were successfully achieved and a new improved version of the iHandU system hardware was obtained. Moreover, it is believed that this new system is better prepared to be introduced in the wearable health devices market.

Keywords: Wearable Health Devices; Deep Brain Stimulation; Microelectronics; PCB Design; Firmware; Bluetooth Low Energy.

Resumo

O avanço tecnológico observado nos últimos anos e o interesse cada vez maior da população nesta área explica o aparecimento dos dispositivos vestíveis, que fornecem uma extensa lista de vantagens para os seus utilizadores em diferentes áreas. Na área da saúde, os sistemas vestíveis são aplicados para monitorização pessoal, para medida da melhoria do desempenho desportivo e como ferramenta de suporte para o diagnóstico. Posto isto, o grupo BRAIN, pertencente ao INESCTEC, desenvolveu um sistema vestível, chamado iHandU, que fornece uma avaliação quantitativa, em tempo real, da variação da rigidez durante cirurgias de Estimulação Cerebral Profunda (ECP).

O sistema iHandU destina-se a pacientes com doenças neurológicas de movimento. O sistema baseia-se num algoritmo que quantifica a melhoria de sintomas motores durante a cirurgia de ECP, auxiliando os médicos a definir os locais e parâmetros de estimulação. O principal parâmetro de entrada do referido algoritmo são os dados do giroscópio retirados aquando o movimento da mão do paciente durante a avaliação dos sintomas. Estes dados são alcançados através de um dispositivo vestível colocado na mão do paciente, que, entre outros componentes, inclui um sensor inercial.

O principal objetivo desta tese de mestrado foi melhorar o *hardware* do sistema iHandU. Assim, foram adicionados sensores de força para medir a força exercida pelos médicos na mão do paciente durante a avaliação dos sintomas, uma vez que este parâmetro pode influenciar os resultados da quantificação. Para além disso, os componentes antigos foram substituídos por uns mais avançados e menores em dimensão e em consumo, pelo que o *firmware* do sistema foi também refeito. Foi ainda desenvolvida uma aplicação web para visualizar os dados e foi testada a reprodutibilidade dos dispositivos construídos. Adicionalmente, foi também acompanhado o desenvolvimento de uma banda têxtil onde o *hardware* será colocado durante a cirurgia.

No final, estes objetivos foram alcançados com sucesso, obtendo-se uma versão melhorada do dispositivo iHandU. Posto isto, acredita-se que este novo dispositivo está melhor preparado para ser introduzido no mercado dos dipositivos vestíveis para a saúde.

Termos-chave: Dispositivos Vestíveis para a Saúde; Estimulação Profunda do Cérebro; Microeletrónica; Desenho de PCB; Firmware; Bluetooth Low Energy.

Contents

List of Figures

List of Tables

Abbreviations

ASUR	Autonomous Sensing Unit Recorder
BOM	Bill Of Materials
BRAIN	Biomedical Research And Innovation
BLE	Bluetooth Low Energy
BAN	Body Area Network
BFCS	Body-Fixed Coordinate System
CA	Capacity Ampere
C-BER	Centre for Biomedical Engineering Research
CCD	Charge Coupled Device
CPHA	Clock Phase
CPOL	Clock Polarity
SCLK	Clock Signal
CSV	Comma Separated Values
CAD	Computer-Aided Design
CS	Coordinate System
CVG	Coriolis Vibrating Gyroscopes
CSPTC	Cortico-Striato-Pallido-Thalamocortical
DBS	Deep Brain Stimulation
DoF	Degrees of Freedom
HHb	Deoxygenated Haemoglobin
EFCS	Earth-Fixed Coordinate System
EMG	Electromyography
EMBS	Engineering in Medicine and Biology Society
ET	Essential Tremor
FOS	Fibre Optic Sensors
FBG	Fibre Bragg Grating

FPCB	Flexible Printed Circuit Board
FSR	Force Sensing Resistors
GAP	Generic Access Profile
GATT	Generic Attribute Profile
GPi	Globus Palidus pars internus
IMU	Inertial Motion Units
INESC-TEC	Instituto de Engenharia de Sistemas e Computadores – Tecnologia e Ciência
IDE	Integrated Development Environment
I^2C	Inter-Integrated Circuit
KPF	Knitted Piezoresistive Fabrics
LED	Light-Emitting Diode
LP	Low Pass
MISO	Master In-Slave Out
MOSI	Master Out-Slave In
MCU	Microcontroller Unit
MEMS	Micro-Electromechanical System
MoMo	Motion Mote
NIRS	Near-Infrared Spectroscopy
NED	North-East-Down
O_2Hb	Oxygenated Haemoglobin
PD	Parkinson's disease
PDMS	Polydimethylsiloxane
PET	Polyethylene Terephthalate
PVC	Polyvinyl Chloride
PU-Cu	Polyurethane-coated Copper
PU	Portable Unit
PCB	Printed Circuit Board
RF	Radiofrequency
SCL	Serial Clock

SDA	Serial Data
SPI	Serial Peripheral Interface
SAS	Simpson-Angus Scale
AgNW	Silver Nanowires
SSn	Slave Select Signal
STN	Sub-Thalamic Nucleus
SVM	Support Vector Machine
sEMG	Surface Electromyography
TETRAS	The Essential Tremor Assessment Scale
TFG	Tuning Fork Gyroscope
UPDRS	Unified Parkinson's Disease Rating System
UART	Universal Asynchronous Receiver and Transmitter
USB	Universal Serial Bus
USART	Universal Synchronous-Asynchronous Receiver and Transmitter
UUID	Universally Unique Identifier
VIM	Ventralis Intermedius Nucleus
WD	Wearable Device
WHD	Wearable Health Device
WHS	Wearable Health System
WS	Wearable System

1

1 Introduction

The use of Wearable Devices (WDs) have been increasing with the technological advancement. These gadgets show great results in a wide range of applications: from industry, to entertainment, until healthcare and many other fields. In particular, WDs have been increasingly implemented in the healthcare area, being called as Wearable Health Devices (WHD). Indeed, healthcare specialists and engineers joined together with the aim of responding to difficulties arising in this field.

This master thesis was developed in the Biomedical Research and Innovation (BRAIN) group of the Center for Biomedical Engineering Research (C-BER), at Instituto de Engenharia de Sistemas e Computadores – Tecnologia e Ciência (INESC-TEC), under the supervision of Eng. Dr. João Paulo Cunha in cooperation with the Functional Surgery and Movement Disorders Unit of Hospital S. João, Porto, Portugal. The aim of this project is to create a small and cutting-edge WHD to be implemented in an existing system that responds to the difficulty of quantifying motor symptoms improvements during Deep Brain Stimulation (DBS) surgeries.

Therefore, this introductory chapter is divided in four topics that will provide a better understanding of this thesis contextualization, motivation and objectives. The last topic describes how the current document is organized.

1.1 Background and Context

Deep Brain Stimulation (DBS) consists in a relatively recent and effective therapy to alleviate proper symptoms of not only movement related disorders, but also neurobehavioral disorders, epilepsy and pain management. Patients suffering from movement disorders exhibit similar symptoms, amongst which, the most common are movement rigidity, tremor and bradykinesia. Due to their high prevalence in the patients, these symptoms are frequently evaluated to infer about the stage/progression of the disorder. [1]

Treatment procedures to alleviate the symptoms consist either on medication or stimulation of specific deep sites of the brain through DBS surgery. Indeed, DBS surgery has been showing

great results in alleviating rigidity, tremor and bradykinesia, improving patients' quality of life. During the surgery, the correct placement of the electrodes into the brain and its configuration for stimulation (further explained in detail) have huge impact on the improvement of the referred symptoms. Therefore, the evaluation of the referred motor symptoms during the surgery are of major importance. Their improvement will reflect the optimal place of the electrodes and the best settings combination. [1] In clinical environment, patients must be awake during the DBS surgery to perform specific movements which will allow to conclude the degree of rigidity, tremor or bradykinesia. Then, clinicians resort to qualitative scales and, based on their perception, they attribute a score to the performed movement. This subjective method is susceptible to errors and therefore, a lack of consistence is verified among different clinicians. [2] Thus, the problematic situation here is that a quantitative and reliable method to evaluate the level of improvement of these symptoms has yet to be developed.

Having this into account, new methods to quantify the improvement of the referred movements would be really helpful in the evaluation of the effectiveness of DBS surgery. Despite the efforts from the scientific community to build a quantitative method for this purpose, it is not known the existence of a system capable of giving an accurate quantitative score of each one of these symptoms improvement during the surgery. For this reason, Eng. Pedro Costa, ex-member of the BRAIN group together with the Professor João Paulo Cunha, have initiated the iHandU system. This system consists in a device able to track hand kinematics, whose signals are transmitted to a smartphone, where an algorithm returns a quantification of the above mentioned symptoms improvement. The iHandU system was further improved by Engª. Sofia Assis and Elodie Lopes. In fact, their efforts resulted not only in published papers [3-5] but also in a patented method for measuring wrist rigidity during DBS surgery [6].

Even so, further improvements on the system are needed, especially at the hardware level. Hence, the aim of this master thesis will be the construction of a completely new WD for the iHandU system. A new miniaturized hardware will be integrated in the system with the already designed symptoms improvement quantification algorithms to achieve a more comfortable, surgical adapted and cutting-edge system to be used during DBS surgery.

1.2 Motivation

Currently, the subjective assessment of the rigidity, tremor and bradykinesia reduction during and after DBS surgery consists in an unreliable and inconsistent evaluation method. The existing iHandU system came to solve this problem with high accuracy. In fact, it has been revealed to be a very useful tool as diagnostic support during DBS surgeries, participating in the improvement of the life quality of movement disorder patients.

What needed to be improved on the existing iHandU system was its physical component. In general, along this master thesis, the hardware of the system was renewed with more advanced

technology. Thus, it was required not only knowledge from the healthcare field as also electronic concepts had to be present. Learning and applying electronic concepts that were not so developed during my university course was a challenge, however there were several factors about this project that made me take the risk. A very attractive one was the fact of the iHandU system gave rise to a spin-off, thus prooving its potential to successfully achieve the healthcare market and make the difference in neurological movement patients live. Also the possibility to obtain a close contact with a textile company and learn all about how textiles are produced, the cares they must obey to be used in surgical environments and how they can integrate electronics had a high influence on my decision. Moreover, in my opinion, at the end of an academic way / begin of a professional career is always advantageous to explore different areas and acquire new knowledges, to better know myself and my capacities and decide which way I want to follow in the future. I also believe that this project can provide me valuable skills and confidence to dive in the world of work, being of my personal and professional interest to learn new methodologies and, together with other ones acquired during the course, apply them in such an innovative project.

To conclude, allying technology to health is one of the purposes of Biomedical Engineers and, with this master thesis, is being given one more step to reach this purpose.

1.3 Objectives

The existing iHandU system has shown great results in rigidity evaluation during DBS surgery, mainly of Parkinson's disease patients, at the Functional Surgery and Movement Disorders Unit of Hospital S. João, Porto, Portugal. However, the system hardware needed to be improved. Without compromising the required efficiency, it was of utmost importance to evolve the wearable into a more comfortable and technological advanced device. For this reason, this project focused on the miniaturization, redesign and system components update, as well as the integration of novel technologies, such as Bluetooth Low Energy. These improvements led to a smaller size wearable device capable of tracking hand kinematics with very low power consumption. Hand kinematics is tracked by an inertial sensor integrated in the device, so, to assure the accuracy of the inertial data, the performance of reproducibility tests for the inertial sensors was also aimed in this master thesis.

Furthermore, the aim of force sensors integration had the purpose of measuring the force made by the clinician on the patient's hand during rigidity assessment, once it is believed that it may influence the obtained results of improvement. In partnership with a textile company and with the ideas of a BRAIN member (Eng. Duarte Dias), it was also followed the development of a new textile band, where the hardware will be included, guaranteeing usability of the WD. The final goal consisted in the integration of the developed device with the iHandU existing system to be used during DBS surgeries, replacing the nowadays outdated wearable.

1.4 Contributions of this work

Until now, the improvements of the existing iHandU system were made to obtain better algorithms that would lead to the achievement of symptoms improvements evaluations with higher accuracies. Moreover, improvements to the mobile app for clinicians' interaction have also been made. With that being said, the main ambition of this thesis was to improve a specific part of the overall system that had not been yet enhanced: the hardware part. The size of the existing hardware and the fact that it is attached to an uncomfortable and not adapted textile band wrapped around the patient's hand have been a problem in the performed clinical trials. Actually, the requirements related to the use of the system in the operating room had not yet been considered.

In response to these flaws, small electronics, comprising an advanced IMU, a microcontroller unit (MCU) and a Bluetooth Low Energy (BLE) module, for low power consumption, welded in a miniaturized printed circuit board (PCB), together with a battery, replaced the system hardware. A smaller device will ensure the patient's comfort during this so delicate surgery. In addition, reproducibility tests of the inertial data provided by the developed WD were made.

Another accomplished challenge was the incorporation of the system hardware in an improved textile, which development had into account the clinicians' feedback. The development of the textile was based on the ideas of a BRAIN member (Eng. Duarte Dias) and it occurred in parallel with this thesis, where it was only followed the evolution of the referred band. Furthermore, the contribution of a textile company provided the best textile to both system incorporation and its use in the operating room.

Finally, both healthcare specialists and BRAIN members also detected the need for an evaluation of the force made by the clinicians during the symptoms evaluation in DBS surgery. For this reason, force sensors were included in the system hardware to test if more accurate results of rigidity quantification will be obtained.

1.5 Document Structure

This master thesis is divided in six chapters organized in a chronological way according to the tasks performed during the full project development.

The beginning of second chapter, has focus on concepts related with DBS therapy. In detail, this chapter studies the course of the DBS surgery, the most typical movement neurological disorders for which the therapy is frequently applied and the movement symptoms that DBS is able to improve. Hence, a revision of the literature about how the referred symptoms improvement are assessed during DBS surgery is presented. Furthermore, since these symptoms are related with the hand kinematics, a research of scientific projects tracking hand kinematics was also

included in the state of art. To conclude, the end of this second chapter describes in detail the existing iHandU system.

The third chapter consists in a description of mainly hardware related concepts, allowing to understand not only in what Wearable Health Systems (WHSs) consist but also to be aware of what WDs tracking hand kinematics must generally comprise and how they can be built. Specifically, in this chapter, an overview the general architecture of a WHS is firstly presented. Furthermore, an overview of WDs incorporation in textiles is also discussed, since it was important for understanding the integration of the developed hardware in the textile band. The third chapter also elucidates in what a micro Inertial Measurement Unit (IMU) consists, since a sensor of this kind was implemented in the new IHandU device to obtain measurements of the hand kinematics. Furthermore, possible digital communication protocols to be used between electronic sensors and a Microcontroller Unit (MCU) and between the MCU and a Bluetooth Low Energy (BLE) module were also discussed. By last, an analysis of Computer-Aided Design software is made, which was used for projecting the circuits of the developed device.

Chapter four corresponds to the description of the development phase of the project. It starts by showing the architecture of the WS where the developed device is integrated and a detailed comparative analysis of the considered electronic components to implement in the device. This is followed by an explanation of the performed Hardware and Firmware development. Still in this chapter, the integration of the produced hardware in the textile band is explained. Then, a developed web application enabling data visualization and recording is presented. To finish, the methodology performed to make reproducibility tests on the achieved two units of the new iHandU device are described.

The results and respective discussion of the project achievements is made on the fifth chapter. Here the developed device is tested at different levels. First, some of the problems that emerged during the Hardware development are revealed and justified. Then, an analysis in terms of developed device power consumption and total cost is made. Moreover, the reproducibility tests results of the inertial data provided by the device sensors are presented. And finally, at the end of this chapter a presentation of the achieved system in this master thesis project is made.

The sixth and last chapter of this master thesis includes the conclusions about the project, as also some suggestions of possible improvements to be made in the future, with the aim of commercializing the developed system.

In addition, this master thesis document contains four annexes. The first annex presents all the needed documentation for reproduce the device developed in this project, including hardware and firmware details. The second annex, in turn, describes the protocol to perform the inertial data reproducibility tests. Finally, the two last annexes, which are confidential, are related with the performed and future developments of the textile band.

2

2 State of Art

Deep Brain Stimulation is a recent and complex therapy suitable to a panoply of neurologic disorders. Furthermore, it comprises a series of important biological and technological concepts that must be known before advancing a solution for the problem to be solved in the scope of this master thesis. Therefore, a first division of this chapter, 2.1, focus on the concepts related to Deep Bain Stimulation Therapy, such as movement related pathologies and methods to assess their respective symptoms, as well as scientific works developed in this area. In 2.2, an overview about the existing iHandU system is made allowing to understand the progression of the system until the moment, its scientific and commercial achievements and its flaws.

2.1 Deep Brain Stimulation Therapy

As mentioned before, Deep Brain Stimulation (DBS) therapy is not only effective for movement disorders, such as Parkinson Disease (PD) and Essential Tremor (ET), but it also presents very good results in a panoply of neurobehavioral and psychiatric diseases. [7]

In this master thesis, the focus is on the effectiveness of DBS surgery in movement disorders symptoms only. Therefore, after a detailed description of the treatment in 2.1.1, including the surgery details, the two most common movement disorders for which DBS is effective are discussed in 2.1.2. For these disorders, DBS surgery alleviates mainly rigidity, tremor and bradykinesia symptoms. Hence, in 2.1.3 a better understanding of these symptoms, their assessment methods during surgical procedures and related scientific projects developed by researchers are given. To deepen the research of other possible techniques to assess the aforementioned symptoms, a generic analysis of scientific projects tracking hand kinematics in 2.1.4 is made. Still in this topic, an investigation about developed projects for force tracking is also performed, since it is believed that this variable may have impact in the symptoms improvement quantification.

2.1.1 Fundamentals

Deep Brain Stimulation involves an invasive neurosurgical procedure with actuation in neural circuits, more specifically in cortico-striato-pallido-thalamocortical (CSPTC) loops. These circuits are related with limbic, associative and motor function, where each one of these are connected to a specific area of the striatum. Therefore, a malfunction on one of these loops will lead to a bad communication between the circuit nodes, resulting in serious disabling symptoms, such as tremor, rigidity and bradykinesia. [7] The comparison of the motor circuit of a healthy subject with the one of a Parkinson's Disease patient is represented in Figure 2.1.

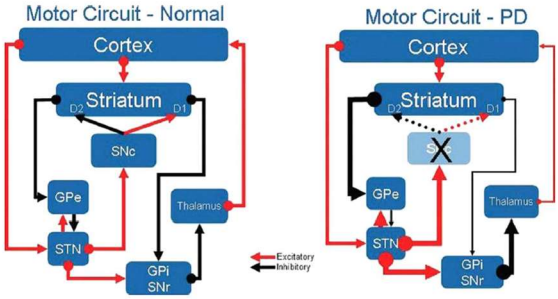

Figure 2.1 - Motor circuits representation. A) In a healthy subject. B) In a patient with Parkinson's disease (neurologic disorder with resort to DBS therapy). [7]

The nodes of the circuit are the target for DBS, which commonly are the sub-thalamic nucleus (STN), the globus palidus pars internus (GPi) and also the ventralis intermedius nucleus (VIM). The choice of the target varies according to the patients' symptoms and imaging examinations. [7] A relation between the target sites and the effective treatment of the symptoms is shown in Table 2.1.

Table 2.1 - Relation of the DBS surgery targets with the relief of the symptoms. Adapted from [1]

DBS site	*Effect of therapy*
Ventralis Intermedius Nucleus	Reduces tremor.
Globus pallidus	Reduces tremor, rigidity, bradykinesia.
Subthalamic nucleus	Reduces tremor, rigidity, bradykinesia.

During DBS surgery, leads, i.e. wires with small electrodes, are inserted into the deep brain target. The leads can be placed in just one side of the brain, unilateral leads (Figure 2.2A) or in both sides, bilateral leads (Figure 2.2B). Once implanted, the leads are attached to a wire extension enabling its connection with a pulse generator, which also can be single-chamber, if connected to one lead (Figure 2.2A) or dual-chamber, if connected to two leads (Figure 2.2B). The pulse generator provides electrical pulses to the leads. In turn, the leads deliver electrical signals on the above referred deep targets, regularizing brain signalling in the affected circuits. Finally, this electrical stimulation promotes the relieving of the symptoms. [1]

Parameters like current intensity values and pulse width and frequency can be changed in the pulse generator during the surgery. The variation of these parameters will interfere directly in the shape of the stimulation field, and therefore improve or worsen the rigid, trembling or bradykinesia movements. Actually, it takes a considerable amount of time to reach the optimal settings combination to achieve the maximum well-being of the patient. [1] The neurostimulators used at the Functional Surgery and Movement Disorders Unit of Hospital S. João, Porto, Portugal, are provided by the Medtronic Company and represented in Figure 2.2C.

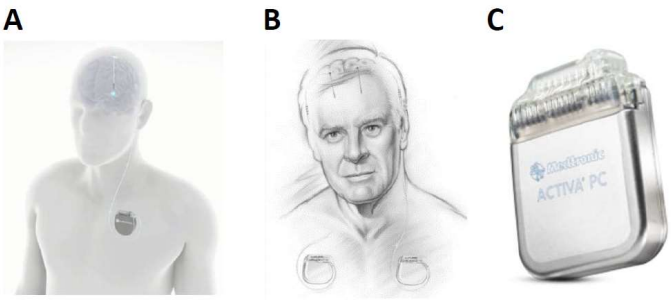

Figure 2.2 - Chamber pulse generator. A) Single chamber with unilateral DBS leads. B) Bilateral chamber with bilateral DBS leads. [1] C) Dual-channel device capable of delivering bilateral stimulation constructed at Medtronic Company. [8]

In conclusion**,** what differentiates DBS from other treatments, besides its good results, is the fact of it being potentially reversible, causing minimal or any damage to the brain tissue. Moreover, the adjustment of the settings, enables a continuous control of the symptoms as well as the expression of the possible side effects. [1]

2.1.2 Pathologies

According to what was said about DBS therapy in the previous chapter, it is a fact that this procedure has a huge potential. Indeed, DBS has being successful in several neurological movement disorders which present a considerable incidence on the worldwide population, as is mentioned in the following two topics.

Among several examples, DBS has been playing an important role in the symptomatic improvement of Parkinson Disease and Essential Tremor patients. Thus, in the following topics, these two movement disorders will be explained and contextualized.

2.1.2.1 Parkinson Disease

Parkinson disease (PD) takes second place of the most common degenerative diseases of the central nervous system with a prevalence that increases with age, affecting 1% of the worldwide population over 60 years old. [9]

Its etiology is still unknown, however researchers defend that it may be related with ageing and with the relation between genetics and environmental factors. [10] At the pathophysiological level, patients with PD show a progressive loss of dopamine neurons (Figure 2.3).

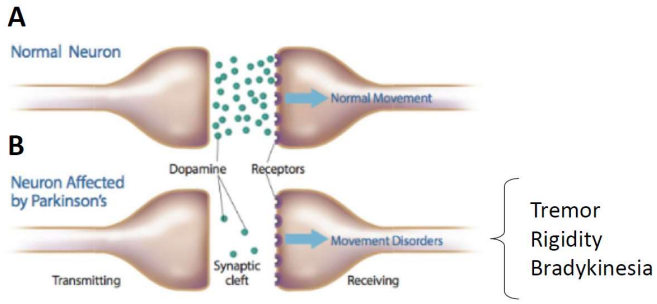

Figure 2.3 - Dopamine release in A) Healthy subject and B) PD patient. Adapted from [11].

Dopamine neurons are located in the substantia nigra region, in the basal ganglia. These neurons are responsible for movement regulation. The latter is achieved by controlling the direct and indirect pathways in the basal ganglia. The direct pathway results in the activation of the thalamus, which sends signals to the cortex**,** then sent to the brainstem and finally to the muscles. The indirect pathway results in the inhibition of the thalamus, thus inhibiting the movement. The role of dopamine neurons is to control the activation of these two pathways in a way that a balance between excitation and inhibition is reached. This balance is achieved because dopamine in substantia nigra can link to two different receptors: one that stimulates the direct pathway and thus the movement, and other that, through the stimulation of the indirect pathway, inhibits the movement. [12] Hence, the lack of dopamine causes movement deregulation in patients with PD.

The three primary symptoms of PD are tremor, rigidity and bradykinesia. However, the presence of additional motor and non-motor features, described in Table 2.2 are common. The PD diagnose is based on clinical features, neurologic evaluation, medical history and in the presence of two out of the three primary symptoms referred above. Besides clinical signs and symptoms, the positive response to antiparkinsonian drugs confirms the presence of this pathology. Moreover imaging techniques like Magnetic Resonance Imaging, Positrons Emission Tomography and Single Photon Emission Computed Tomography can be performed, mainly to exclude other causes, or to differentiate PD with dissimilar origins. [13]

Table 2.2 – Motor and Non-motor Symptoms of PD. [10, 13]

Motor Symptoms	Non-motor Symptoms
Cog wheeling	Constipation
Difficulty in initiating movement	Depression
Hypokinisia	Olfactory impairment
Microphagia	Sleep disturbance

Hypophonia	Dysphagia
Gait and balance difficulties	Dementia and hallucinations

Up until now, there is not a known cure for PD. Therefore, only the use of therapy aims to soften the symptoms or delay the disease progression. The possible treatments can be divided into dopaminergic medications, like levodopa, and surgical therapies, such as DBS surgery, where the target is the STN (Figure 2.4). The appropriated therapy differs from patient to patient, depending strongly on the patient's age and disease progression. [2, 13, 14]

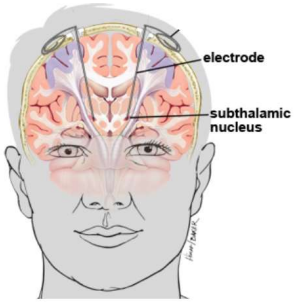

Figure 2.4 - Electrode positioned in the sub-thalamic nucleus for DBS surgery. Adapted from[15].

In the scope of this pathology, the quantification of the most symptoms, including rigidity, tremor and bradykinesia, is performed using a subjective scale called the Unified Parkinson's Disease Rating System (UPDRS). This scale evaluates the level of the symptoms in five qualitative levels. [16] Despite its frequent use, UPDRS depends on the clinician experience and perception. Consequently, not only the resolution for detecting small changes in the mentioned symptoms is lost but also there is no general agreement between different clinicians. These difficulties raise the need of quantifying the symptoms' improvement in different contexts of the patients' life. [2, 14] Particularly, an impartial and quantitative scale would be helpful during Deep Brain Stimulation surgery for discriminating rigidity, tremor and bradykinesia enhancements due to stimulation.

2.1.2.2 Essential Tremor

Essential Tremor (ET) is a very common movement disorder, having a prevalence of 4.6% in worldwide population over 65 years old. It is characterized by a kinetic and/or postural tremor affecting mainly the upper limbs, but also the head, vocal cords, trunk, legs and face. Other neurological findings like bradykinesia, ocular movements, gait ataxia and difficulties in hand-eye coordination are present in these patients. [17]

Despite not existing evidences of inheritance, this syndrome has a strong familial linkage. Therefore, the diagnostic implies a revision to the family history and a careful examination of the observable findings. [18]

The pathophysiology of ET is still unclear. However it is known an increased cerebellar activity. In fact, through electrophysiological and imaging techniques, a coherent oscillation of the cortico-olivo-cerebello-thalamic circuit (Figure 2.5) with respect to the ongoing tremor oscillation was found. What remains unclear is the process behind the circuit's oscillation.[19, 20]

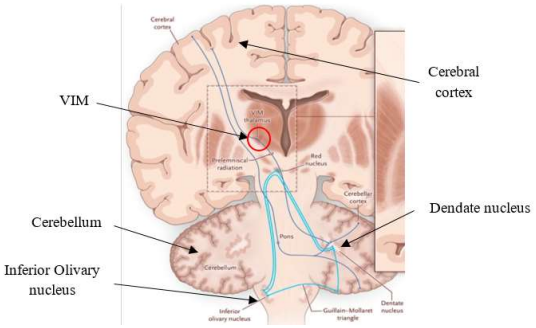

Figure 2.5 - Cortico-olivary-cerebello-thalamic circuit in blue. Highlighted in red is the target for DBS. [21]

Finally, in what refers to the disorder treatment, it can also be through medication or through DBS surgery. Propranolol is a β-adrenoceptor blocker reducing the tremor amplitude in 50% to 60% in 50% of the patients. Other medication also widely used is the primidone which provides a decrease of 50% to 70% of the tremor, despite its mechanism being unknown. DBS is able to reduce tremor by electrically stimulating the ventral intermediate nucleus (VIM) of the thalamus, thus interrupting its current activity. [22]

For this disorder, the evaluation of tremor improvement during therapy is made through a qualitative scale, called The Essential Tremor Assessment Scale (TETRAS). This scale only assesses the tremor severity and its impacts in the daily routine of the patients. [23] Again, this is a subjective scale, bringing the same disadvantages before mentioned.

2.1.3 Physiological kinematics assessment methods

As mentioned before, rigidity, tremor and bradykinesia are very common symptoms in a large number of movement disorders. Furthermore, DBS surgery presents higher improvements on them. For this reason, a brief definition, the clinical assessment operation and some scientific projects related with the assessment of these symptoms are presented in the following topics. The projects referred along this master thesis were mainly found on the b-on and ScienceDirect search engines. In particular, for the projects mentioned in this topic, the research was filtered by introducing the following keywords: "(name of the symptom) evaluation", "quantitative method", "Deep Brain Stimulation".

2.1.3.1 Rigidity

Rigidity can be defined as an increasing resistance, marked by a permanently elevated muscle contraction, in response to passive stretch. In this way, a state of severe rigidity prevents the patients to reach muscle relaxation. Furthermore, their voluntary movements are accompanied by an elevated contraction of antagonist muscles. [24, 25]

In clinical environment, the assessment of rigidity is usually made by inducing a passive movement at the wrist or elbow of the patient. The passive movement is performed by a clinician and it consists, for example, in the flexion and extension of the chosen joint (Figure 2.6). Then, qualitative scales are used to attribute a score based on the perceiving stiffness of the movement. [25]

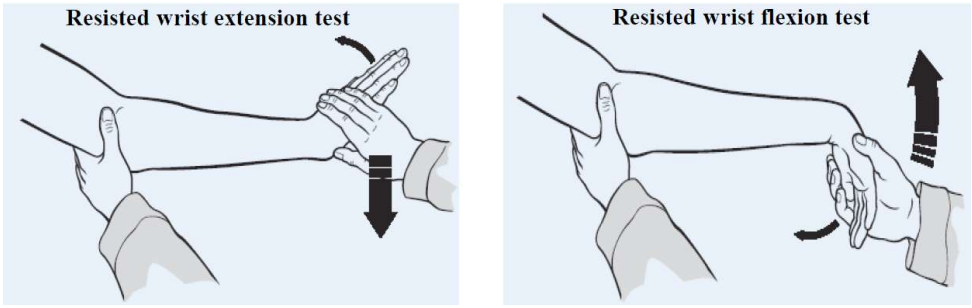

Figure 2.6 - Rigidity assessment in clinical practice. [26]

Research has been done among the scientific community to find performances of quantitative evaluation of rigidity symptom.

From the found quantitative evaluations, only the systems of Dai et al. [27] (Figure 2.7A) and Shapiro et al. [28] (Figure 2.7B) are used during DBS surgery. The other projects, like the ones driven by Park et al. [24] (Figure 2.7C) and Patrick et al. [2] (Figure 2.7D), are performed in regular patient monitoring situations.

Most of the found projects include accelerometers and/or gyroscopes, to determine hand's movement, and force sensors to estimate the force made by the clinician in the patient, during rigidity evaluation [2, 24, 27]. An exception is the system developed in [28]. Here, the movement is induced by a torque motor, being that the rigidity is quantified through the work performed by the torque motor at each cycle of oscillation.

Authors also differ in the joint to evaluate rigidity. While some authors evaluated rigidity based on the elbow movement [2, 28], others induced the movement of the patient's wrist to achieve the rigidity level [24, 27].

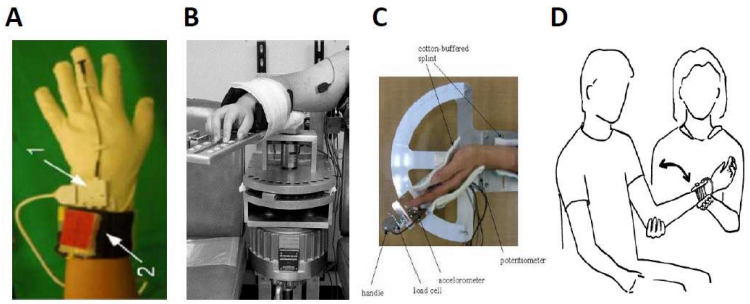

Figure 2.7 - Experimental setups developed in some rigidity quantification research projects. A) Glove monitoring system used to quantify neurological symptoms during DBS surgery [27]. B)Setup to infer about the effects of STN DBS on rigidity in PD. [28]. C) Setup to analyse viscoelastic properties of wrist joint for quantification of Parkinsonian rigidity [24]. D) Sketch of how to use the rigidity quantification device.[2]

2.1.3.2 Tremor

Tremor is a common neurologic symptom expressed by rhythmic and involuntary movements of one or more body parts. [29] Three types of tremor are considered: resting tremor, postural tremor and action tremor. The first type happens when the subject has the muscles relaxed, prominent in PD for example. Postural and action tremor, on the other hand, are most seen in ET, appearing simultaneously to voluntary movements of the muscles.

Similarly to rigidity, the methods of evaluation of tremor are qualitative, being quantified through subjective scores, thus revealing higher insensitivity and inaccuracy. [30] An example is the TETRAS scale mentioned in the ET pathology explanation. Figure 2.8 presents the most common tasks asked to the patients, to infer about their tremor level.

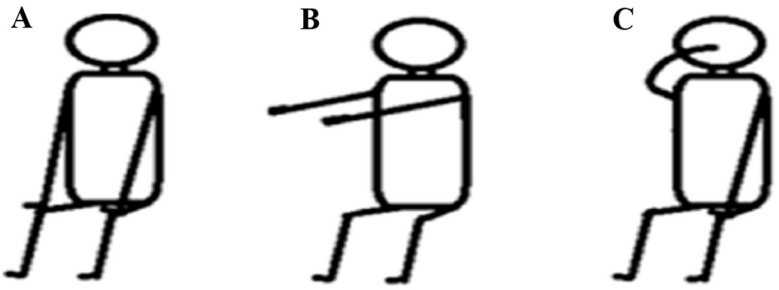

Figure 2.8 - Tasks performed by the patient during the clinical assessment of A) Resting tremor. B) Postural tremor. C) Kinetic tremor. [31]

Developed devices for quantitatively determine tremor scores, use motion data to obtain tremor amplitude and frequency. Therefore, inertial sensors are frequently included in devices for tremor assessment.

Dai et al. [31] (Figure 2.9A) and Giuffrida et al. [32] (Figure 2.9B) have used a similar method for tremor quantification. Both implemented a sensor unit in the patient's middle finger.

The sensor unit included a 3 axes accelerometer and a 3 axes gyroscope. In both projects, the sensor unit was connected to a command module, placed on the wrist, through a thin wire. Also, the tasks asked to the patients for tremor assessment were similar, including the subject remaining still for evaluating resting tremor, subject with arms extended in front of body to quantify postural tremor and subject extend arm and touch nose repeatedly to determine kinetic tremor. The main difference between these two systems setup is that in [31] movement data is transferred for a computer via USB, while in [32] data is wireless transmitted.

Differently, Salarian et al. [33] (Figure 2.9C) used angular velocity data from two gyroscopes included in an Autonomous Sensing Unit Recorder (ASUR). The gyroscopes were disposed in perpendicular directions. A command module wasn´t needed, since the ASUR already included a data-logger, a battery and a flash memory. Furthermore, in this project, the sensor unit is not placed on the fingers but on the patient's forearm. Data was transferred to a computer via cable.

Regarding the features taken from the inertial sensor signals to detect and score tremor, the root mean square of the angular velocities is widely applied to determine tremor amplitude. On the other hand, the construction of a power frequency spectrum is used to infer about tremor frequencies. [32, 33]

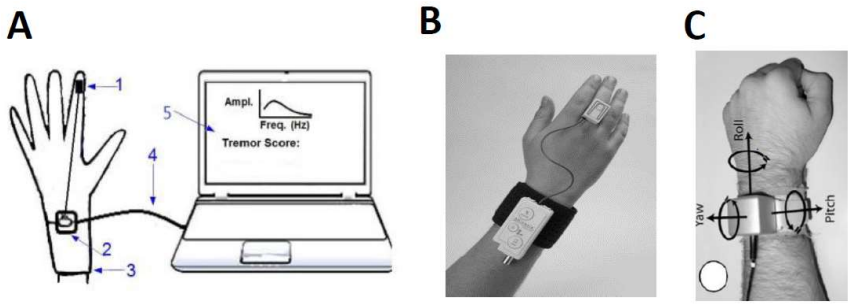

Figure 2.9 - Experimental setups developed in some tremor quantification research projects A) Diagram of the tremor quantification system to assess tremor during DBS surgery. [31]. B) Kinesia System for automated tremor assessment. [32]. C) ASUR system to assess tremor in PD patients [33].

2.1.3.3 Bradykinesia

Bradykinesia consists in the slowness of movement. Furthermore, it is also visible a decreased amplitude of the movement and difficulties in planning, initiating and executing it. To evaluate the level of bradykinesia in clinical environment subjective scales such as UPDRS and Simpson-Angus Scale (SAS) are typically used**.** Common tasks performed by the patients during bradykinesia evaluation are finger tapping, whole hand grasping and hands' supination-pronation (Figure 2.10). [34]

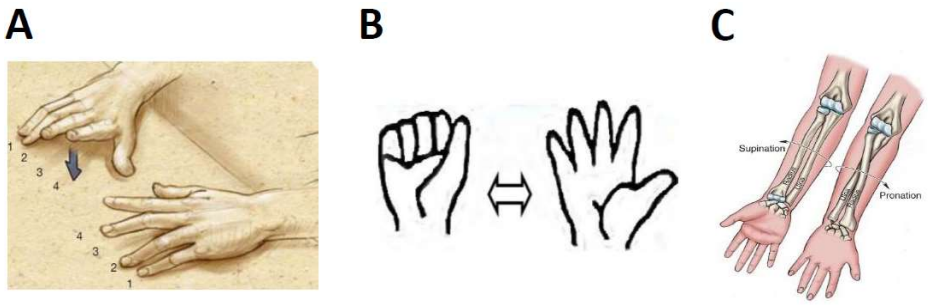

Figure 2.10 - Common tasks in bradykinesia assessment: A) finger tapping [35], B) whole hand grasping [36] and C) supination-pronation of the hand [37].

The existing devices for quantitatively assess bradykinesia often include accelerometers and/or gyroscopes. However, in the majority of the found research, these sensors are not used alone, as in the case of Niazmand et al. [38] (Figure 2.11A) and Printy et al. [39] (Figure 2.11C and D) systems. Indeed, in [38], finger tapping movements between the thumb and middle finger were evaluated through accelerometers and force sensors. Printy et al. [39] have used a gyroscope, an accelerometer, a capacitive touch screen, a microphone and a front-facing camera to measure kinematic data from the hand. This data was then captured by a developed iPhone application and stored for later analysis.

Oppositely to the previous works, Dai et al. [40] (Figure 2.11B) evaluated, whole-hand grasp movements of PD patients using only one 6 DoF IMU (Inertial Measurement Unit) including a 3 axis gyroscope and a 3 axis accelerometer. IMU data allowed to determine amplitudes and frequencies of the task signals.

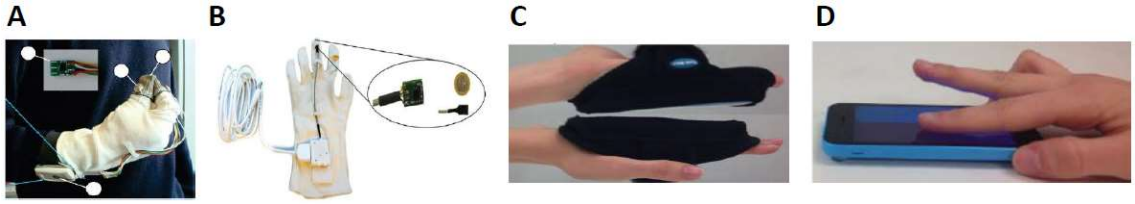

Figure 2.11 - Experimental setups developed in some bradykinesia quantification research projects. A) Smart glove used during bradykinesia assessment. [38]. B) Bradykinesia assessment prototype. [40] C) Diagram of using the application for hand supination/pronation assessment [39]. D) Diagram of using the application for finger tapping assessment [39].

2.1.4 Commercial and research assessment methods and devices

The research of more accurate and comfortable devices for measuring hand kinematics has been growing substantially in the past few years. Furthermore, goals have been the combination of accuracy with lower-cost and smaller components. Being aware of the scope of this thesis, research on hand motion monitoring and force estimative was conducted. Thus, in the following, two topics, Motion tracking and Force tracking, different methods used in the past few years to

track hand motion and force are presented. To reduce and specify the research of the Motion tracking projects, the following expressions with different combinations are examples of the keywords used: “hand kinematics”, “motion tracking devices”, “quantitative methods”, “inertial sensors”, “data gloves”, “wearable devices”. For the Force tracking scientific works, keywords such as “force estimation”, “force sensors”, “hand kinematics”, among others, were used.

2.1.4.1 Motion Tracking

Hand motion tracking has a huge importance in the healthcare domain, as well as in other non-related sectors, like gamming and human-computer interaction. In fact, hand motion tracking is really useful in rehabilitation, not only, to evaluate the upgrading state of neurological patients, who see their mobility affected, but also to give feedback during treatments like DBS surgery. [41]

In the beginning of this topic, no inertial hand function tracking devices developed among the scientific community are explored. The second part of the topic, though, refers only projects using IMUs, since this is the method that the iHandU system uses to track hand kinematics.

No inertial tracking

Different no inertial resources have been used by the scientific community to track hand kinematics. Among them are:

- Electromyography (EMG).
- Goniometers.
- Magnetic sensors.
- Optical sensors.

Through these methods, researchers have been able to infer about hand posture, classify hands’ movements or track only the fingers movement.

Table 2.3 comprises a description of several found scientific projects using the above mentioned methods to track hand kinematics in different ways. In this table, besides being referred the authors and the projects main goals, are also presented the used devices and a small summary of each implemented system.

Table 2.3 - Specifications and summary of the hand's motion tracking projects.

Tracking method	Author(s) – Year (Figure)	Goal	Device(s)	Project’s Summary
EMG Tracking	**Castiblanco et al. – 2016 (Figure 2.12A) [42]**	Identify five movements of the hand.	sEMG electrodes (Myo Armband device)	Placement of the Myo Armband (containing 8 pairs of sEMG electrodes) around the subject’s arm. Through time domain features, was reached the conclusion that SVM was the best classifier for data fitting and a decision tree model would present better results for movements’ classification.

	Karimimehr et al. – 2015 **(Figure 2.12B) [43]**	Estimate fingers and wrist's kinematics.	sEMG electrodes and accelerometers.	Implementation of sEMG electrodes and accelerometers in hand/arm of the subject. After a deep comparison between several linear classifiers and different features, the Output Error and the RMS, were, respectively, the linear model and feature that enable higher recognition accuracy.
	Ricardez et al. – 2018 **(Figure 2.12C) [44]**	Classify grasping movements.	Myo and Leap-Motion devices.	Use of joint angles information obtained through the Myo device and myoelectric potential from the Leap-Motion to extract three features used in a Support Vector Machine classifier.
Tracking based on Goniometers	**Li et al. – 2018** **(Figure 2.12D) [45]**	Fingers' joint motion measurement.	Electrical Semi-conductive Goniometer.	Incorporation of fourteen stretchable bending sensors made of an electrical semi-conducting material (ethylene propylene rubber) as the sensing area in a glove made of silicone materials with different elasticities. An IMU sensor is attached at the back of the hand to monitor the palm movement.
	Yao et al. – 2018 **(Figure 2.12E) [46]**	Track finger kinematic.	Wearable (AgNW) Capacitive Strain sensors.	The high efficiency of the capacitive strain sensors to track finger joints movements was confirmed by calculating the time variation of the joints angles through an optical motion tracking system, and compared to the verified percentage change of strain.
	Carbonaro et al. – 2014 **(Figure 2.12F) [47]**	Obtain fingers' joints angles.	Textile (KPF) Goniometer.	Construction of a lycra sensing glove with 3 KPF sensors made of 75% of electroconductive yarn and 25% lycra for determining 3 specific fingers' joints angles on the index, middle finger and thumb.
	Ciotti et al. – 2016 **(Figure 2.12G) [48]**	Reconstruction of hand posture.	Textile (KPF) Goniometer.	Consideration of joint angles information obtained by five KPF sewn in a sensing glove together with synergy information (multi-finger inter joint covariance patterns) to perform the recognition of eight functional grasps using a K-means algorithm.
Magnetic Tracking	**Fahn et al. – 2006** **(Figure 2.12H) [49]**	Track fingers movements.	Coils used as both sensors and generators of the magnetic field.	Considering the electromotive force produced in the sensor coils, fingertip positions and abduction angles were determined. Taking into account this information and the relation between the adjacent phalanges, the shape of the finger was estimated and the bending angles computed.
	Ma et al. – 2011 **(Figure 2.12I) [50]**	Track finger motion.	Permanent magnets and contactless magnetic sensors.	A combined magnetic field is established by a set of magnets placed in the fingernails. Multiple magnetic sensors are distributed around the wrist measuring the magnetic flux change, according to the fingers motion. A geometric model is applied for reconstruct hand's position and orientation.

Optic Tracking	**Fujiwara et al. – 2013 (Figure 2.12J) [51]**	Measurement of fingers movement.	Optical fibre.	Incorporation of silica fibres in a textile glove through an adhesive gel. Light is measured at the end of the fibre using a Charge Coupled Device (CCD). Light difference data obtained from the sensor is processed and correlated with angular displacements of finger joints.
	Koyama et al. – 2018 (Figure 2.12K) [52]	Hand motion tracking.	Hetero-core optical fibres.	A smart textile made of wool with hetero-core optical fibres woven was placed around the subject forearm. With the forearm movement, occurred the bending of the optical fibre, being translated in correlated optical loss. Therefore, by the variation of the measured light intensity at an implemented photodiode, the performed bending was discriminated.
	Silva et al. – 2011 (Figure 2.12L) [53]	Hand posture monitoring.	Fibre Bragg Sensors.	Fourteen FBG sensors were inserted in the optical fibre. The last, was then integrated in a curvilinear form in a flexible polymeric glove made of polyvinyl chloride (PVC). The system provided angles and hand posture data in real time.

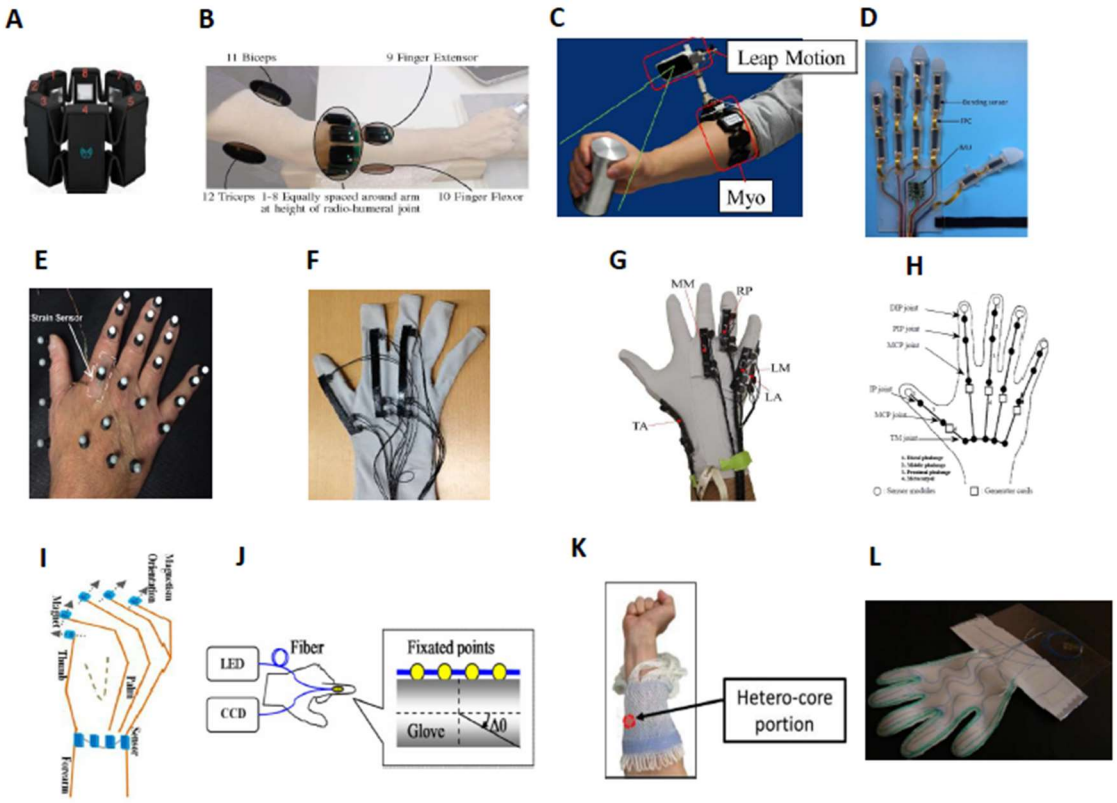

Figure 2.12 - No inertial experimental setups developed in some hand tracking kinematics projects. EMG projects. A) sEMG system (MyoArmband) [42]. B) sEMG electrodes and accelerometers around the subject's arm[43]. C) Visual system (Leap Motion) complementing information of EMG based-sensor (Myo) [44]. Goniometers projects: D) Conductive elastomers goniometers [45]. E) Capacitive strain sensors goniometers [46]. F) KPF goniometers attached to a sensing glove [47]. G) Sensing glove with KPF goniometers [48]. Magnetic projects: H) Structure of the magnetic hand motion tracking system [49]. I) Hand model and magnetic sensors and generators positions. [50]. Optical Fiber projects: J) Diagram to determine angular displacements of the fingers joints[51]. K) Smart textile with optical fiber embedded [52]. L) FBG sensor attached to a sensing glove [53].

Inertial tracking

Commonly, inertial tracking is made with Inertial Motion Units (IMU) which are considered a kind of micro-electromechanical system (MEMS). Indeed, the advances of MEMS allowed the construction of smaller and lower-cost IMU devices, conferring them high attention in the market. IMU sensors are constituted by an accelerometer, a gyroscope and sometimes by a magnetometer. [54, 55]

In accordance with the research done, it can be concluded that one of the major differences among the inertial tracking based systems for hand kinematics assessment is the number and placement of the IMU sensors. For example, Moreira et al. [56], Mohan et al. [57] and O'Flynn et al. [58] aimed to track fingers joints angles to be used in rehabilitation. However, while in [56] ten IMUs were installed in the fingers (a pair for each finger) plus one at the back of the hand, in [57] it is considered that only six IMUs in three fingers and two in the back of the hand are enough

to obtain complete information about the hand kinematics . Moreover, in [58] the same goal was achieved using sixteen IMUs in the fingers' phalanges.

Also, the choice of which sensors from the IMUs to use varies from work to work. While Schaeffer et al. [59] have quantified hand kinematics during DBS surgery, using only gyroscope and acceleration data, the before mentioned authors included the magnetometer to accomplish their objectives.

Differently from the referred projects, Rabelo et al. [60] added EMG sensors, besides the IMU, in the developed setup to track hand motion and muscular activity. Hsiao et al. [61] have also enriched their system adding force sensors to complement pressure measurements to the hand orientation.

Another obvious difference between these projects is the specific IMU used. Therefore, a deeper characterization of the IMU specifications and implemented methodologies as well as a brief summary of seven inertial tracking based projects is shown in Table 2.4.

Table 2.4 - Related publications with IMUs for hand motion tracking.

Author(s) – Year (Figure)	Project's Summary	IMU sensor	Processor	Data Acquisition hardware
Moreira et al. – 2014 (Figure 2.13A) *[56]*	Hand and finger tracking for hand function evaluation in rehabilitation, using eleven sensors placed in the fingers and wrist.	L3GD20: 3-axis gyroscope. LSM303DLHC: 3-axis accelerometer and 3-axis magnetometer.	STM32.	Computer. →Data sent via cable.
Mohan et al. – 2018 (Figure 2.13B) *[57]*	Incorporation of eight IMU sensors in a glove, called i-Glove, in the fingers and wrist zones to track hand motion in rehabilitation.	MPU9250: 3-axis gyroscope, 3-axis accelerometer and 3-axis magnetometer.	Microchip.	Computer. → Data sent via a Bluetooth.
Schaeffer et al. – 2018 (Figure 2.13C) *[59]*	One IMU sensor was sewn in an adjustable strap for the hand's movement quantification during DBS surgery in patients with PD and ET, using only 6 degrees of freedom (DoF).	LSM9DS1: 3-axis gyroscope, 3-axis accelerometer and 3-axis magnetometer.	Arduino.	Alpha Omega Neuro Omega. →Data sent via cable.
Rabelo et al. – 2017 (Figure 2.13D) *[60]*	Electromyography (EMG) electrodes and one IMU sensor was used to assess bradykinesia during the extension of the wrist, differentiating healthy older patients from PD patients.	L3GA4200D: 3-axis gyroscope. LSM303DLM: 3-axis accelerometer and 3-axis magnetometer.	Not specified.	Computer. → Data sent via cable.
O'Flynn et al. 2015 (Figure 2.13E) *[58]*	Creation of a glove with sixteen 9-axis IMUs placed on the fingers phalanges to quantitatively measure the range of the hand joints movements.	MPU9150: 3-axis gyroscope, 3-axis accelerometer and 3-axis magnetometer.	AVR32	Computer. → Data sent via a Wi-Fi.
Hsiao et al. 2015 (Figure 2.13F) *[61]*	A data glove with seventeen 9-axis IMUs positioned on the back of the hand on the phalangeal joints, together with five force sensing resistors, are able to track hand kinematics in real time and determine the pressure made by the subject when grabbing an object.	LSM9DS0: 3-axis gyroscope, 3-axis accelerometer and 3-axis magnetometer.	MSP430	Computer. → Data sent via a Bluetooth.
Kortier et al. 2014 (Figure 2.13G) *[62]*	Determination of the absolute orientation of the hand through eighteen 6-axis IMUs placed in the back of the hand and in each finger segment plus eight 3-axis magnetometers placed on the back of the hand and on each fingertip.	LSM330DLC: 3-axis gyroscope and 3-axis accelerometer.	Atmel XMEGA	Computer. → Data sent via cable.

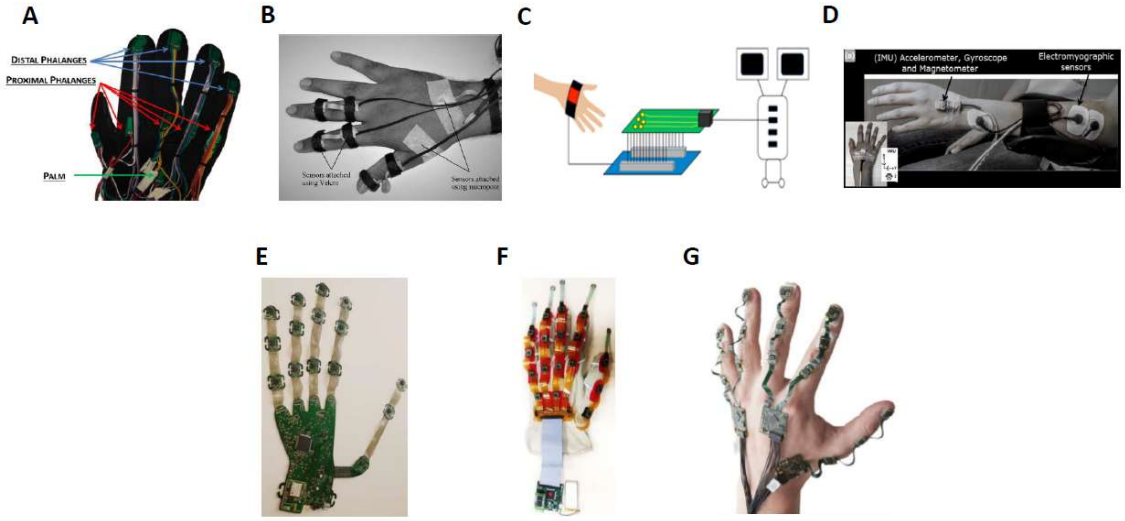

Figure 2.13 - Inertial experimental setups developed in some hand tracking kinematics projects A) Real-time hand motion capture glove. [56]. B) Glove designed for hand kinematics assessment. [57]. C) System of movement quantification during DBS surgery. [59] D) System to assess bradykinesia in PD patients. [60]. E) IMU Smart Glove for hand motion monitoring. [58]. F) Hardware of the system to evaluate hand function. [61]. G) Glove hardware including multiple PCB strings with inertial sensors. [62].

2.1.4.2 Force tracking

There are innumerable types of force sensors with potential to be implemented in wearable systems. However, the main ones applied at the hand level are the piezoresistive (Figure 2.14A), the piezoelectric (Figure 2.14B) and the capacitive ones (Figure 2.14C). While a piezoresistive sensor changes its electrical resistance according to the suffered mechanical deformation, a piezoelectric one is able to perform the conversion of the applied stress into an electrical voltage. In turn, the capacitive force sensors comprise two electrode plates and a capacitance measuring system. So, when the sensor is squeezed, this deformation is measured through the capacitance variation. [63]

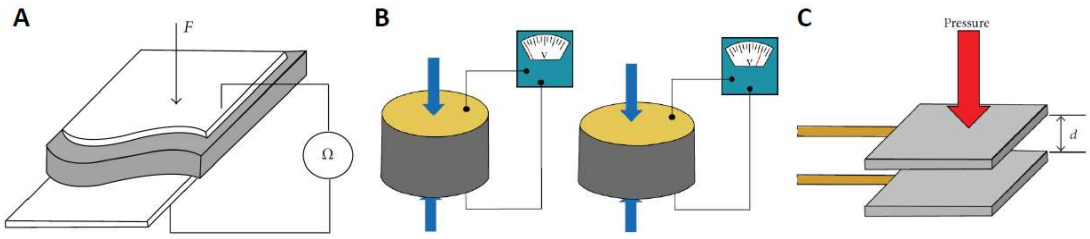

Figure 2.14 - Force Sensors. A) Piezoresistive. B) Piezoelectric. C) Capacitive. [63]

Each one of these types of sensors has its advantages and disadvantages, as presented in Table 2.5.

Table 2.5 - Advantages and disadvantages of piezoresistive, piezoelectric and capacitive force sensors. [63]

Sensor Type	Advantages	Disadvantages
Piezoresistive	→ Low cost. → Good sensitivity. → Low noise. → Simple electronics.	→ Stiff and frail. → Nonlinear response. → Hysteresis. → Temperature sensitive.
Piezoelectric	→ Dynamic response. → High bandwidth.	→ Temperature sensitive. →Not so robust electrical connection.
Capacitive	→ Sensitive. → Low cost. →Availability of commercial A/D chips.	→ Hysteresis. → Complex electronics.

In between the piezoresistive sensors, the Force Sensing Resistors (FSR) are widely used to detect the applied force. When force is applied, the FSR surface deforms, responding with a decrease of its resistance. The change in resistance can then be converted in voltage, thus enabling the prediction of the performed force. [64, 65]

Low thickness, low cost and good shock resistance are the benefits that make them ideal for monitoring force in all type of wearable devices, including those applied to the hand. [64] In fact, scientific projects like the ones performed by Bahadir [65] in, Pasquale et al. [64] also in 2018 and Sakr and et al. [66] in 2017 have used these sensors to accomplish different objectives, detailed in Table 2.6.

Oppositely to piezoresistive sensors, the piezoelectric ones have a good performance in detecting dynamic forces. Therefore, Cotton et al. [67] decided to construct a piezoelectric sensor to detect the slip of an object grabbed by a prosthetic hand. Indeed, these authors state that has been proved that piezoelectric sensors were efficient to detect vibrations due to the slip. Details about this project are in Table 2.6.

On what regards to the capacitive sensors, researchers often create custom capacitors to accomplish their goals. An example is the project driven by Wang et al. [68]. During this research, the authors created a capacitor made of two Polyethylene terephthalate (PET) layers with incorporated copper electrodes and a Polydimethylsiloxane (PDMS) film acting as the insulator layer. The project aim is better understood in Table 2.6.

Table 2.6 - Related publications with Force Sensor for hand motion tracking.

Sensor Type	Author(s) – Year (Figure)	Goal	Force Sensor	Project's Summary
Piezoresistive Sensors	**Bahadir – 2018** **(Figure 2.15A)** **[65]**	Pressure detection.	Interlink Electronics FSR Model 406.	Integration of a FSR in a textile structure by embedding it with conductive yarns.
	Pasquale, Matrototaro, Pia and Burin – 2018 **(Figure 2.15B)** **[64]**	Measure fingertips force.	FlexiForce A301 (FSR). → Small sensing area. → Reduced hysteresis.	Incorporation of four FSRs in a glove's fingertips to evaluate force of the fingertips during neurologic rehabilitation training procedures.
	Sakr and Menon – 2017 **(Figure 2.15C)** **[66]**	Estimate hand force.	Interlink Electronics FSR Model 402.	Measurement of Force Myography signals (detect pressure yielded by the muscles) applying four sensing bands along the subject's arm with 12 to 16 FSRs each.
Piezoelectric Sensors	**Cotton et al. – 2007** **(Figure 2.15D)** **[67]**	Determine slip of objects in a prosthetic hand.	Custom sensor.	Incorporation of a custom piezoelectric sensor on the fingertips of prosthetic hand to avoid objects from slipping.
Capacitive Sensors	**Wang et al. – 2014** **(Figure 2.15E)** **[68]**	Measure gripping force of prosthetic hand.	Custom sensor.	A customized capacitive sensor was implemented on the curved surface of a prosthetic hand thumb to measure its gripping force in different situations.

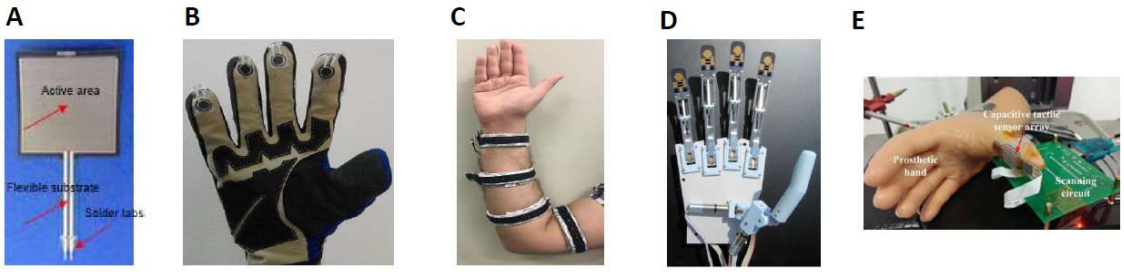

Figure 2.15 - Experimental setups developed in some force tracking projects. FSR projects A) Sensor used to identify sensing capability to of FSR integrated to E-Textile Structure [65]. B) Sensing glove for neurologic rehabilitation trainings. [64]. C) Force Myography bands for hand force estimation. [66]. Piezoelectric projects. D) Integration of a slip sensor in a prosthetic hand. [67]. Capacitive projects. E) Capacitive tactile sensor array integrated into a prosthetic thumb finger. [68].

2.2 Existing iHandU wearable System

Accurate and simple quantitative methods to measure rigidity, tremor and bradykinesia improvements during patients' disorder progression and, in particular, during DBS surgery, aren't known. With this purpose, previous developments performed on the Centre of Biomedical Engineering Research (C-BER) at INESC TEC culminate on the development of a novel and comfortable wireless system to mainly evaluate the improvement of wrist joint rigidity during DBS surgery. This system is called iHandU and began with the efforts of Costa et al. [3], that achieved a patent of the iHandU system. [6] Later the system was improved by Assis et al. [4] and Lopes et al. [5].

2.2.1 System Architecture

The iHandU system consists in a relatively small Motion Mote (MoMo) attached to a textile that surrounds the patient's hand during the DBS surgery and communicate with a smartphone via Bluetooth. Therefore, it includes a Bluetooth module, an IMU, a battery and a Texas Instruments Microcontroller Unit (MCU).

An Android mobile application was developed to enable data visualization and computation of rigidity improvement during the surgery. The overall architecture of the system is represented in Figure 2.16.

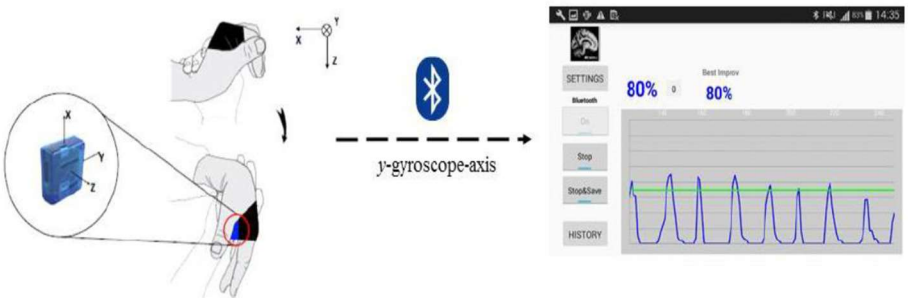

Figure 2.16 - iHandU system architecture. Adapted from [4].

Currently, the iHandU system is being tested at the Functional Surgery and Movement Disorders Unit of Hospital S. João, Porto, Portugal to support the clinical assessment of rigidity symptoms. The system provides a helpful computerized evaluation of the rigidity improvements.

2.2.2 System Acquisition method and data processing

On what concerns to the signal acquisition, only wrist flexion movements were evaluated. Furthermore, only the y-axis values from the gyroscope were considered once it reveals higher accuracy in faster movements and it ensures data invariance in relation to hand rotation and position.

Focusing on data processing, positive arcades of the signal, corresponding to wrist extension, were discarded and the absolute value of the negative arcades were taken from the signal. A baseline signal, i.e., wrist flexion signal before stimulation, was measured to serve as control for the signals acquired during stimulation.

As aforementioned, rigidity can be defined as an increasing resistance to the movement, thus limiting the speed, the range and the smoothness of the imposed wrist flexion. Indeed lack of smoothness is visible in the baseline signal (Figure 2.17A first trace) due to the influence of the cogwheel effect in the wrist movement. This effect is highly associated with joint's rigidity.

In Figure 2.17A are also represented the 50% (second trace) and 80% (third trace) rigidity improvement signals (signals acquired during electric stimulation). From the signals is possible to conclude that a less rigid movement revealed higher velocities and amplitude values and a smoother signal, annulling the cogwheel effect.

Taking this into account, the average angular speed (μ_ω) and the average peak value (μ_P) are extracted from the signals to compute a signal descriptor $\emptyset$, defined in 2.1.

$$\emptyset = \sqrt{\boldsymbol{\mu_\omega \cdot \mu_P}} \qquad \textbf{2.1}$$

A schematic representation of these values is made in a rigid signal of Figure 2.17B.

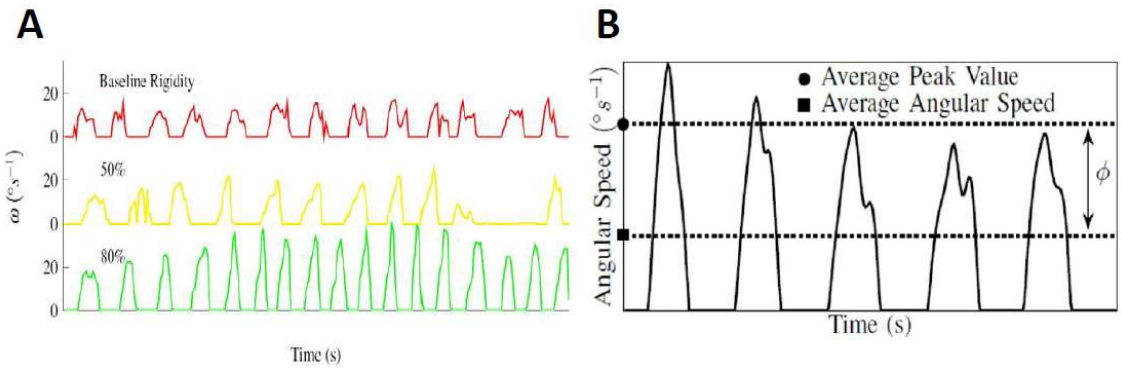

Figure 2.17 - iHandU method to quantify rigidity improvement. A) Angular velocity signals. Adapted from [4]. B) Average angular speed (square symbol) and the average peak value (circle symbol) [3].

To quantify the achieved improvement of the movement, two label scores were applied: the medical label score and the iHandU label score. The first mentioned, comprehend a range of possible improvement values from 40% to 80%, with steps of 10. The iHandU score can attribute scores from 0% to 80%. Lower values for medical label score were not considered due to the difficulty in detect slight improvements. The inclusion of the medical opinion on the algorithm was made to add accuracy to the system assessment. This was achieved by discarding the system values with a difference higher than $\pm 5\%$ from medical score. In addition, due to restrictions in medical scores, also the values lower than 40% in the iHandU score were discarded, and the remaining were round to the closes ten.

2.2.3 System results and scientific publications

The most recent work, developed by Sofia Assis, counted with 10 participants from which 237 evaluations were used to train the model and 38 to validate it. The designed model reached a classification accuracy of 82% with a mean error of 3.4%. [4]

In 2015, the iHandU system started being developed by Pedro Costa, who with the contribution of Maria José Rosas, Rui Vaz and João Paulo Silva Cunha, patented their developed method to determine the improvement of rigidity performed by the patient. [6] Furthermore, they achieved a publication in Proceedings of the IEEE International Conference of the Engineering in Medicine and Biology Society (EMBS). [3]

Later in 2016, Sofia Assis added several improvements to the system during the execution of her thesis. In particular, she focused on enhancing the rigidity model, adding the evaluation of the tremor symptom and improving the Android mobile application. Sofia Assis got two publications. One of them had the contribution of Pedro Costa, Maria José Rosas, Rui Vaz and João Paulo Silva Cunha in Proceedings of the IEEE International Conference of the EMBS [4] and the other in Neuroiberia in which the authors mentioned have also collaborated. [69]

Moreover, also Elodie Lopes has invested in this project by organizing data and improving the rigidity model [5].

3

3 Theoretical Fundamentals

In this chapter, the concepts related with the implementation of a Wearable Health Device (WHD) are discussed. To start, in 3.1, an overview of a Wearable Health System (WHS), in which the WHDs are important components, is made. The subsequent topics are focused in hardware concepts that must be known when constructing a WD. Therefore, since it is aimed to include a micro Inertial Measurement Unit (IMU) in the device to track hand kinematics, in 3.2 Microelectromechanical Systems (MEMS) IMUs are explored. Following this reasoning, topic 3.3 consists in an analysis of the possible Digital Communication Protocols to establish between the employed sensors and the MCU that manipulates their data. Lastly, in topic 3.4 is referred possible Computer-Aided Design software to design the Printed Circuit Board (PCB) where the electronic components are assembled.

3.1 Overview of a Wearable Health System

Making part of any Wearable System (WS), the existence of wearable devices (WDs) provide a new form of human-computer interaction, with an endless list of applications and advantages. The WDs have emerged in the military field but rapidly extended to other areas. Nowadays, besides the military field, WDs are implemented in industry, fitness (smart fit bands), entertainment (virtual reality), healthcare and many others. [70] In particular, WDs had an enormous impact in the healthcare environment, originating Wearable Health Devices (WHDs). WHDs have been enhancing the healthcare system, being used in home monitoring for chronic and elderly patients, real-time continuous patient monitoring in hospitals, monitoring of physiological parameters, rehabilitation progress and emergency situations. [71]

In this master thesis, the construction of a WHD to monitor wrist rigidity improvement of motor disable patients was intended. Therefore, due to the need of understanding well the generic architecture of a WHS, where a WHD is included, the first topic of this chapter focus on concepts of this theme. Moreover, it was also aimed to incorporate the referred WHD in a textile band that wraps the patient's hand. Thus, the second topic here presented refers some techniques to construct hand kinematic devices based on fabrics and some related scientific projects.

3.1.1 Generic architecture of a Wearable Health System

The architecture of a Wearable System varies with the requirements needed to fulfil their respective objectives. Even among WHS, different architectures approaches can be designed. However, reliability in the transmitted data, energy efficiency and user's friendly are mandatory requirements. [71]

In the context of this project, the architecture of a WHS can be fragmented into four parts (Figure 3.1): the Body Area Network (BAN), a Portable Unit (PU), the wireless/radiofrequency protocols and the Portable Device (PD). [72]

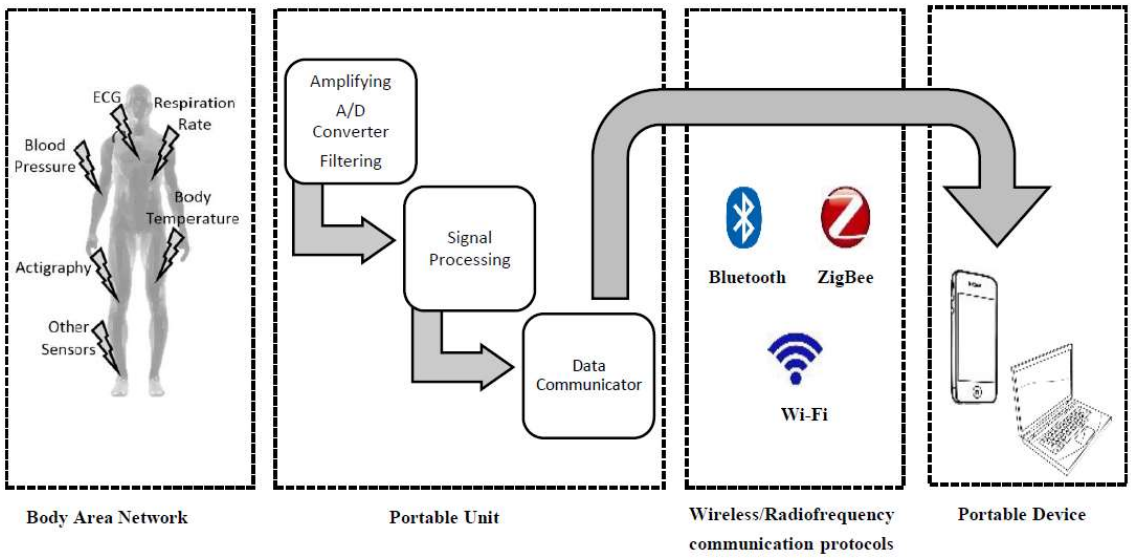

Figure 3.1 - Architecture of a Wearable Health System. Adapted from [72]

In the healthcare environment, information from multiple sensors is often needed. Therefore, BAN corresponds to the group of sensors deployed in the user's body. [73] Researchers' effort has not only been in the construction of smaller, low-cost and low-power sensors as well as their incorporation on the user. [72] The objective is to guarantee the maximum comfort, minimum impact on users' daily routine and, at the same time, reliability in the gathered data. [74]

The second part of the presented WHS is the PU, which corresponds to data processing. Until now, the connection between the sensors and the PU were mainly wired, since it consists in cheaper and easier implementation solutions. [72] However, recent works are focused on creating wireless solutions in order to satisfy requirements like wearability, non-invasiveness and comfort. [75] In addition, these requirements are frequently achieved by incorporating the wearables in textiles, which is one of the most used materials by humankind. [76] For this reason, the next topic will focus on the integration of electronic components in textile materials.

The processed raw data is transmitted to a portable device via a wireless protocol. The three most used protocols are Bluetooth, Wi-Fi and ZigBee. [72] Bluetooth is a very common wireless

standard used in device-device communication. One of its advantages is to provide the interaction between devices without needing a line-of-sight positioning. Additionally, it guarantees a high level of security, which is an important assurance when dealing with personal healthcare data. Wi-Fi provides faster wireless connectivity being ideal to large data transmission. [77] Furthermore, is also best suited in longer distances communication due its capability of covering a maximum range of 200 meters free from obstacles. [72] ZigBee is ideal for applications that need long battery life, since it requires lower power consumption. However its slower data transfer rate is a known disadvantage that constrains its application. The low power consumption associated to ZigBee and Bluetooth, make them the most widely used protocols in the healthcare domain. [77]

3.1.2 Textile based devices for hand kinematics analysis

It is foreseen that electronic components will be embedded in our daily outfits, once they are able to recognize the activity of their own user contextualized with the surrounding information. [78]

With the incorporation of electronic components, textiles raise to smart textiles by gaining properties that are usually performed by electronic systems, such as conductivity. To accomplish the referred incorporation, different techniques exist: [72]

- Metal yarns incorporating conductive fabrics, i.e. the metal yarns are wrapped with the textile yarns or are made channels for their integration.
- Gluing a conductive fabric in other fabric.
- Incorporation of electro-conductive yarns containing polymeric or carbon-coated threads.

To better understand this area, scientific research was made to find how the scientific community has been incorporating the electronic components in textiles. So, in the following paragraphs, different projects that successfully accomplished this objective are presented.

In medical environment there is a large research around smart fabrics mainly to measure physiological signals. Zysset et al. [79], in Switzerland, created a sensor textile based on the Near-Infrared Spectroscopy (NIRS) principle. Their goal was to measure both pulse waves at the fingertips and changes in oxygenated and deoxygenated haemoglobin (O_2Hb and HHb, respectively), during a venous occlusion at the calf. With this intention, they used micro-fabrication techniques, like soldering, gluing and wire bonding to mount the necessary components in three different kinds of double-layer flexible plastic strips. The strips were manually inserted into the textile in the weft (longitudinal) direction. The insulated copper wires were then soldered in the wrap (lateral) direction (Figure 3.2).

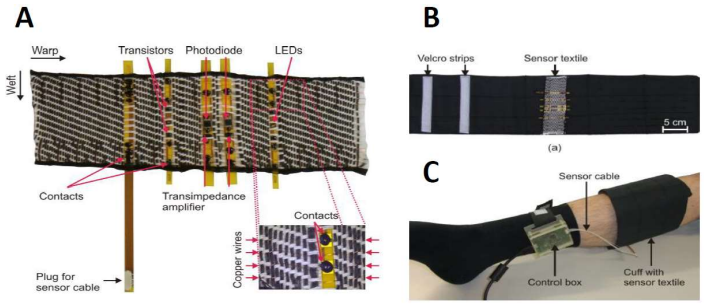

Figure 3.2 - Smart textile developed in [79]. A) Woven sensor textile with flexible plastic strips in weft direction carrying LEDs, transistors, photodiodes and transimpedance amplifiers. B) Sensor textile sewn into a textile with Velcro strips for attaching to the human body. C) The textile is strapped to the calf together with the control box.

Oppositely, Bahadir [65] incorporated a Force Sensing Resistor (FSR) in a textile, by introducing six conductive yarns with different linear resistances in a polyester base structure. The connection of the sensor with the yarns was established in one of the yarns extremity using snap fasteners (Figure 3.3).

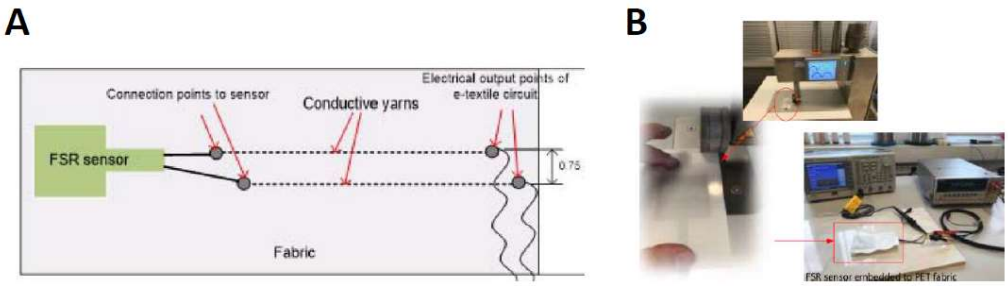

Figure 3.3 - Smart textile developed in [65]. A) Schematic diagram for FSR integrated to e-textile circuit. B) FSR sensor embedded to Polyethylene Terephthalate (PET) fabric via ultrasonic welding machine for pressure detection.

Although the authors have made a complete integration of the sensor components in the textile, not all the electronic were embedded. In both Figure 3.2 and Figure 3.3 the acquisition hardware outside the textile is visible.

Recently, some smart garments, in the healthcare domain, to track motion have also been developed. However, their main focus is not the hand kinematics, but the postural monitoring. With this purpose, Kang et al. [80] incorporated four IMU sensors in a highly stretchable knit t-shirt, by embroidering a polyurethane-coated copper filament (PU-Cu) and polyester (Figure 3.4). These filaments enable the connections between the sensors and the processor.

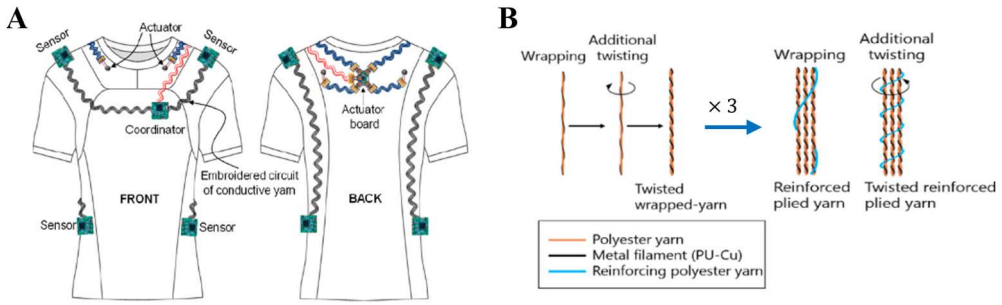

Figure 3.4 - Kang et al. project. A) Smart t-shirt prototype. B) Development of the conductive yarn. [80]

On the other hand, An et al. [81] assured the electronic textile biocompatibility, in their motion tracker chest band, using a knitted conductive fabric made of silver plated nylon 66 and elastomer. A 9-axis MPU-9250 sensor was embedded in the textile electrode through a specially designed Flexible Printed Circuit Board (FPCB). Through this board was assured the power supplies and the transmission of data from the sensor to the microcontroller (Figure 3.5).

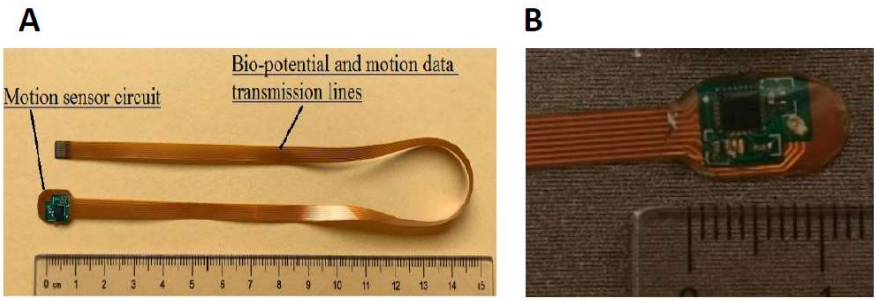

Figure 3.5 - An et al. project. A) Flexible printed circuit. B) Photo of integration of the circuit board in the textile. [81]

Focusing on the hand, there are several data gloves incorporating IMU sensors. Elastic and stretchable properties of the glove material is common in most of the studied projects. [82, 83] This because a stretchable fabric doesn't interfere with the mobility and comfort of the user. However, instead being embedded, sensors are often attached to the textile gloves. Mummadi et al. [82] (Figure 3.6A) and Connolly et al. [83] (Figure 3.6B), created an IMU-based glove for hand monitoring, by interconnecting the IMUs between each other and with the processor unit through stretchable cables, that are then attached to an elastic textile glove.

Figure 3.6 - Sensing glove based on IMU sensors developed in [82].

In form of conclusion, embedding of electronics in textiles is a growing field. However, based on the made research, projects where all the electronics (sensors and acquisition hardware) are completely embedded into textiles were not found.

3.2 Microelectromechanical Systems: Inertial Measurement Units

Microelectromechanical Systems (MEMS) consist in a technology where mechanical elements fabricated in micro scale, such as cantilevers and membranes, are added to microelectronic circuits. [84] These devices are known not only for their small size but also light weight, low power consumption, low cost, high sensitivity and high resolution. All these characteristics explain the reason of such interest for this concept. [85]

Inertial Measurement Units (IMUs) include, at least, a gyroscope and an accelerometer meant to provide information about the orientation and position of any object they are on. Particularly, the gyroscope measures the angular velocity of the sensor to estimate its orientation and the accelerometer measures the resultant acceleration force applied on the system to determine its position. Both sensors are able to track motion of a system individually, but their separated results don't contain the desirable accuracy. For this reason, not only their data is combined, as also the presence of additional sensors to reach a high level of quality in the measurements is usually required. Commonly, magnetometers, which provide the direction of the magnetic field, are joined in the IMUs. [86]

Due to their capability of accurately providing orientation information, inertial sensors have innumerable applications. For this reason and taking into account the referred characteristics of the MEMS technology, researchers together with the industry started to work on the miniaturization of gyroscopes, accelerometers and magnetometers, to construct the microelectromechanical inertial sensors – MEMS IMUs. [86] A MEMS IMU is a miniaturized motion tracker employed in areas from human motion tracking until pose estimation of cars, boats, trains. It also covers other areas such as of robotics, navigation, biomechanical analysis and gaming industries.

To better understand the operation of a MEMS IMU, a description of the work principles of microscale gyroscopes, accelerometers and magnetometers are conducted in the following topics. In addition, the final topic rapidly summarize the concepts of sensors data combination.

3.2.1 Gyroscope

The main purpose of a gyroscope is to provide the angular rate of a rotating system. Coriolis Vibrating Gyroscopes (CVG) correspond to the biggest percentage of the MEMS gyroscopes. As

can be inferred by the name, their principle of operation is based on the Coriolis Effect, which consists in an apparent force that emerges on a rotating frame giving the illusion that an object is deviating from its path. [87] Despite the different possible designs of these CVG, all of them must consider two modes of vibration: the drive mode and the sense mode. Here is mentioned the most popular CVG, the Tuning Fork Gyroscope (TFG). [88]

The TFG consist in two anchored beams and two proof masses (Figure 3.7A). Opposite oscillations in the horizontal plane are induced in the proof masses. These oscillations result in their vibration at one of their natural frequencies, also called as drive mode of vibration (Figure 3.7B). When the gyroscope sense angular rotation, the proof masses start to vibrate in opposite vertical directions: sense mode of vibration (Figure 3.7C). These vertical oscillations result from the Coriolis effect. Metal plates are positioned above the proof masses to form a capacitor. The distance between the metal plates and the proof masses only change when the system is in the sense mode, i.e., when an angular rotation is applied. Through electrical equipment, the change in capacitance can be discovered and a signal proportional to the angular rate is produced. [89]

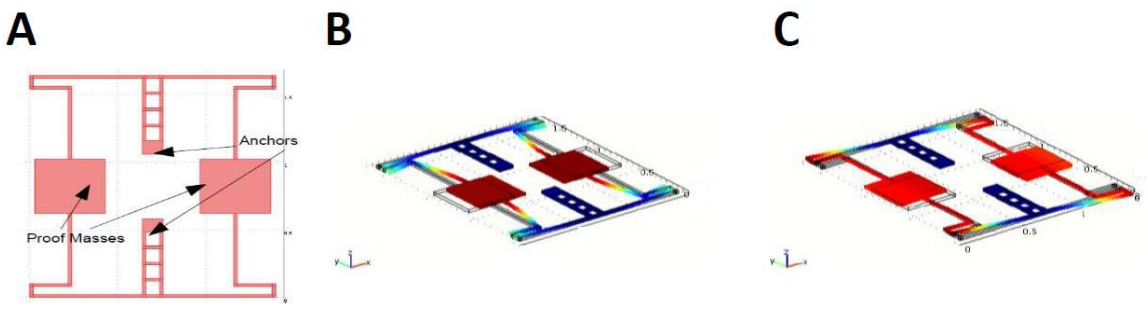

Figure 3.7 - TFG. A) Mechanical Structure. B) Drive mode of vibration. C) Sense mode of vibration. [89]

3.2.2 Accelerometer

The accelerometer provides linear acceleration of the system, in one or more axes, by measuring static (e.g. gravity) or dynamic acceleration forces, which appear due to the motion of the device. Accelerometers are one of the MEMS technologies with a widest range of application, being indispensable in the automobile industry, computer and audio-video technologies. [84]

Their operation is based on the second Newton's Law. Therefore, it is the force resulting from the acceleration of the system that is measured by the different sensing mechanisms of the accelerometer. These mechanisms can be either capacitive, piezoresistive or piezoelectric. [90]

A capacitive accelerometer includes a movable mass attached to a mechanical spring on silicon substrates. Furthermore, there are movable electrodes, associated with the movable mass, and fixed electrodes (Figure 3.8). When the system is under acceleration, a resultant force induces the displacement of the mass. As result, the distance between the movable and the fixed electrodes causes changes in capacitance. An electrical circuit is included in the accelerometer structure to transform the capacitance variation in an analog voltage signal, proportional to the induced force.

This is the example of a one axes accelerometer. However, by placing several similar of these structures displaced by 90º or by arranging the capacitive sensors properly, multiple axes accelerometers may be created. [90]

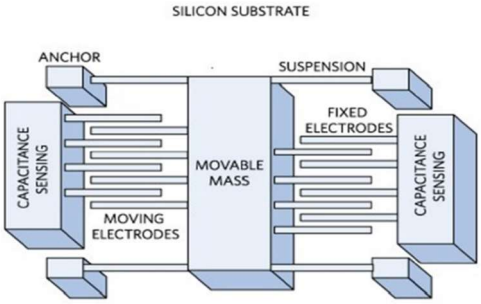

Figure 3.8 - Capacitive accelerometer model. [90]

Despite several possible configurations of piezoresistive accelerometers, they all include a movable mass attached to a rigid frame through flexure beam(s). These beams have piezoresistor elements, which are sensitive to stress induced by acceleration.

According to the configuration of the piezoresistive accelerometer, in Figure 3.9A, a movable mass is connected to a rigid frame through four flexure beams. In the maximum stress points of these beams are eight piezoresistor elements, forming a Wheatstone bridge (Figure 3.9B and Figure 3.9C). [91] The vibration of the mass due to the acceleration, causes stress in the beams, changing the resistance of the piezoresistor elements. Using Wheatstone circuits, the resistance difference is converted into an electrical signal, which is proportional to the acceleration of the vibrating mass. [92-94]

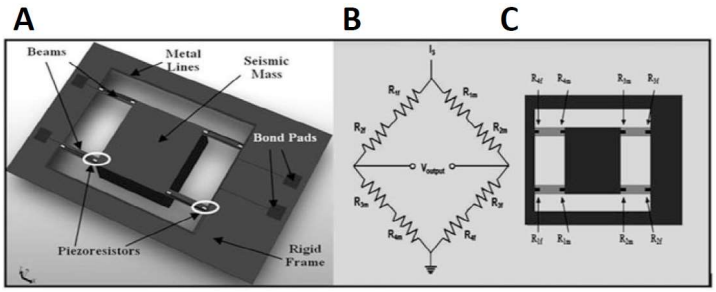

Figure 3.9 - Piezoresistive accelerometer. A) Structure. B) Wheatstone bridge arrangement. C) Mapping of the piezoresistor elements on the MEMS accelerometer. [91]

Also the piezoelectric accelerometers have different designs. Among them the annular diaphragm (Figure 3.10A) and the trampoline model (Figure 3.10B) are possible options. The most common piezoelectric material used in the accelerometers is the lead zirconate titanate. When force resulting from acceleration is applied in these kind of materials, the piezoelectric material produce an electrical voltage, proportional to the acceleration sensed by the device. [95, 96]

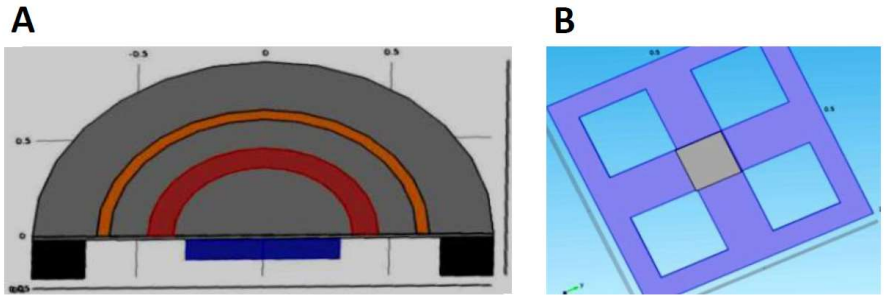

Figure 3.10 - Piezoelectric accelerometers. A) Annular diaphragm model. B) Trampoline model. [95]

3.2.3 Magnetometer

Magnetometers are sensitive to the surrounding magnetic field. Their application has been growing in the last years, having an important impact in science, engineering and industry fields. In fact, at the moment, they are used for vehicle detection, control mineral prospection, medical diagnose and for several other purposes. [85] In MEMS technology, magnetometers can be divided in two main groups: the ones based on the Lorentz force and the magnetoresistance magnetometers.[97]

The Lorentz force consists in a force applied on a charged particle through an electric and a magnetic field. [98] The magnetometers based on this force can be, in turn, divided in the Hall effect magnetometers and the resonant magnetometers.

Both, these two types of magnetometers, consist in the application of a magnetic field perpendicular to a plate where current is flowing, thus resulting in the appearance of the Lorentz force. In the Hall Effect magnetometers (Figure 3.11A), this force cause a drift in the electrons path, leading to the concentration of electrodes in one side of the plate and a consequent voltage difference. [85, 99] In the resonant magnetometers, the Lorentz force effect can be detected either through capacitive (Figure 3.11B), optical or piezoresistive techniques.

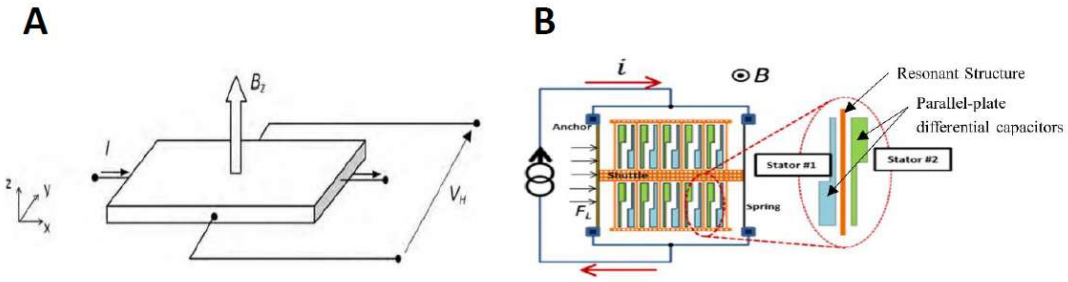

Figure 3.11 - A) Hall effect principle. [85] B) – Capacitive resonant magnetometer, where the displacement of the plate is measured by the group of parallel-plate differential capacitors. Adapted from [100].

The magnetoresistance magnetometers are based on resistance differences caused by the presence of an external magnetic field and they can be giant magnetoresistance magnetometers or a anisotropic magnetoresistance magnetometers.[101]

The giant magnetoresistance magnetometers (Figure 3.12A) are constituted by three main layers: a layer where the magnetization is fixed, a layer where the magnetization varies according to the applied magnetic field and an intermediate thin conductive layer. Therefore, when the magnetizations of the two first mentioned layers are parallel to each other, the current of electrons between the layers is maximum and, when the same magnetizations are normal to each other, the current of electrons is minimum, resulting in changes of resistance values. [97, 101]

The anisotropic magnetoresistance principle (Figure 3.12B) involves the application of permalloy to act as a magnetometer. An external magnetic field is applied to the system, influencing the rotation of the magnetization. Indeed, the angle of magnetization rotation depends on the magnitude of the applied external magnetic field. A current will be flowing in the magnetic material and the resistance of the current will decrease as the direction of the magnetization is moving away from the current's direction. [97]

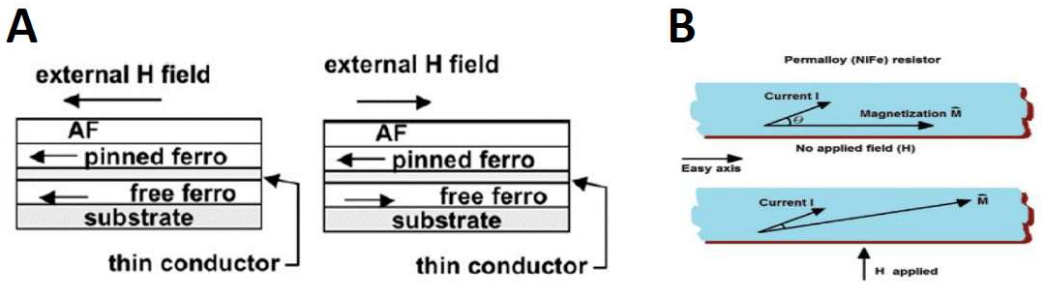

Figure 3.12 - Giant magnetoresistance principle. A) Parallel magnetizations → low resistance state; Opposite magnetizations → high resistant state. [101] B) Anisotropic magnetoresistance principle. [97]

3.2.4 Data fusion Processing methods

As mentioned before, inertial sensors include at least two, but often three, sensors. The limitations of each sensor make it necessary the convergence of the IMUs provided data in order to obtain reliable orientation information. Additionally, before performing the data combination, it is important to understand how orientation can be represented with the gyroscope, the accelerometer and the magnetometer data.

Therefore, the following points, Orientation representation and Sensors data fusion, will make a brief resume on how orientation is commonly represented and how the IMU data combination is performed.

Orientation representation

To determine the orientation of a body, two coordinate systems must be considered: an earth-fixed coordinate system (EFCS) and a body-fixed coordinate system (BFCS). [102] In this way, the position and orientation of the BFCS is measured with reference to the EFCS. [86] The most common EFCS used is the Local North-East-Down (NED) CS. The origin of this frame can be at any point of the surface of the earth. Its x and y axes point to the north and east, respectively and its z axis is defined through the right hand rule (Figure 3.13A). The BFCS has its origin at the centre of mass of the body in study. Its x and z axis point forward and bottom, respectively, and its y-axis is also determined using right hand rule (Figure 3.13B). [103, 104]

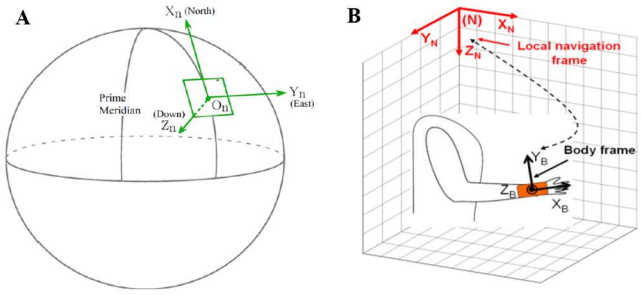

Figure 3.13 - Sensor's data fusion. A) Earth-fixed CS (NED). Adapted from [105]. B) Body-fixed CS [106].

There are several ways to represent the relation between these two CS. Among them, Euler Angles and quaternions are the most implemented ones.

In 1776, Leonhard Euler described the orientation of a rigid body, by using three rotation angles, performed by the rigid body with respect to a fixed CS, in a specific sequence. [102, 103] The standard sequence consists in a rotation first about the Z_B axis, to obtain the yaw (or heading) angle (ψ), followed by a rotation about the Y_B, finding the pitch angle (θ) and lastly a rotation about the X_B axis that results in the roll angle (ϕ) (Figure 3.14). [105]

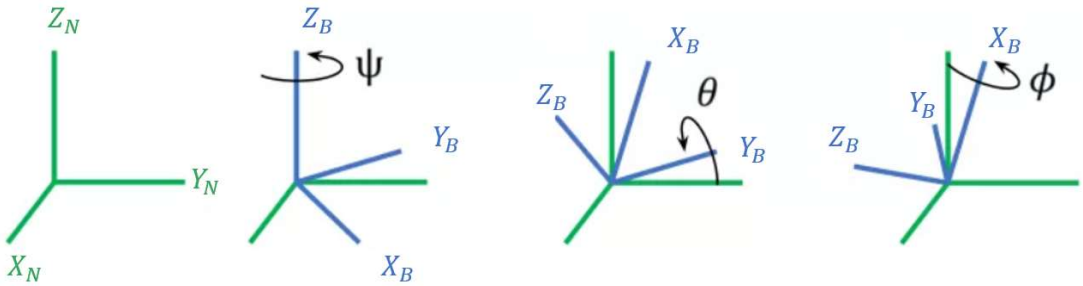

Figure 3.14 - Representation of the Euler Angles. In green the navigation CS. In blue the body CS. Adapted from [4].

Quaternions are a four-dimensional extension of complex numbers. As mentioned above, quaternions are also able to represent the rotation of the body CS relative to the navigation CS. [107] A quaternion can be represented as in 3.1.

$$\boldsymbol{q = q_0 + (q_1 i + q_2 j + q_3 k)} \quad \textbf{3.1}$$

where q_0, q_1, q_2 and q_3 are real numbers and i, j and k are unit vectors directed along x, y and z axis, respectively. [108]

Sensors data fusion

As already mentioned, gyroscope and accelerometer have some limitations in estimating orientation alone.

Gyroscope is able to yield the three pitch (θ_g), roll (ϕ_g) and yaw (φ_g) angles through its measurements of angular velocities in x, y and z directions. [4] However gyroscope operation is only effective at fast rotations. In slow or still situations the drifts will be integrated over time, leading to bigger errors, thus resulting in a non-reliable orientation estimation. [86, 102] Therefore, a high pass filter must be applied to the data, thus minimizing the influence of noise derived from slow situations. [109]

The accelerometer is able to obtain the pitch (θ_a) and the roll (ϕ_a) angles through its measurements of linear acceleration on x, y and z axes. [109] On what regards to the yaw angle, the influence of gravity force in the system makes the accelerometer unable to calculate it. The gyroscope data is needed to remove the influence of the gravity force. [86] Though, the accelerometer measurements are only reliable in still or slow motion conditions. When the system acquires high speed, data is affected by noise. Similarly from what happens to the gyroscope, the double integration required for obtain position data means that drifts are also integrated, leading to inaccurate results. [102]

To solve the uncertainties resulting from the integration steps of the gyroscope and accelerometer, other sensors are integrated in the IMU. Magnetometer incorporation is the most frequent solution, since this sensor complements orientation information based on the direction of the magnetic field. [86] In this way, the magnetometer is used to provide the yaw (ψ_m) angle, missed in the accelerometer measurements.

At this point, data from the accelerometer and the magnetometer is merged to obtain the three pitch (θ_a), roll (ϕ_a) and yaw (ψ_m) angles. Then, these angles are integrated with the ones obtained from the gyroscope. A filter for data fusion is used to compensate the generated errors. [109]

3.3 Digital Communication Protocols

Digital communication protocols are used to exchange data between two computing systems. In this project, data must be exchanged either from the sensor to the microcontroller as

from the last to an external device. Therefore, digital communication protocols are a reasonable topic to be explored.

In the following topics, the most commonly implemented digital communication protocols between sensors and a processor are analysed. This analysis is of utmost importance for the choice of the sensors to implement in the system. Additionally, in the end, the protocol of Bluetooth Low Energy technology, which is here discussed due to the intention of including it in the system to be developed to transmit data from the processor to a smartphone, is referred.

3.3.1 Inter-Integrated Circuit

The Inter-Integrated Circuit (I^2C) is a multi-master protocol which enables the connection between any number of slaves and any number of masters. The master is the device initiating the data transmission, while the slaves are the connected devices. [110]

At the physical level (Figure 3.15A), the I^2C protocol consists in two active wires, which are the serial data (SDA) line and the serial clock (SCL) line. The SDA, as the name suggests, is the line in which data is exchanged, while the SCL line defines the timer at which data is being exchanged in the SDA line. Pull-up resistors are connected to these lines in order to pull them to VCC, thus decoding a logical one. According to the I^2C specification, the data presented on the SDA line can only change if the SCL signal is at the logic zero state. [110]

Regarding data transference (Table 3.1), the first step is the emission of START condition by the master. Then, the master sends a 7 bits address, which specifies the device it wants to communicate with. To note that each device in the I^2C protocol has a unique address.

An indication about the pretended operation to be performed by the master, read (one) or write (zero), is sent with the address information, as the last bit. All the slaves receive the address sent by the master and compare it with their own. In a no matching situation, the slaves wait until a STOP condition, which will end the communication. In a matching situation, an acknowledgment signal will be sent by the matched slave to the master, enabling the beginning of the data transmission. [110]

Table 3.1 - Transference of 2 bytes data with I^2C protocol. Adapted from [110].

Start	Slave address	R / W	ACK	Data	ACK	Data	ACK	Stop
1 bit	7 bits	1 bit	1 bit	8 bits	1 bit	8 bits	1 bit	1 bit

Data is divided in bytes. In the case of master receiving data, it is the master that must send an acknowledgment signal at each read byte. In the opposite operation, it is the slave that sends the acknowledgement signal at each received byte. After data be correctly transferred, a STOP condition is emitted by the master and the connected devices wait for the next transmission. [110]

The I^2C digital protocol enables a flawless communication between multiple devices using just two physical wires, which means a more simple hardware implementation. One of I^2C drawbacks are the constraints of the data rate values, being more used for slower data transference. The limit of the devices addresses to 7 bits can also be a disadvantage for the I^2C communication protocol. However, this issue is overcome by a 10 bit extension, where two words are used to address the device: the first comprises the most significant bits and the second includes the least significant bits. Another disadvantage of the I^2C communication is the inability to communicate with two sensors with the same address. Actually, establishing an I^2C communication with two similar sensors with the same address would lead to errors in the communication. To solve this problem, sensors units usually have two addresses, being possible using both. Generally, among similar sensors only changes the 7^{th} bit of the address. [110]

3.3.2 Serial Peripheral Interface

SPI stands for Serial Peripheral Interface. Compared to the I^2C, the SPI communication protocol consists in a very different form of establishing communication (Figure 3.15B). First, only one device can act as the master to start the communication with the several possible slaves. In addition, the SPI uses four, and not only two, connection wires for each master-slave interaction. One of these wires is the clock signal (SCLK). The clock signal is sent by the master to all the slaves. Other of the wires is the slave select signal (SSn), which allows the master to select the slave to establish communication with. Thus, the number of these selection lines is equal to the number of slaves in the communication system. Finally, there are two wires, instead of one as in the case of the I^2C protocol, to exchange data. One of them, is named Master Out-Slave In (MOSI), where the data flows from the master to the slaves, and the other is the Master In-Slave Out (MISO) data line, for transference of data from the slaves to the master. It must be reinforced that each SPI signal must be synchronous with the SCLK. [110]

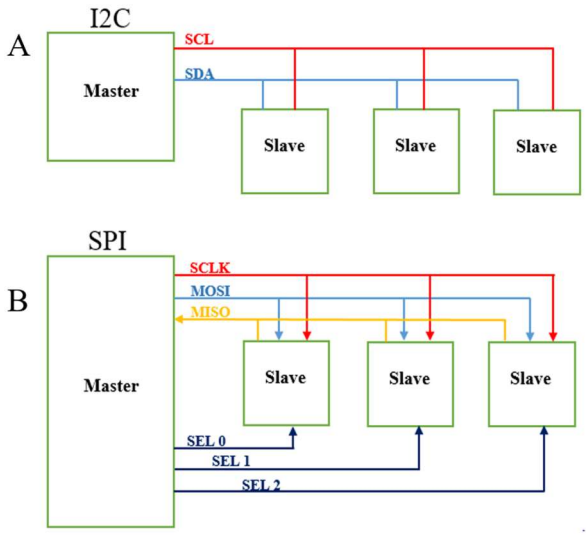

Figure 3.15 - A) I^2C and B) SPI protocols comparison. Adapted from [111].

Focusing on the communication, the selection of the slave by the master is the first step. The master selects the slave by pulling its SSn line down. Then the SCLK is activated at a particular clock frequency. This frequency is used by both master and slave. At this point, there are four possible modes of communication. Each mode is characterized by the clock polarity (CPOL) and the clock phase (CPHA). To communication be possible, the SCLK frequency, the CPOL and the CPHA of the master and of the respective slave must be equal. So, each time the master needs to communicate with other slave in a different mode, it must reconfigure these three parameters. [110]

Some differences of this protocol with the I^2C protocol were already mentioned above. However, it is worth to highlight that SPI does not have a limit data rate. Therefore, the SPI protocol is mostly used in situations where higher speed transference of data is needed. On the other side, its architecture is more complex, requiring more work to construct. [110]

3.3.3 Universal Asynchronous Receiver and Transmitter

The Universal Asynchronous Receiver and Transmitter (UART) protocol performs only asynchronous serial communication. Thus, it consists in a half-duplex, i.e. it allows both transmission and reception of data, but not at the same time. In fact, the main disadvantage of the UART protocol is that communication can only be performed between 2 devices at once. Physically, it comprises two wires named R_x and T_x. The R_x pin receives data from the other device, while the T_x pin transmits data for the device it is connected to (Figure 3.17A). No clock is implemented in this system. However a baud rate, i.e. number of bits transmitted per second, is defined at the beginning of the communication, being that for a communication to be possible, the two connected devices must work at the same baud rate. [112]

For data transference in the UART protocol (Figure 3.16), first a start bit is sent. The start bit allows the other device to know that a communication is about to initiate. Then, data is sent in bytes. Finally, a parity bit and a stop bit are sent, to error checking and communication termination, respectively. [113]

Figure 3.16 - Transference of data in the UART protocol. [113]

The major drawback of the UART protocol is the fact of it not comprises a clock, i.e., it is asynchronous. Despite an asynchronous communication facilitate the data transference between the devices, it results in more errors. Thus, a similar synchronous protocol called Universal Synchronous-Asynchronous Receiver and Transmitter (USART) is used to complement this flaw.

Physically, the USART protocol is similar to UART, being that they differ in the presence of a clock line in the USART protocol that allows the master to generate a clock signal to control data transference (Figure 3.17B). [114]

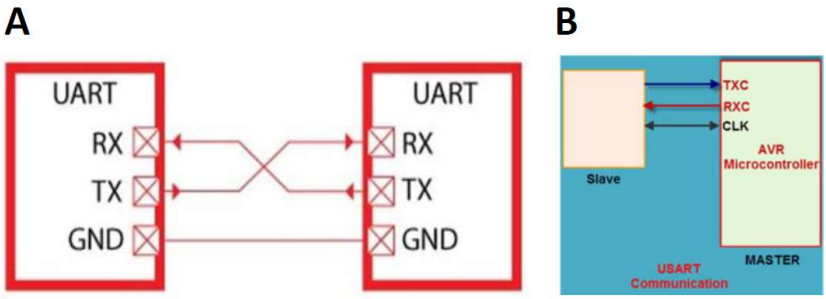

Figure 3.17 - Asynchronous and Synchronous digital protocols. A) UART. [1] B) USART. [115]

3.3.4 Generic Attribute Profile

A new form of data transference emerged with Bluetooth technology. Instead of installing cables between the devices, radiofrequencies are able to exchange data, thus achieving wireless connections. In particular, the launch of Bluetooth version 4.0 and the following ones, also known as Bluetooth Low Energy (BLE) or Bluetooth Smart, caught the attention of developers. This new technology is characterized for enabling economy of energy, making it ideal for implementing in long battery life applications. [116]

BLE contains 40 radiofrequency (RF) channels. Among the available channels, 3 are the advertising ones used for device discovery, connection and broadcast. The remaining 47 are the data channels, used for bidirectional communication between connected devices. The inclusion of cyclic redundancy checks, acknowledgements and retransmissions in the BLE inter-devices communication ensure that data is transmitted in a reliable way. In addition, BLE connections also contain encryption and decryption of data to guarantee data confidentiality. [116]

The architecture of the BLE technology consist in several layers with different purposes. Among them, is manly important to understand the Generic Access Profile (GAP) layer and the Generic Attribute Profile (GATT) layer.

The GAP layer is responsible for control connections and advertisements, i.e. it gives visibility to the device and determine if and how the devices can communicate. The important concepts defined by the GAP are central and peripheral devices. Generally, the central devices correspond to mobile phones or tablets which have more processing power and memory. On the opposite, the peripheral devices are smaller and low power and they can connect to a central device. What regards to the advertisement process, it consists on the periodic transmission of advertising packets by the peripheral device. [117]

The Generic Attribute Profile (GATT) defines how data is transferred between the devices (Figure 3.18). It also defines the concepts of GATT server and GATT client, which corresponds

to the peripheral and to the central devices, respectively, defined in the GAP layer. The exchange of data between the GATT client and the GATT server occurs at each connection interval, unless the GATT client is busy trying to establish communication with other servers. The connection interval is defined by the GATT server according to the time it takes to respond to the first GATT client request. [117]

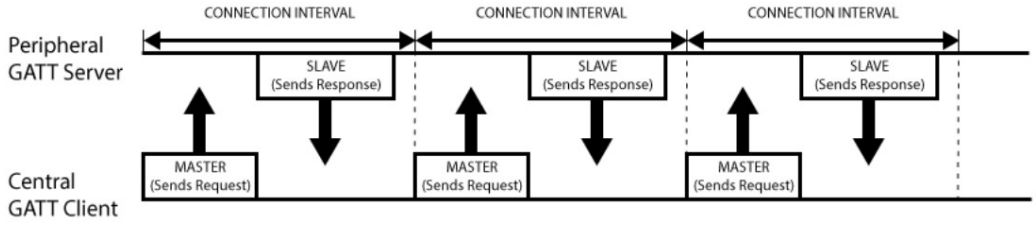

Figure 3.18 - Exchange of data between GATT client and GATT server. [117]

The exchanged data in the GATT protocol is organized in profiles, services and characteristics (Figure 3.19). A Profile simply consist in a group of services. Services, in turn, contain sets of data useful to achieve a given function of the device, e.g. battery monitoring. Thus, a service can only perform a certain function because it comprises one or more characteristics, since the characteristics contain the values to be used, either to exchange data or control information. [116] Each service and each characteristic is identified by a universal unique identifier (UUID), distinguishing them from other services and characteristics, respectively. [117]

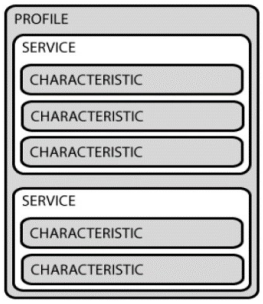

Figure 3.19 - GATT protocol transactions organization. [117]

3.4 Hardware Computer-Aided Design

The support for the improved iHandU system electronics will be a Printed Circuit Board (PCB). PCBs are becoming very useful for medical applications, once they enable the construction of smaller, less complex and lighter devices. [118]

To design the PCB, a PCB Computer-Aided Design (CAD) software must be used. There are several programs available for this effect. Among them, Altium Designer, Eagle and Kicad are the most used. Among the PCB designers, there are a lot of controversy in deciding which software is best. Online forums of users with all types of experiences, since learners until

professionals, were visited to understand the major differences between the software and decide the most suitable CAD software to use in the development of this master thesis. [119]

From what was read, Eagle and Kicad are more destinated to hobbyists and inventors. These two software are pretty similar and they are very intuitive to use when the user is learning. On the other side, Altium Designer is the software with more advanced features, being widely used in industry by professional engineers. The quality of its 3D visualization mode, its extensive libraries, the existence of a large variety of support/ tutorials and the possibility of personalization make Altium a board design software increasingly popular.

Furthermore, the Altium Designer is the PCB CAD software used in the BRAIN group, existing a really good know-how in using this software. Therefore, having into account the variety of tools Altium Designer can offer, the close help it can be obtained while learning to use it and the existence of a license provided by INESC TEC, Altium Designer was chosen to design the PCB for the new iHandU hardware. [118-120]

4

4 Development of a new Wearable Health Device

Wearable Health Devices (WHDs) are an important part of Wearable Health Systems (WHS). Therefore, when aiming to build a new WHD, the first step that must be taken is the study of its system architecture. After completing this first step, the needed components for the said WHD, the requirements they must obey and the flow of information and applicability of the full WHS will be known. Then, an analysis of the possible components specifications to be implemented in the device must be made. At this stage, the components that comply with the restrictions imposed by the system architecture are compared amongst each other and the most suitable ones are chosen to develop the device.

In this chapter, the sequential steps to develop the new wearable device, i.e., an evolution of the existing iHandU hardware, which, from now on, will be referred as iHandU_v2 device, will be described. In the beginning of this chapter, the architecture of the existing iHandU system and the conducted analysis of possible components to be integrated in the device are presented. It is important to refer that some problems arose during the iHandU_v2 device implementation, mainly due to the wrong choice of some components, better explained in 5.1. Therefore, in 4.2.5, the components that must be implemented in a future improvement of the device developed during this project are presented, being also highlighted which component of the current iHandU_v2 device must be replaced.

Subsequently, a detailed explanation on how the device was built and programmed, i.e., the Hardware and the Firmware development, is provided in this chapter. Then, a clarification of the hardware integration in the textile band is given. The textile band is an important part of the system, since it is where the device is placed during DBS surgery. Furthermore, the development of the textile band had already into account the achievements of this master thesis, providing space to integrate the force sensors and the respective cables of communication with the MCU. Following this topic, the development of a web application to visualize and record sensors data is presented. This web application was very useful not only as a debug platform during the device development, as also to perform reproducibility tests of the inertial data provided by two iHandU_v2 units produced in this master thesis. Moreover, the final topic of this chapter shows the followed methods to ensure reproducibility of inertial data.

4.1 Wearable Health System architecture

Some updates on the iHandU existing system architecture had to be made for the integration of the iHandU_v2 device. Thus, the updated iHandU system, the iHandU_v2 system, was envisioned as presented in Figure 4.1. The comfort of the patient, the components efficiency and the adaptation of the system characteristics to be used during surgery were the main influencers in the projection of the new approach.

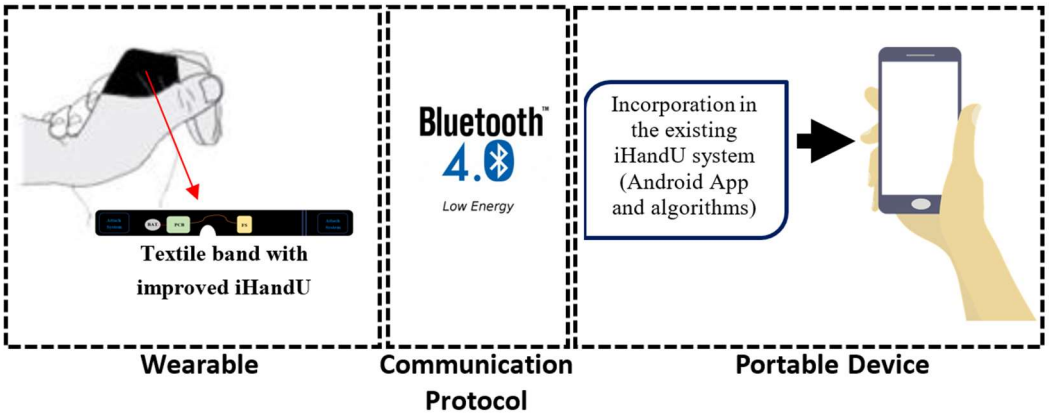

Figure 4.1 - Proposed architecture for the improved iHandU system: iHandU_v2 system.

In this new perspective, a textile band containing the system electronics is placed on the hand of the patient at the beginning of the DBS surgery. A 9 DoF IMU sensor, a MCU integrated BLE module, as well as other general components needed for power management, will be soldered in a miniaturized designed PCB. The PCB is then inserted in a pocket of the band. Force sensors were also added to the system, as well as incorporated in the band. In what concerns to data visualization, the android application of the existing iHandU system was updated by a member of the BRAIN group for it to receive sensors readings of the iHandU_v2 device, through the BLE protocol (GATT). Figure 4.2 represents the components diagram of the iHandU_v2 system.

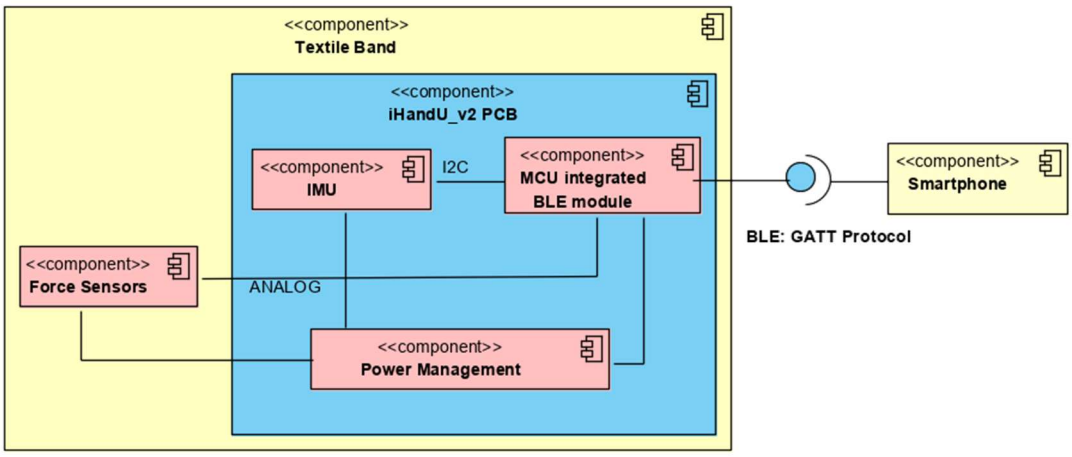

Figure 4.2 - Proposed textile design and components organization.

4.2 Components procurement for implementation device design

The study of the existing iHandU system, together with the research of developed wearable devices tracking hand's kinematics, allowed to determine the type of components needed to fulfil the needed improvements on the existing iHandU device. Therefore, at this point, it is certain that an IMU and force sensors are required. Also, a battery to power the device, a MCU to process data and to communicate with sensors and a Bluetooth module, which will transmit this data to an external device are essential.

When selecting the components, some restrictions must be made. It is of paramount importance to keep in mind the operating voltage of the circuit, which in this particular case, is of 3.3V, since it is the most typical work tension in microelectronics. Therefore, it must be assured that all components work at a voltage compatible with this value. Certainly, for each component there are other particular restrictions that must be taken into account. These are discussed in the following topics.

Comparative tables of IMUs, force sensors, MCU integrated Bluetooth modules and batteries are also presented. In each table the components are organized by price. Studying and comparing the components characteristics of each table enabled the choice of the specific components to implement in the device. In specific, after confirming voltage compatibility in between the components, the main decisive factors to choose each component were their low power consumption, low cost and small size. In each table the chosen component is highlighted in green.

4.2.1 Microelectromechanical Systems: Inertial Measurement Units

The Inertial Measurement Units (IMUs) are the key device in the scope of this project, since their data allows the determination of the hand kinematics. In what regards to these sensors, they must have 9 DoF (3-axis gyroscope, 3-axis accelerometer and 3-axis magnetometer), because, despite the rigidity changes quantification algorithm only uses gyroscope data, the data from the two other sensors can be useful for future implementations of algorithms evaluating other parameters. Furthermore, the implementation of the I^2C protocol to establish the communication between inertial sensor and the MCU is preferred. The reason is that this protocol has a more simplistic architecture to implement on the hardware, since it uses only two active wires to establish communication between devices, and its range of data rate is more than enough for this application. Also, the minimal size of this sensor is crucial. Thus, having into account these main restrictions, the IMUs on Table 4.1 were found and compared.

Table 4.1 – IMUs specifications.

Name	MPU-9250	ICM-20948	LSM9DS1	BMX160
Manufacturer	InvenSense	TDK InvenSense	STMicroelectronics	Bosch Sensortec
DoF	9-axis	9-axis	9-axis	9-axis
Gyroscope range	±250 dps; ±500 dps; ±1000 dps; ±2000 dps	±250 dps; ±500 dps; ±1000 dps; ±2000 dps	±245 dps; ±500 dps; ±2000 dps	±125 dps; ±250 dps; ±500 dps; ±1000 dps; ±2000 dps
Accelerometer range	±2g; ±4g; ±8g; ±16g	±2g; ±4g; ±8g; ±16g	±2g; ±4g; ±8g; ±16g	±2g; ±4g; ±8g; ±16g
Magnetometer range	±4800 µT	±4900 µT	±4 G; ±8 G; ±12 G; ±16 G	±1300 µT; ±2500 µT
Size	3mm x 3mm x 1mm	3mm x 3mm x 1mm	3.5mm x 3mm x 1mm	2.5mm x 3mm x 0.95mm
Operating Voltage VDD	2.40V – 3.60V	1.71V – 3.60V	1,90V - 3,60V	1.71V – 3.60V
VDD IO	1.71V - VDD	1.71V – 1.95V	1.71V - VDD+0.1V	1.20V – 3.60V
Serial Interface	I2C/SPI	I2C/SPI	I2C/SPI	I2C/SPI
Price (u.p.)	3.90 €	4.24 €	4.75 €	5.26 €

All the four presented IMUs have in common the fact of having of 9 DoF and being able to transmit data through the I^2C protocol.

The LSM9DS1 is the biggest one, so it was the first to be discarded. On the other hand, the BMX160 is the smallest IMU, but also the most expensive of the four, being also discarded.

ICM-20948 and MPU-9250 are very similar. In fact, the ICM-20948 is the subsequent version of the MPU-9250 produced by TDK InvenSense. Moreover, TDK InvenSense announced that the MPU-9250 will be discontinued. So, despite MPU-9250 being cheaper, the ICM-20948 was chosen to be integrated in the iHandU_v2 device, ensuring the implementation of most recent and updated components. However, the ICM-20948 has a disadvantage. The range of its I^2C lines voltage supply values (VDDIO) does not extends to the operating voltage of the iHandU_v2 device, i.e. 3.3V. This means that the sensor needs two supply voltages, one for general purposes (3.3V) and one for I^2C communication purposes (1.8V). Therefore, when integrating the ICM-20948 on the device, a voltage regulator is needed to create the supply voltage of 1.8V. Also, a level translator must be integrated in the device to transform the signals coming from the MCU at 3.3V in the same signals, but at 1.8V, to feed the IMU I^2C lines.

4.2.2 Force Sensors

With the incorporation of force sensors, it is aimed to determine the magnitude of the force made by the clinician in the patient's hand during DBS surgery. In the DBS surgeries, occurring at Hospital S. João, the way clinicians hold the patients' hand is being observed. This analysis enables the definition of the number and shape of the sensors to implement, as well as the place(s) to incorporate them in the textile band. Having this into account, size and shape are of utmost importance when choosing the force sensors. Several hypothesis are presented in Table 4.2.

Table 4.2 - Force Sensors specifications.

Name	FSR0 (1,2 & 3) CE	FSR 400-408	Single Tact	FlexiForce A401 & 101
Manufacturer	Ohmite	Interlink Electronics	Single Tact	Tekscan
Type	Force Sensing Resistor	Force Sensing Resistor	Capacitive	Piezoresistive
Active area shape	Squared Round Rectangular	Round Squared Strip	Round	Round
Active sides length/ diameter (mm)	39.70 x 39.70 25.42 604.60 x 10.20	Several	8.00	24,5 3.80
Thickness (mm)	0.375 0.425 0.375	0.3 – 0.41	0.35	0.208 0.203
Pins	2	2	3	2
Proper electronic	no	no	yes	no
Price	8.81€ - 16.34€	7.49€ - 15.49€	18.00€	22.51€ - 33.57€

Force Sensing Resistors (FSRs), Piezoresistive and Capacitive force sensors were analysed.

The capacitive sensor, manufactured by SingleTact, is too complex. The need of its own electronics could compromise the low-cost feature and mostly, the small size of this project.

In addition, the piezoresistive sensors from Tekscan are more appropriated for measuring bending forces instead of force magnitudes caused by touch. Furthermore, they are also the most expensive.

The Interlink Electronics FSR 400 series sensors were chosen to implement in the system. This series of sensors include rectangular, squared and rounded sensors of different sizes. Its lower cost and mainly its diversity of size and shape justify the choice, since it is not yet known

the most profitable shape and size of the force sensors to implement in the system. Meanwhile, for the first tests, the round shape sensors of two different sizes, already existing in the lab, were used.

It is relevant to mention that it is expected that further tests with these sensors in clinical environment will enable a more objective decision on the size, shape and number of force sensors to be incorporated in the iHandU_v2 system.

4.2.3 Microcontroller & Bluetooth

Besides the sensors, a MCU is required to achieve data processing and to communicate with the sensors and with a Bluetooth module, which, in turn, is required to transmit data to external devices. The low power consumption and the miniaturized size of these components were evaluated to allow a more advantageous decision.

Aiming to reduce the hardware size, a solution that integrates the MCU in a Bluetooth module was considered. MCU integration in a Bluetooth module saves space on the device, enabling the maximum miniaturization of the system hardware. Furthermore, this solution does not compromise the required features of each component.

As referred in previous sections, the implementation of the most recent and low power technologies is aimed. Hence, only modules with Bluetooth versions from 4.0 and further were considered. Regarding data processing, the number of bits used in the analog-to-digital conversion, memory and velocity characteristics of the MCU were taken into account.

Six MCU integrated Bluetooth module are presented in Table 4.3.

Table 4.3 - MCU integrated Bluetooth Modules specifications.

Bluetooth Module	BGM111	AMS002	SPBTLE-1S	BMD-200	PAN1740	BT900
Manufacturer	Silicon Labs	Silicon Labs	STMicroelectronics	Rigado	Panasonic	Laird
Bluetooth Version	4.2	4.1	4.2	4.2	4.1	4.0
Size (mm)	12.90 x 15.00 x 2.20	17.60 x 11.40 x 2.40	11.50 x 13.50 x 2.00	17.00 x 17.00 x 1.90	9.00 x 9.50 x 1.80	19.00 x 12.50 x 2.50
Number of bits (ADC)	12	10	10	10	10	12
Velocity (MHz)	40	24	32	16	16	40
Flash memory (kB)	256	8000	160	256	n.s.	n.s.
RAM (kB)	32	n.s.	24	32	42	n.s.
Price	5.55 €	8.02 €	9.72 €	10.42 €	12.17 €	16.59 €

From the found modules, the PAN1740 is the smallest one, but it is also the second most expensive. The BT900, the BMD200 and the AMS002 are larger in size, what makes them unsuitable for this project.

The SPTLE-1S is slightly smaller than BGM111. However, the BGM111 is not only the cheapest MCU integrated Bluetooth module found, but it also uses a higher number of bits in the analog-to-digital conversion, has higher velocity and larger memory. Moreover, this chip has been used in several projects developed in the lab, what provides more confidence on the component and easiness to program it. For those reasons, BGM111 was the chosen MCU integrated Bluetooth module to implement on the device.

4.2.4 Battery

A battery is needed to deliver power to the system. In the study of possible batteries to implement in this project, only the rechargeable ones were considered, to guarantee a longer duration of this component. Furthermore, coin cell batteries were thought as the most appropriated, since they occupy the minimum space, being possible to attach them to the PCB. However, batteries with other shapes but still small in size were also analysed.

Table 4.4 specifies some important characteristics of possible batteries to implement in the wearable device. Besides the shape and size, the voltage and capacity values of the batteries were compared. Batteries providing voltage values of 3.3V or higher and capacities between 50 and 200mAh are preferred, since 3.3V is the work voltage of the device and it is firstly estimated a power consumption lower than 10 mA, based on the main components consumptions referred in their respective datasheets. Furthermore, due to their potential for yield higher capacity values and their low self-discharge [121], the research focused on Lithium-ion batteries only.

Table 4.4 - Batteries specifications.

Name	LIR2032	LIR2450	RJD2032C1	RJD2048	LP 402025 1S-3	LP 401235 1S-2
Manufacturer	EMB	EMB	Illinois Capacitor	Illinois Capacitor	Bak	Bak
Battery chemistry	Lithium ion	Lithium ion	Lithium ion	Lithium ion	Lithium-ion	Lithium-ion
Shape	Coin cell	Coin cell	Coin cell	Coin cell	Rectangular cell	Rectangular cell
Size (mm)	20.0 (d)	24.5 (d)	20.0 (d)	20.0 (d)	26 x 20	38 x 12.6
Thickness (mm)	3.2	5.0	3.5	5	3.8	4.25
Nominal Voltage (V)	3.6	3.6	3.7	3.7	3.7	3.7
Capacity (mAh)	45	120	85	120	155	120
Price	4.33 €	4.39 €	7.62 €	11.49 €	16.49 €	21.23 €

Coin cell batteries have the advantage of being small in size and low in price. Consequently, it was opted to implement a coin cell battery with 20mm diameter, existing three possible options.

The RJD2048 was discarded due to its higher thickness of 5 mm. LIR2032 and RJD2032C1 have quite similar characteristics. The main difference between them relies on their capacity. LIR2032 provides a current capacity of only 45 mAh, which can be not enough for ensure the autonomy of the wearable during DBS surgeries. Therefore, the RJD2032C1 battery, with a capacity of 85mAh, was chosen to be implemented in the device.

4.2.5 Other components

Beyond the main components, above referred, other auxiliary components must be implemented in the device to assure its power management and board programming.

First, the selected coin cell battery requires a battery holder. This holder was chosen based on appropriate size and minimal thickness. Since the battery is rechargeable, a charger is also needed. When choosing the charger, the charging current of 0.5CA (Capacity in Amperes), advised in the battery datasheet, was taken into account. In addition, a microUSB connector was implemented in the circuit to allow the charging of the battery via cable and a slider button was added to turn on and off the device.

Besides these components, two voltage regulators and a voltage translator, to fulfil the ICM-20948 requirements, are needed. The main difference between these two components is that a voltage regulator is used to fix a specific constant voltage, being mainly used to provide supply voltages. On the other hand, the voltage translator, is used to transform a digital signal at a certain voltage level in the same digital signal but at a different level of voltage. So, with the voltage translator the properties of the signal are not lost.

In this way, the TPS71533 DCKR voltage regulator was used to fix a supply voltage of 3.3V (VCC) and a provided current of 50mA. As only exception, the ICM-20948 needs a supply voltage of 1.8V (VCCIO). VCCIO must be provided by the TPS71518 DCKR. However, in the iHandU_v2 device was implemented a voltage divider circuit to create this voltage. Unfortunately, the voltage divider circuit brought problems to the developed hardware, which are better explained in 5.1.3. The voltage translator, in turn, performs the transformation of the signal coming from the BGM111 at 3.3V level in the same signal at 1.8V level, acceptable by the ICM-20948, and vice-versa.

Finally, a MCU programmer was added to load the firmware in the device and enable its debug. Several capacitors and resistors of a 0402 size were also used.

Table 4.5 contains the specification of the above mentioned components

Table 4.5 – Other components specification.

Component	Component class	Functionality
Keystone Electronics Corp. 3003	Battery Holder	Fixate the battery in the PCB.

MCP73831T-2ATI/OT	Battery Charger	Charges the implemented rechargeable battery.
USB629105105921	Micro USB connector	Connector to promote the charging of the battery.
CUS - 12TB	Button	Turn on and off the device.
TPS71533 DCKR	Voltage Regulator	Regulate the voltage and current coming from the battery at 3.3V and 50 mA, respectively.
TPS71518 DCKR	Voltage Regulator	Regulate the voltage and current coming from VCC at 1.8V and 50 mA, respectively.
LSF0204	Voltage Translator	Do the conversion of 3.3 to 1.8V (voltage needed for the ICM20948 to work).
FTSH-105-01-F-D-K	MCU Programmer	Enable the loading and debug of the firmware in the device.

4.3 Hardware Development

Once the architecture of the system has been defined and the components to integrate have been decided, the hardware design is the first task to accomplish to develop the device.

For the hardware development, the Printed Circuit Board (PCB) must be designed in a CAD software and the components need to be ordered and welded in the board.

In this topic, a detailed explanation on how the PCB was designed and soldered is provided. So, first, a clarification on how the components are organized in the board and how they connect is given. Subsequently, it is given an explanation on how the components were positioned in the board, exposing a 2D and a 3D visualization of the referred board achieved with the Altium Designer software. Finally, the welding techniques used to construct the device are shown.

Once again, it is important to refer that due to some errors made during the design of the hardware, clarified in 5.1, the presented schematics and Altium Designer board visualizations, do not exactly correspond to the built iHandU_v2 device, shown in Figure 4.15. In fact, schematics and the Altium Designer board visualizations are already updated to avoid the occurrence of these errors in a future development of the iHandU device.

4.3.1 Components design and integration

The Altium Designer software was used to design the PCB where the components were soldered. Designing a PCB includes the concretization of several sequential tasks. To start, two libraries must be created: the Schematics Library and the PCB Library. The first library includes the pin out diagrams of all components, while the PCB Library contains the footprints of each component. Then, an association of the pin out diagrams and respective footprints of each component is made. Furthermore, it is also possible to download 3D models of each component, which provides a 3D visualization of the board in a step ahead.

Once libraries are created, the schematics associated to each component or group of components must be designed. This information is available on the datasheets of each component. However, the input of BRAIN research members was also needed. In Figure 4.3 there is an example of the pinout diagram, footprint and schematic of the ICM-20948.

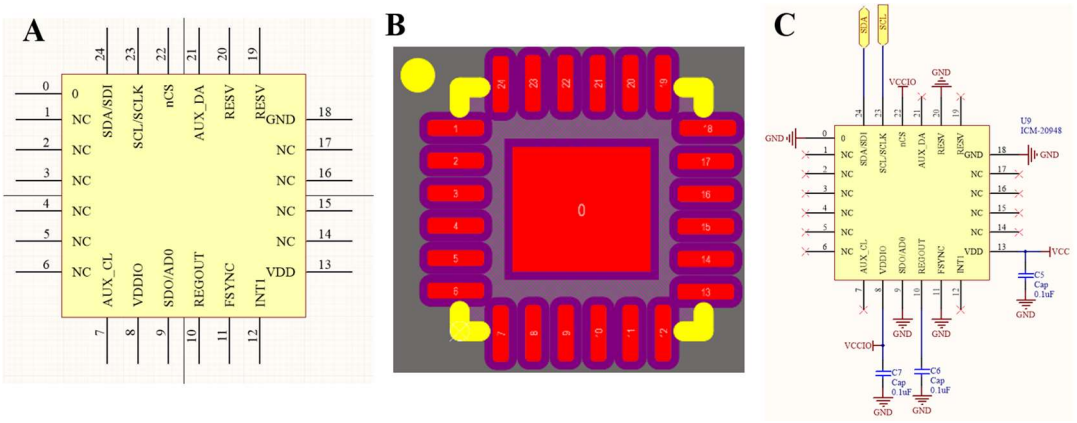

Figure 4.3 - ICM-20948 design in Altium Designer. A) Pin out diagram. B) Footprint. C) I²C communication schematic.

After creating all the schematics, a main one must be created. Here, the connections between the already designed schematics are established as presented in Figure 4.4.

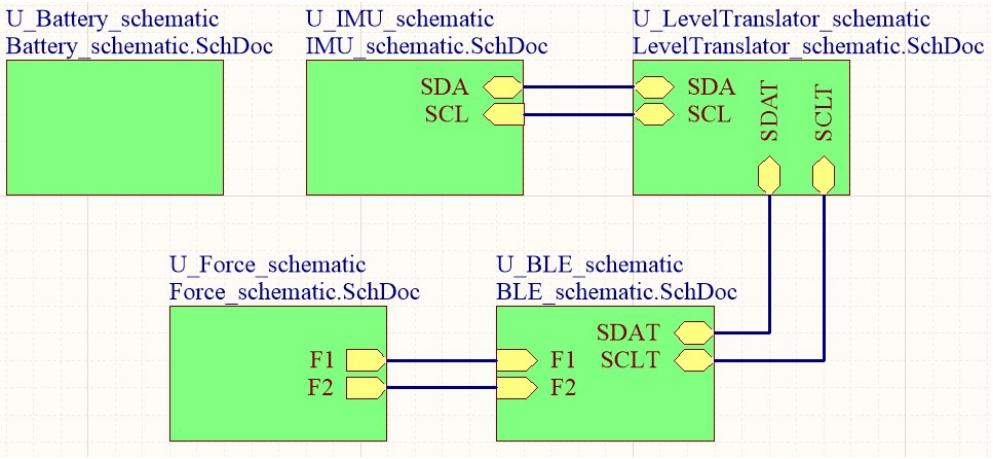

Figure 4.4 - Overall schematic of the board.

Finally, the schematic files are imported to a PCB document, where the challenge is to position the components in a minimal area possible, without compromising the connections between them, which must also be established at this stage. Finishing that, the size and shape of the final board can finally be set.

In the following topics, all the schematics will be presented and explained.

4.3.1.1 Inertial Measurement Unit

Figure 4.5 represents the circuit of the inertial sensor adapted for I²C communication. As can be seen, the sensor is fed with two different voltage supplies: VCC and VCCIO. VCC is the operating voltage of the circuit (3.3V), while VCCIO is the voltage used to feed the I²C lines of the component, i.e. the SDA and SCL pins. The pin AD0 (pin number 9) is connected to the ground. The logical level of this pin determines the Least Significant Bit (LSB) of the I²C address of the device. The possibility to set the last bit is useful to distinguish two similar inertial sensors in the same device. In this particular case, there is only one inertial sensor and the LSB of its I²C address is set to 0.

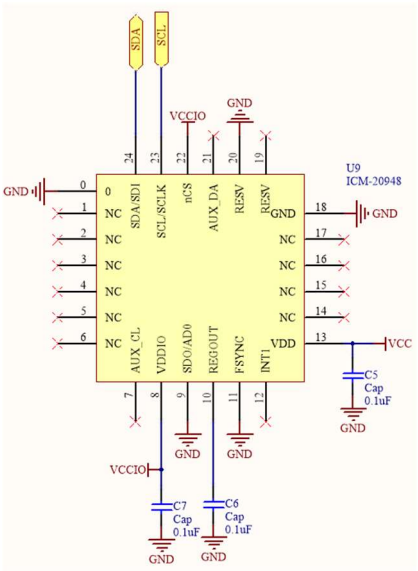

Figure 4.5 - I²C adapted schematic of ICM-20948.

4.3.1.2 Voltage Translator

A voltage translator is needed due to the incompatibility of voltage values between the ICM-20948 and the BGM111. The design of the circuit (Figure 4.6) was made according to the recommendations of the component datasheet. On the A side, i.e. the left side, the lowest voltage (VCCIO = 1.8V) must be connected, thus corresponding to the side of the ICM-20948. Therefore, the SDA and SCL signals coming from the ICM-20948 will connect to the input/output entries of this voltage translator side. In the opposite side, i.e. the B side, the VCC (3.3V) supply voltage will be connected, so corresponding to the BGM111 side. Thus, the SDA and SCL signals coming from the BGM111 will connect to the input/output entries of this voltage translator side. The OE pin must be set to high in order to enable the device.

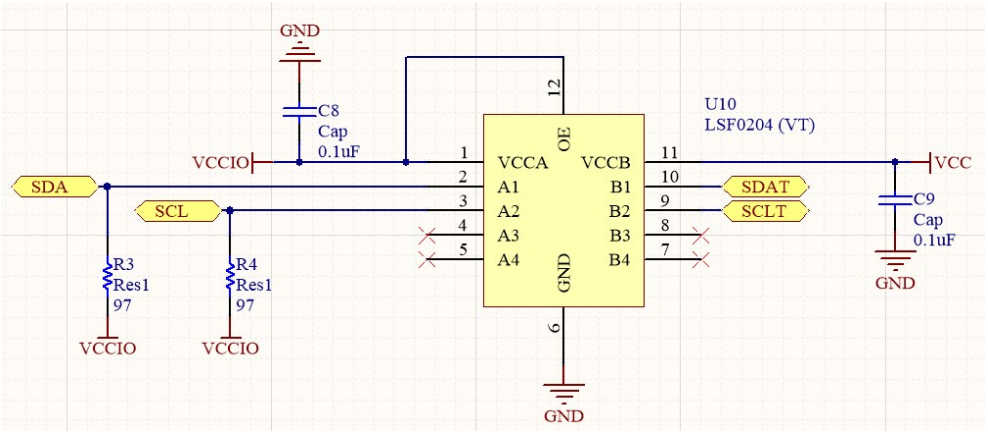

Figure 4.6 - Voltage translator schematic.

4.3.1.3 MCU integrated Bluetooth module with programmer

In Figure 4.7, the schematic of BGM111 and the respective connector required to program and debug it (FTSH-105-01-F-D-K) are represented. Similarly to the previous components, the BGM111 standard circuit was designed accordingly to its datasheet. Pins 18 and 19 are the I^2C communication lines (SDA and SCL); the outputs of the force sensors are connected to the analog ports 5 and 6 of the BGM111; pin 7 is the reference voltage for the analog force sensors, being that it should be connected to VCC Analog. However, due to a mistake made in the PCB design, referred in 5.1.1, this pin was connected to VCCIO. The consequences of this error are clarified in 4.3.1.4.

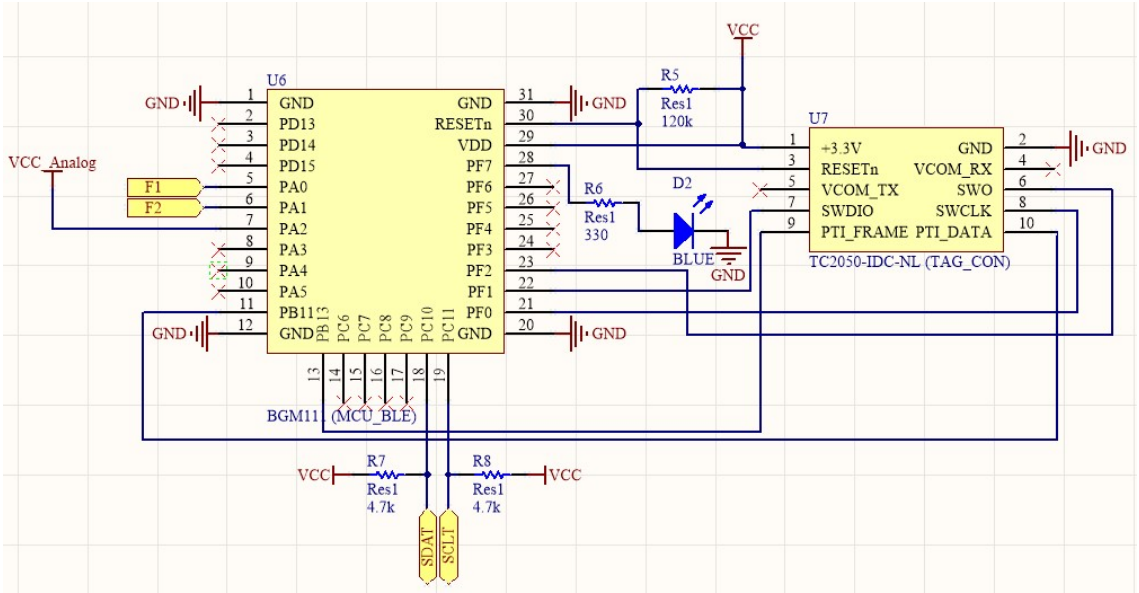

Figure 4.7 - BGM111 and FTSH-105-01-F-D-K schematic.

4.3.1.4 Force Sensors

Once it is the first time force sensors are implemented in the iHandU system, two Force Sensing Resistors (FSR) with similar shape (round) but different sizes were included in the device. In this way, it will be possible to analyse, in a near future, which force sensor is more suitable for the purpose.

The schematic circuit of the analog force sensors (Figure 4.8) are based on a voltage divider circuit.

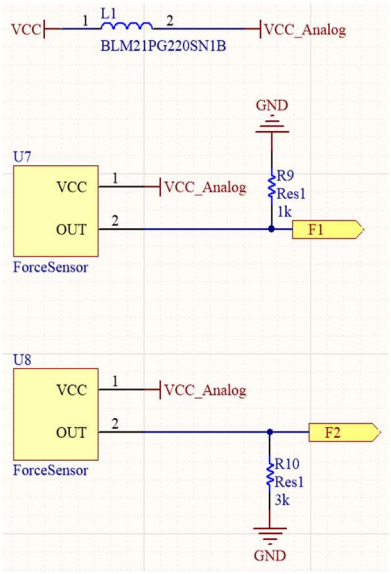

Figure 4.8 - Force sensors schematic.

As already mentioned, when force is applied to a FSR, its resistance decreases. So, having into account the above schematic (Figure 4.8), the force applied on the sensors and read on the analog ports of the BGM111 is in voltage units, being computed according to the equation of the circuit presented in 4.1.

$$V_{OUT} = \frac{R_{FIXED}}{(R_{FIXED} + R_{FSR})} \cdot VCC_{Analog} \quad \textbf{4.1}$$

Being that, VCC_{Analog} is the reference voltage of the voltage divider circuit and it has the same value as VCC (3.3V). It results from the connection of an inductor to VCC, as visible in Figure 4.8, to eliminate noise and create more stable channels of VCC and VCC_{Analog}.

The fixed resistors values (R_{FIXED}) for each sensor were chosen according to the graph in Figure 4.9, also provided in the datasheet of the sensor. This graph shows the behaviour of a FSR output voltage depending on the applied force, in grams, for several fixed resistors. The presented lines were made for a voltage reference of 5V. However, in the case of this project, the voltage reference is 3.3V. So, experimentally, the behaviour of each fixed resistor value was slightly different from what was expected.

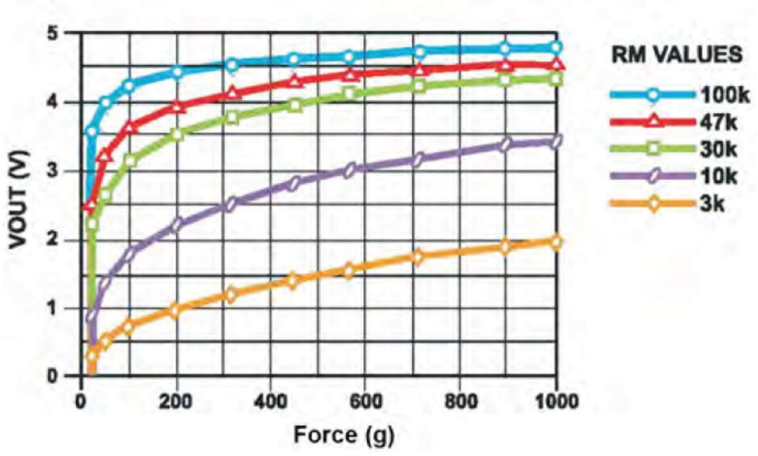

Figure 4.9 - Force vs Vout curves for a standard FSR in a voltage divider configuration.

According to what was read in these sensors datasheet, they present a range of a few grams until a bit more than 1000g of force. Therefore, to be sure that these sensors were fitting for the purpose of the project, a weight scale was grabbed in a similar way that doctors grab the patients' hand during DBS surgery. This test was performed by different subjects, allowing to conclude that a grabbing similar to the one of rigidity evaluation in the operating room will trigger a variation of force between 50g and 1300g.

Having into account the pretended force range and based on the observation of the graph of Figure 4.9, a fixed resistor of 10kΩ seemed to be the most appropriated to implement in a first attempt.

However, since it was explicit in the sensors datasheet that the theoretical results of Figure 4.9 referred to standard FSR with a voltage reference of 5V, and not 3.3V, and that the sensors have hysteresis, there was the need of designing calibration lines for each one of the force sensors used in the system. The calibration would allow the choice of the most suitable fixed resistor for each force sensor. Moreover, force sensors calibration also enabled the conversion of the sensors output from voltage to grams units.

Thus, a graph of weight, in grams, in function of the sensor output voltage, in mV, was made. Taking into account the pretended sensors range of weight (from 50g to 1300g), output voltage of the sensors when submitted to weights from 50g to 1300g in steps of 100 were measured. With a 10kΩ resistor, the calibration lines of both sensors saturated to fast. Therefore, these resistors were switched by ones of 3kΩ. For the big sensor, the desired sensitivity was obtained, being that its calibration line is presented in Figure 4.10A. For the smaller one, a 3kΩ resistor originated a still saturated curve. So, for the smaller force sensor circuit was implemented a 1kΩ resistor, that originates the calibration line presented on Figure 4.10B.

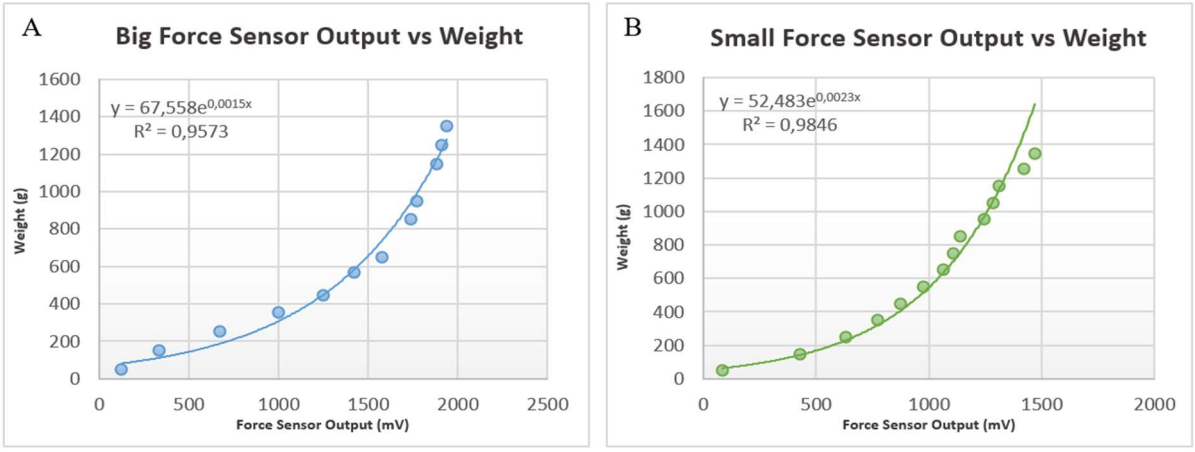

Figure 4.10 - Force sensors Calibration. A) Big force sensor calibration line ($R_{FIXED} = 3k\Omega$). B) Small force sensor calibration line ($R_{FIXED} = 1k\Omega$).

Values above 1300g were discarded, once they are out of the sensors range, and values under 50g were also discarded due to lack of sensitivity of the sensor. Because the sensitivity of the force sensors can slightly change from sensor to sensor, the obtained exponential trend lines must be employed in the code of the developed debug platform mentioned in 4.6.

4.3.1.5 Power management

The following schematic (Figure 4.11) represents the power management circuit of the device. It consists in the battery, the battery charger, the USB connector, the button and two voltage regulators.

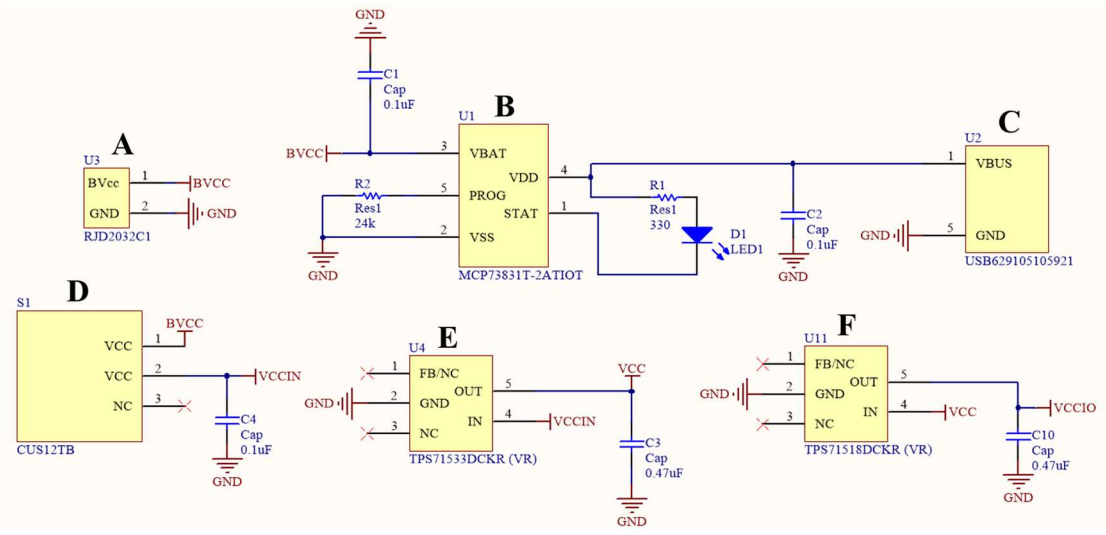

Figure 4.11 - Battery management circuit. A) Battery. B) Battery charger. C) USB connector. D) Button. E) Voltage Regulator – 3.3V. F) Voltage Regulator – 1.8V.

Figure 4.11A represents the battery, where BVCC corresponds to its voltage. BVCC can go until 4.2V, when the battery is fully charged, or 5V while it is charging. To charge the battery,

a cable is connected to the microUSB entry (Figure 4.11C). From here, the voltage flows to the VDD entry of the charger (Figure 4.11B). The VBAT pin of the charger is the battery charge control output and, for this reason, is connected to the its BVCC pin. As referred before, the battery must be under a charging current of 0.5CA, i.e. 42.5 mA (recalling that the capacity of the chosen battery is 85mA). To regulate this current, the resistor R2, of 24kΩ, was added to the charger circuit. This value was defined according to equation 4.2, presented in the charger datasheet.

$$I_{REG} = \frac{1000V}{R_{PROG}} \quad \textbf{4.2}$$

Where, R_{PROG} is the resistor that must be implemented in the system to obtain the desired charging current, in $k\Omega$, and I_{REG} is the charging current, in mA. Knowing that, for the chosen battery, I_{REG} must be $42.5mA$, the value of R_{PROG} can be found through equation 4.3.

$$R_{PROG} = \frac{1000V}{42.5mA} = 23.5k\Omega \approx 24k\Omega \quad \textbf{4.3}$$

The battery circuit also includes all the other needed components for the device operation. In Figure 4.11D is the button. The battery management circuit is only active when the button is on. So, when it is on, this component has VCCIN as output. VCCIN has the same voltage as BVCC, but it is connected to a capacitor to remove noise. In turn, VCCIN is the input of the voltage regulator in Figure 4.11E. This regulator has a constant output of VCC (3.3V) that will feed all the components in the board. Finally, there is also a second voltage regulator (Figure 4.11F) of the same family of the first that will fixate the voltage at 1.8V needed to supply the voltage translator and the ICM-20948 digital lines.

It is important to recall that this second voltage regulator is not actually implemented in the developed device, as referred in 4.2.5.

4.3.2 Hardware design

Having completed the design of the schematics, these were imported to a PCB file. In this file, the components are automatically organized in blocks according to the schematics they belong. However, instead of being represented by their designators, each component is represented by its footprint.

Having into account the number of components and their respective dimensions, it was decided that a two layers PCB would be enough for building the device. Therefore, the components could be put on the top layer or on the bottom layer of the PCB.

The decided strategy to positon the components consisted in place the battery and its respective holder in the bottom layer. These components occupy a large part of this layer, letting only the corners empty. So, the remainder components must be positioned on the top layer, without overcoming the dimensions of the battery holder. In this way, taking into account the size

of the battery holder (22mm x 20mm), the estimated size of the PCB must be around the same values. In this way, it is guaranteed the construction of the smallest board possible, when included batteries of the same size as the chosen one.

So, the components started to be placed in the top layer of the board according to their schematics. Only a small component (voltage regulator) and some resistors and capacitors were positioned in the corners of the bottom layer. To correctly perform this task, it is important to have in mind the connections between the components. It is not a good practice to position connected components far away of each other.

After organizing all components and establishing the connections between them, a board with 24.250 mm x 21.593 mm was obtained, accomplishing one of the goals of this project: obtain a smaller device. The 2D design of the final board can be seen in Figure 4.12.

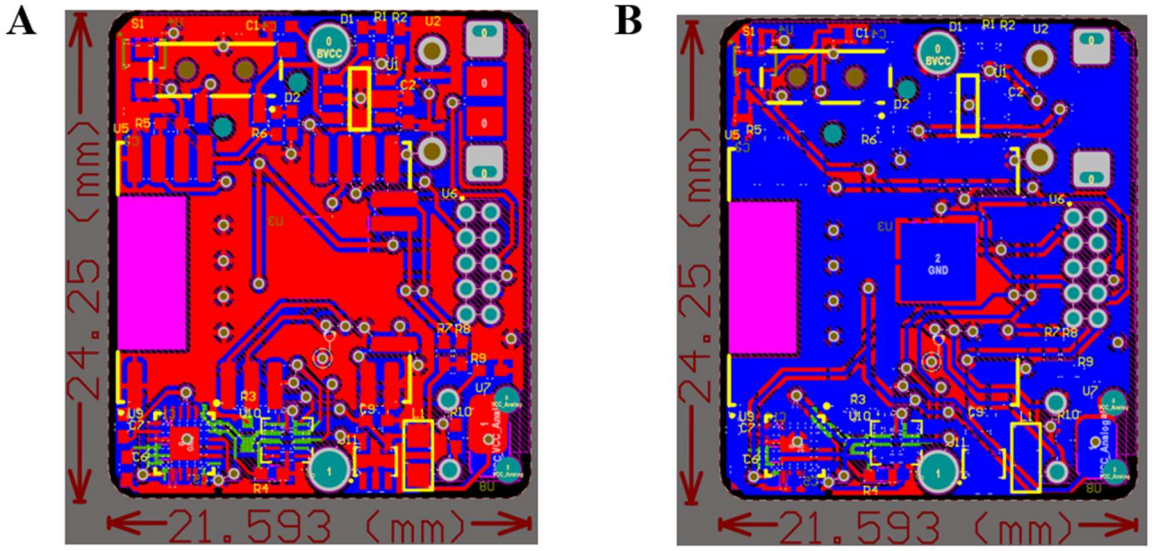

Figure 4.12 - iHandU_v2 2D view of PCB. A) Top layer. B) Bottom layer.

Once the 3D models of each component were downloaded, the Altium software allows for a 3D view of the board (Figure 4.13).

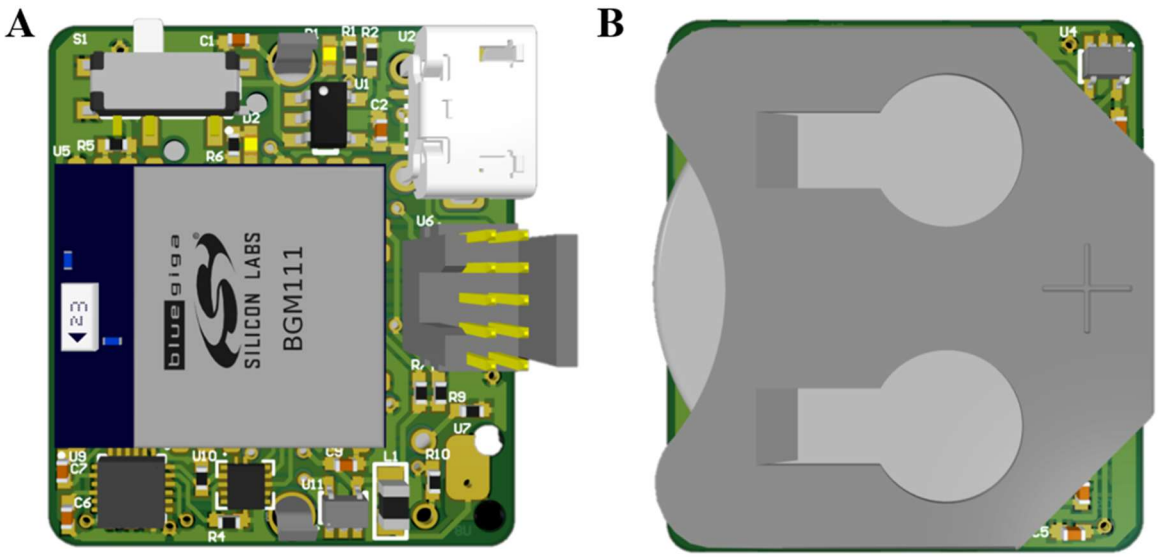

Figure 4.13 - iHandU_v2 3D view of PCB. A) Top Layer. B) Bottom Layer.

4.3.3 Hardware production and assembling

After concluding the PCB design, the Altium software allows to generate Gerber files that contain all the information needed to produce the board. The board was ordered in a Belgian company, already known by the group, called Eurocircuits. The Gerber files were submitted in the web site of the company and, after the specialists revise these files and make sure no errors exist or rules are inflicted, the PCB took about 7 work days to arrive to the lab. The price of each PCB decreases as the quantity ordered increases, so, despite the intention of soldering two boards only, five PCBs were ordered.

While waiting for the PCBs to arrive, it was exported from the Altium the Bill Of Materials (BOM) to achieve the list of the components to buy. The components were bought online in Mouser, except for the battery which was bought in Arrow website.

When finally the PCBs and the components were in the lab, the welding phase started. To solder the boards, two equipment were used: an iron (Figure 4.14A) and a rework (Figure 4.14B). The rework was only used to solder components in which the pads are located underneath, i.e. the BGM111, the ICM-20948 and the voltage translator. The remainder components were all soldered using the iron.

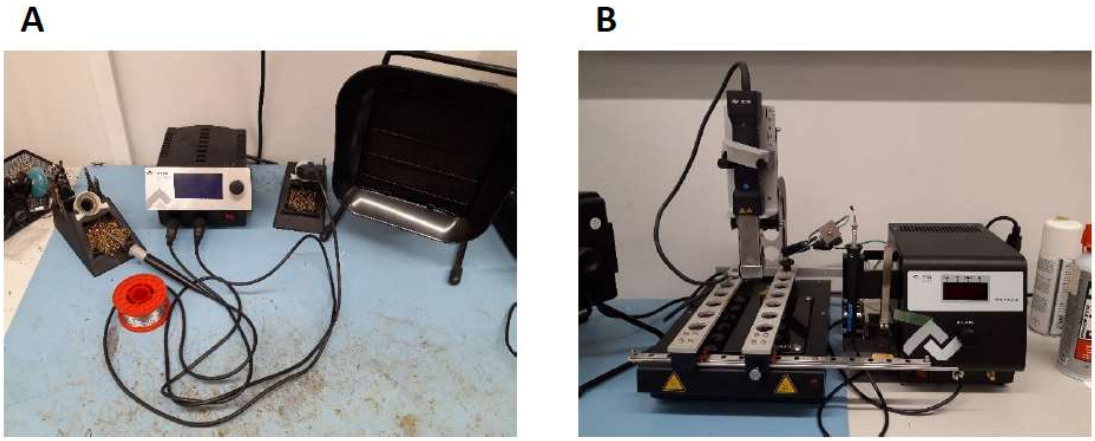

Figure 4.14 - Figure 4.15 – Welding equipment. A) Iron. B) Rework.

The final assembled device is represented in Figure 4.15.

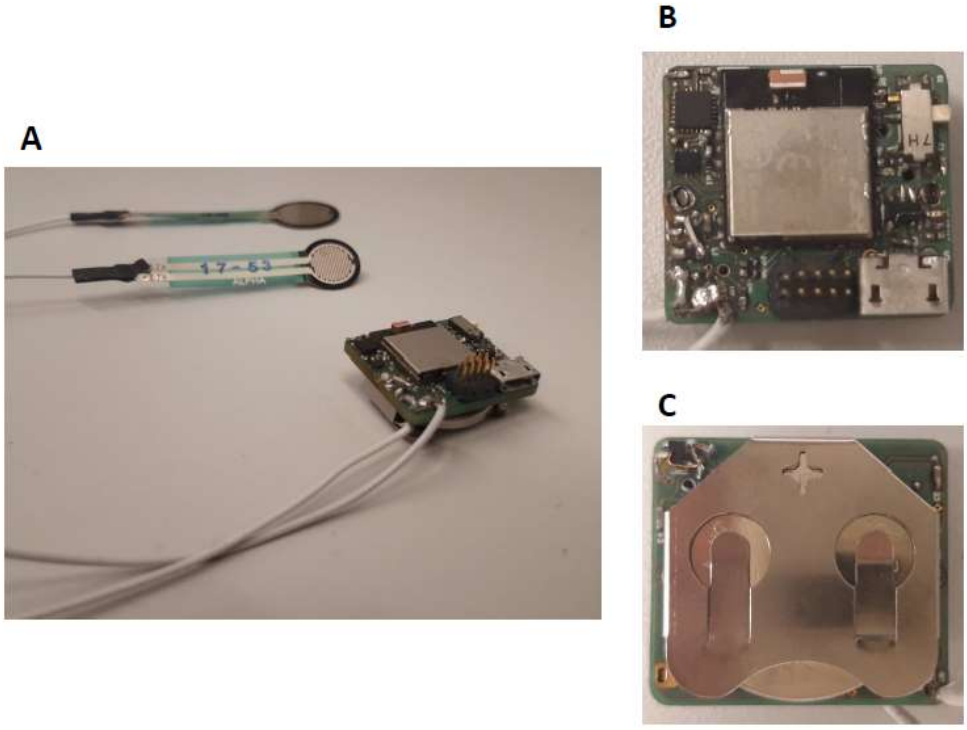

Figure 4.15 - Final hardware. A) Completed device. B) Top Layer. C) Bottom Layer.

As mentioned along this chapter topics, some errors were made during the development of the iHandU_v2 device. Therefore, the device presented in Figure 4.15 has some differences in relation to the design presented in 4.3.2, which already contains all the corrections made. Once again, these corrections are referred in 5.1.

4.4 Firmware development

The development of the firmware was made using C programming language in a Silicone Labs Integrated Development Environment (IDE) called Simplicity Studio. This IDE has the particularity of including a panoply of tools that brings a lot of advantages in relation to the competition. In fact, Simplicity Studio includes tools for energy profiling, configuration and wireless network analysis, demos, software examples, documentation, technical support and community forums. Furthermore, it provides code for device initialization and configuration of the Bluetooth stack, which is a major advantage that supported the firmware development during the learning phase.

So, for the device firmware, two source files were created: one that contains all the functions needed to exchange data between the MCU and the ICM-20948 through I^2C, explained in 4.4.1, and other with the code to read the analog ports of the MCU where the force sensors are connected, presented in 4.4.2. In addition, the code for the Main file explained in 4.4.3 was also made.

4.4.1 ICM-20948 Firmware

Recalling the I^2C communication protocol, explained in 3.3.1, the communication between the ICM-20948 (slave) and the BGM111 (master) is made through two communication lines: SDA and SCL. The SCL is the clock line that works as pacemaker to the information flow, allowing a synchronization between the master and the slave, while the SDA is the line that transmit the data, being that each bit transmitted in the SDA line corresponds to one pulse of the SCL line. According to this protocol, the communication between the two components can only be established if the master firstly establishes a start condition. For ICM-20948 the start condition is defined as a high to low transition of the SDA line while SCL line is high (Figure 4.16). Together with the start condition, the master must also send the I^2C address of the inertial sensor. This sensor identification address is constituted by seven bits, where the last one can alternate between 0 and 1 according to the connection of AD0 pin, explicit in 4.3.1.1. This is useful to distinguish a specific sensor when several similar sensors are implemented in a device. Moreover, to this I^2C address must be added an eighth bit, that gives information to the slave if the master is going to perform a reading or a writing process.

After identifying it, the BGM111 can communicate with the ICM-20948 through eight bit registers. The ICM-20948 comprises a high number of registers that allow the performance of several tasks, such as:

- Sensors initialization.
- Accelerometer and gyroscope configurations of full scale range, bandwidth and sample rate.
- Accelerometer and gyroscope readings.

- Independent interaction with the magnetometer (initialization, configuration and readings).
- Status checking.
- Device reset.
- Sensors self-tests.

Moreover, the master and the slave must always acknowledge each received byte (Figure 4.16) by pulling down the SDA line during the 9th pulse of the clock signal. The exchange of data ends when the master establishes a stop condition (Figure 4.16), which is defined as a low to high transition on the SDA line while SCL is high.

The following tables present the flow of information between the ICM-20948 and the BGM111 when the master is writing (Table 4.6) and reading (Table 4.7) one byte of data to and from the slave, respectively.

Table 4.6 – Write data to a specific Register Address: Single-Byte Write Sequence.

BGM111 (Master)	Start bit	Device I²C Address + W	Specific Register Address		Data	Stop bit
ICM-20948 (Slave)		ACK		ACK	ACK	

Table 4.7 – Read data from a specific Register Address: Single-Byte Read Sequence.

BGM111 (Master)	Start bit	Device I²C Address + W	Specific Register Address	Start bit	Device I²C Address + R		NACK	Stop bit
ICM-20948 (Slave)		ACK	ACK		ACK	Data		

In the case of a Single-Byte Read Sequence, a not acknowledge signal (NACK-when the SDA line remains high) exists after the slave sends the data, being sent together with the stop bit by the master. The NACK signal means that the master will stop receiving data from the slave.

Despite only the Single-Byte Write/Read Sequences being here presented, Burst Write/Read Sequences, where several bytes of data is exchanged, instead of a unique byte, are also possible and it was implemented in the system firmware.

Due to the high number of ICM-20948 registers, these are divided in four banks, from bank 0 to bank 3. Each bank is also represented by a particular register address, the Bank Register. In this way, before sending the registers that correspond to each one of the ICM-20948 tasks, as the ones referred above, first the master must send the register that specifies the bank where the register it intends to write or read belongs (Bank Register), avoiding communication conflicts.

Therefore, the flow of data between the ICM-20948 and the BGM111 always start with a Single-Byte Write Sequence to select the bank in which the register address belongs. This sequence is similar to the one presented in Table 4.6, where the “Specific Register Address” is

the Select Bank Register, which states the bank that will be chosen, and the "Data" is the Bank Register. After selecting the bank, the exchange of data is different if the master intends to read from the ICM-20948 or to write on it. In the first case, a Read Sequence similar to the one presented in Table 4.7 follows the Select Bank sequence. In the second case, the Select Bank sequence is followed by a write sequence as the one shown in Table 4.6.

Figure 4.16 shows the SDA and SCL signals observed in the oscilloscope of a Single-Byte Read Sequence of the WHO-AM-I register, register that must return the ICM-20948 Reset Value, confirming that it is receiving data with no errors.

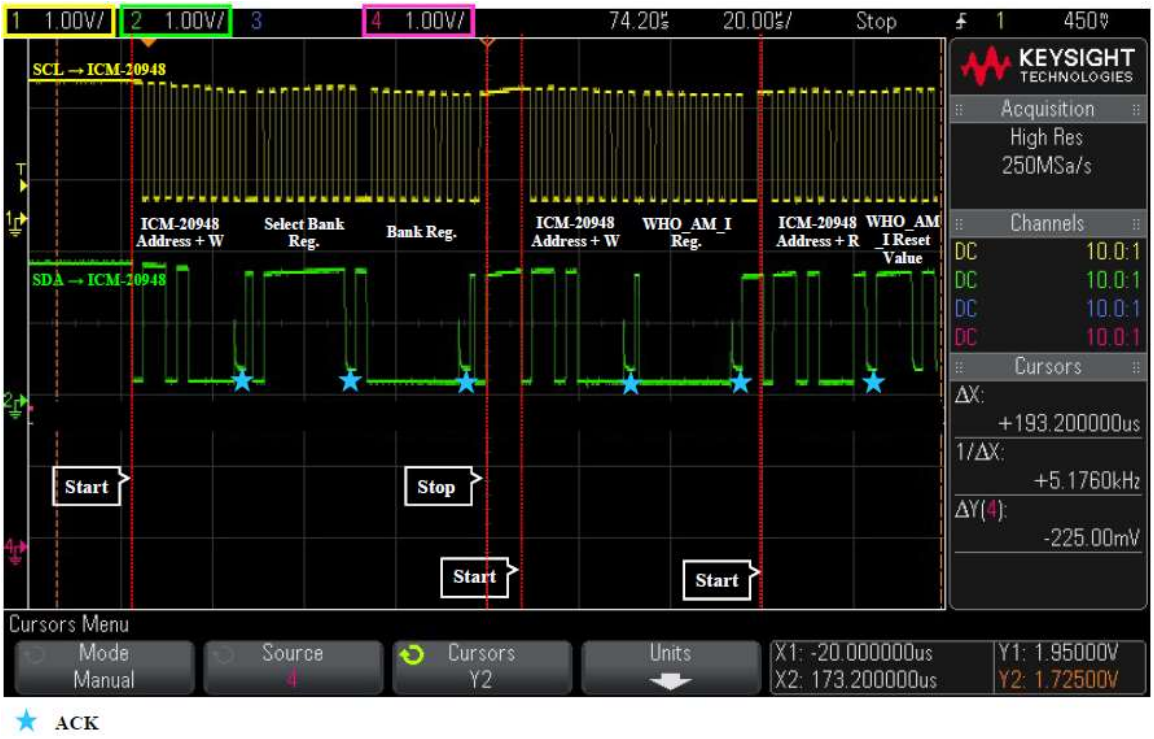

Figure 4.16 – Single-Byte Read Sequence of the WHO-AM-I register. I²C communication signals: SCL in yellow; SDA in green.

Regarding the implemented code related with the ICM-20948 communication, first generic functions to select the bank register, read data and write data, being that the amount of data to read or write was an input of the functions, were created.

The ICM-20948 contains two dies in a unique package, where in one die is the accelerometer and the gyroscope and in the other die is the magnetometer (AK09916). This magnetometer acts as a slave of the ICM-20948 component. This is made by enabling the Master I2C Serial Interface, as can be seen in Figure 4.17. With that being said, functions to interact with the magnetometer only must be implemented.

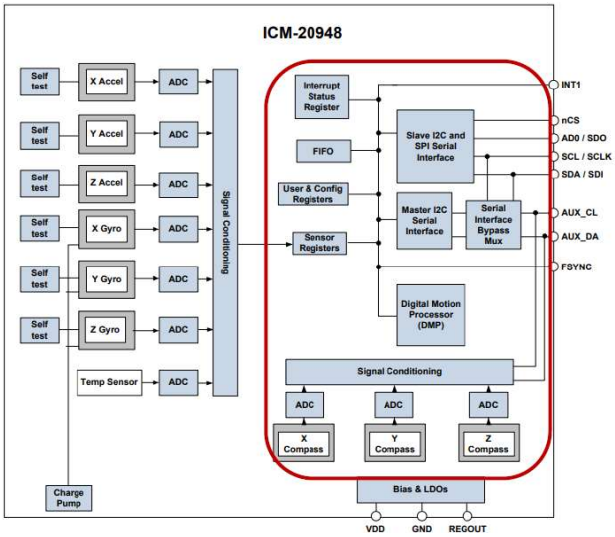

Figure 4.17 - ICM-20948 block diagram.

Among the created functions needed to establish communication between the ICM-20948 and the BGM111, it is important to highlight the following ones for:

- Accelerometer and gyroscope initialization, where are defined the configurations of full scale range, bandwidth and sample rate.
- Magnetometer initialization, where it is reset and set to single mode measurement.
- Accelerometer, gyroscope and magnetometer data reading and respective conversion to float numbers.
- Accelerometer and gyroscope calibration, where the mean of 300 readings is write in offset registers that are then subtracted to the current sensors readings.
- Sensor reset.
- Enable and disable sensor sleep mode.

The fact of the magnetometer be a separated component of the accelerometer and the gyroscope made its communication difficult to obtain. Furthermore, due to the lack of time was not possible to obtain a successful calibration of the magnetometer.

4.4.2 Force sensors Firmware

What regards to the force sensors firmware, three functions were used for:

- ADC channels initialization, where the ADC clock is enabled, is defined the ADC resolution (12 bits), the reference voltage to use (VCC) and the ADC channel to read.
- Data conversion from bits to voltage units.
- Get data.

Thus, with the above mentioned ADC configurations, 4096 levels ($2^{12} = 4096$) to represent 3300mV are defined, originating a sampling resolution of 0.8mV.

4.4.3 Main code & Bluetooth Firmware

Several developed examples provided by Simplicity Study were analysed in detail to help in the initialization and configuration codes of the device and of the Bluetooth stack, respectively, developed in the Main file.

This file starts with the device initializations and Bluetooth configuration. Then, it contains a while loop where first, five samples of each of the five sensors of the device are read and then data is sent to an android or web application through a BLE command in a unique array. Figure 4.18 represents the activity diagram of the code in the Main File.

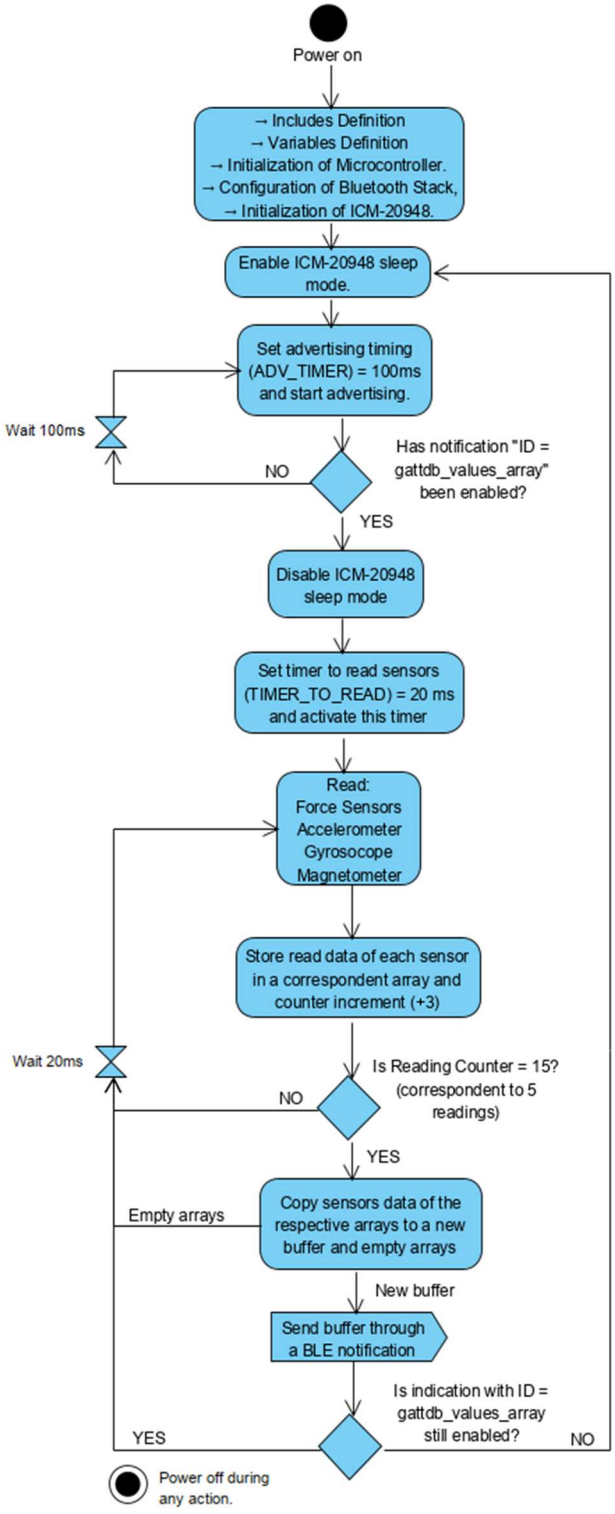

Figure 4.18 - Main code activity diagram.

While the firmware was being developed, the battery management circuit of the device was not being used. Therefore, the device was being powered by the computer through the evaluation board of the Blue Gecko Module Wireless Starter Kit, provided by Silicone Labs Company. This kit contains the referred evaluation board with multiple sensors, a screen, a BGM111, a BGM121

and multiple connectors for external devices, helping starters to develop simple firmware. Figure 4.19 presents the system setup while the firmware was being developed.

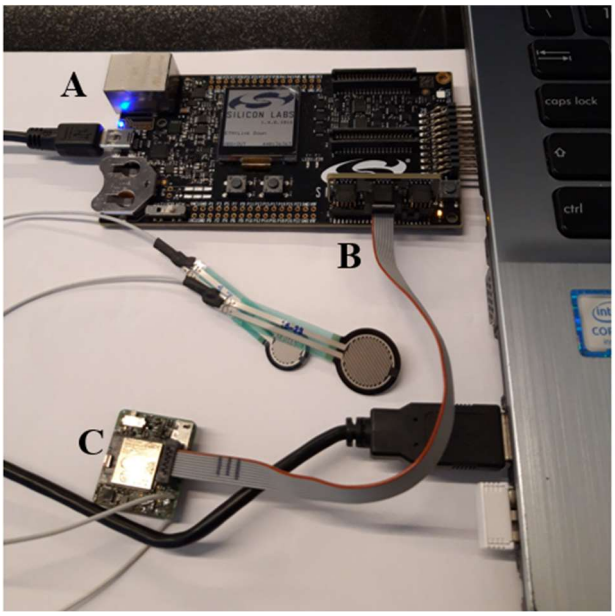

Figure 4.19 - System setup during Firmware development. A) Evaluation board. B) Connector. C) iHandU_v2 device.

After the initializations, the ICM-20948 is put in sleep mode, since it is not being used yet. This is one more method of power saving. Once the device and the Bluetooth configuration are ready, the Bluetooth module starts sending advertisement packets at each 100ms until the connection is established.

The GATT Profile of this project contains four services (Figure 4.20). Three of them are common in the software examples provided by Simplicity Studio software. Though, the fourth one, named SensorValues, was created to allow the exchange of the sensors readings between the GATT server (iHandU_v2 device) and the GATT client (smartphone/web application). This service has only one characteristic, named ValuesArray. The ValuesArray characteristic is identified by an ID = gattdb_values_array.

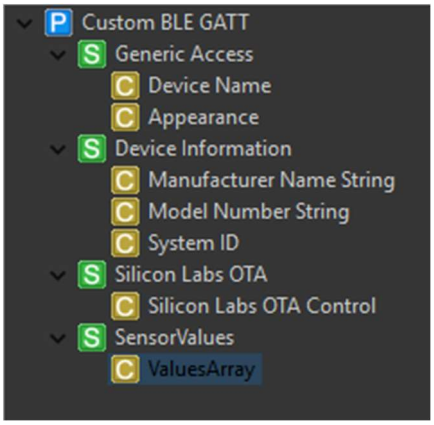

Figure 4.20 - iHandU_v2 project GATT Profile.

So, when the gattdb_values_array notification is enabled in the GATT client, a timer to read the values measured by the iHandU_v2 sensors is set to 20ms. This means that, while the mentioned notification is enabled, at each 20ms the values of the sensors will be read and stored in a buffer, corresponding to a sampling rate of 50Hz, frequency which corresponds to the sensors reading frequency of the previous iHandU device.

A unique reading from the ICM-20948 returns nine float values (three for the accelerometer, three for the gyroscope and three for the magnetometer). Moreover, a reading from each force sensor returns one float value, which gives a total of 11 float values read at each 20ms.

After performing a power consumption study with the Energy Profiler tool of Simplicity Studio, presented in 5.2, it was decided that the sensors data will only be sent when 5 readings of each sensor occurred. Thus, at each reading, i.e. at each 20ms, the read values are stored in a buffer. After 100ms, the buffer contains 55 float values, corresponding to 5 readings of each sensor. At this instant the buffer is sent to the smartphone/web application through a BLE command. After sending the readings to the client, the array is empty to avoid possible interferences from previous or subsequent readings.

A float number need four bytes to be represented in an unsigned integer form. Therefore, the ValuesArray characteristic was set to transport a 220 bytes array ($55\ floats \times 4\ bytes = 220\ bytes$), and send it to the smartphone through a notification. The array with the sensors values is organized as in

Table 4.8.

Table 4.8 - Organization of the sensors values array.

Sensor	Accelerometer	Gyroscope	Magnetometer	Small Force Sensor	Big Force Sensor
Float Elements	0:14	15:29	30:44	45:49	50:54
Bytes	0:59	60:119	120:179	180:199	200:219
Example	$a_{x1}\ a_{y1}\ a_{z1}$ $a_{x2}\ a_{y2}\ a_{z2}$ $a_{x3}\ a_{y3}\ a_{z3}$ $a_{x4}\ a_{y4}\ a_{z4}$ $a_{x5}\ a_{y5}\ a_{z5}$	$g_{x1}\ g_{y1}\ g_{z1}$ $g_{x2}\ g_{y2}\ g_{z2}$ $g_{x3}\ g_{y3}\ g_{z3}$ $g_{x4}\ g_{y4}\ g_{z4}$ $g_{x5}\ g_{y5}\ g_{z5}$	$m_{x1}\ m_{y1}\ m_{z1}$ $m_{x2}\ m_{y2}\ m_{z2}$ $m_{x3}\ m_{y3}\ m_{z3}$ $m_{x4}\ m_{y4}\ m_{z4}$ $m_{x5}\ m_{y5}\ m_{z5}$	f_{s1} f_{s2} f_{s3} f_{s4} f_{s5}	f_{b1} f_{b2} f_{b3} f_{b4} f_{b5}

If the gattdb_values_array notification is disabled or the device is disconnected, the advertising timer is set to zero and then restarted.

4.5 Form-factor and textile design

In what regards to the textile, the BRAIN group has a partnership with the Petratex Company for the development of new textile prototypes. With the input of their knowledge, the appropriated materials and design of the band was decided to fulfil a set of desirable characteristics:

- Biocompatibility and suitability for surgical environments: a flexible, breathable and clean textile. (D. Dias 2019, personal communication, January)
- Easy to maneuverer: a thin textile, simple to put and remove, with adjustable size. (D. Dias 2019, personal communication, January)
- A band able to be used on the left or right hand of the patient. (D. Dias 2019, personal communication, January)

In parallel with this thesis project, the BRAIN group developed and interacted with Petratex Company to produce the textile band where the iHandU_v2 hardware will be placed during DBS surgeries. Several iterations of this product were made according to the obtained clinical feedback. The final version is represented in Figure 4.21.

Figure 4.21 - Final iteration of the textile band. (D. Dias 2019, Personal Communication, August)

In the scope of this master thesis, the evolution process of the referred textile band was followed, since some of its design characteristics had taken into account the iHandU_v2 hardware, as the case of the force sensors inclusion.

Due to intellectual property issues, all the designs and respective details about the textile band evolution, performed by the investigation centre, can't be part of this document body. For that reason, they will be presented in Annex III, which will not be published and will only be shared with the evaluation members of this thesis. This annex has the unique objective to show the work followed during this master thesis and what has been learned to evaluation effects and it cannot be disseminated in media and for other purposes.

Despite being not presented, in the body of this master thesis, the details about the textile band, it is of utmost important to understand how the hardware was integrated in the referred textile. Thus, an explanation about how the PCB and the force sensors were introduced in the band is given in the following topic, 4.5.1.

4.5.1 Hardware Textile Integration

The textile band previously introduced contains two pockets, one for the force sensors and other for the PCB, linked through a narrow channel. This channel was created to allow the passage of the cables connecting the force sensors to the PCB. To establish the referred connection, coaxial cables were used. These cables are composed by the following four layers:

- Outer plastic sheath
- Woven copper shield
- Inner dielectric insulator
- Copper core

Thus, a coaxial cable is able to conduct two different signals through its copper layers, which is an advantage for establishing the connections between the two force sensors and the PCB in a simpler and cleaner way. With that being said, the woven copper shield and the copper core were welded to each one of the two pins of the force sensors, conducting respectively the reference (VCC Analog) and the variable analog signal, as represented in Figure 4.22. After welding the force sensors to the respective cables they were integrated in the band using glue on specific locations of their pocket. These locations were determined according to the way doctors grab the patients' hand during the DBS surgery. The cables were then introduced through the narrow channel to be welded on the PCB. As projected in the PCB design, the cables were welded in opposite layers of the PCB for a question of saving space. To prevent the copper core to break when stretched, the coaxial cable must pass through a hole on the PCB, reaching the opposite layer, from where it was introduced, and then the copper core and the woven copper shield are welded in their respective pads (Figure 4.22). After welding the coaxial cables of the two force sensors to the PCB, a hardware that is integrated in the textile is achieved.

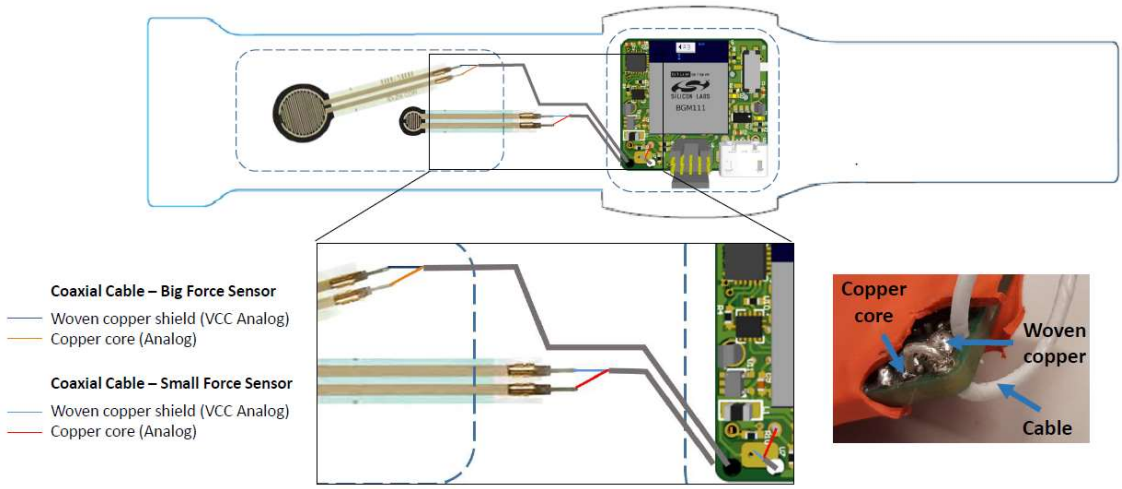

Figure 4.22 - Developed hardware integration in the textile band (force sensors cables and PCB connection).

4.6 Web Cross Platform Application

Data visualization is of higher importance to debug and confirm the reliability of the received data. A JavaScript and html code establishing the communication between a Bluetooth device and the chrome browser has been developed by a member of the Brain group. This code was studied to understand the programming language in order to be able to design a web specific platform for the iHandU_v2 device.

In the scope of this master thesis, four graphs, one for the accelerometer readings, one for the gyroscope readings, one for the magnetometer readings and one for both force sensors readings, were generated. Moreover, in addition to the already existing “Connect” and “Disconnect” buttons, “Download Values” button was also created to enable the download of the sensors data in a CSV format. The four graphs displayed in the developed web page interface are represented in Figure 4.23.

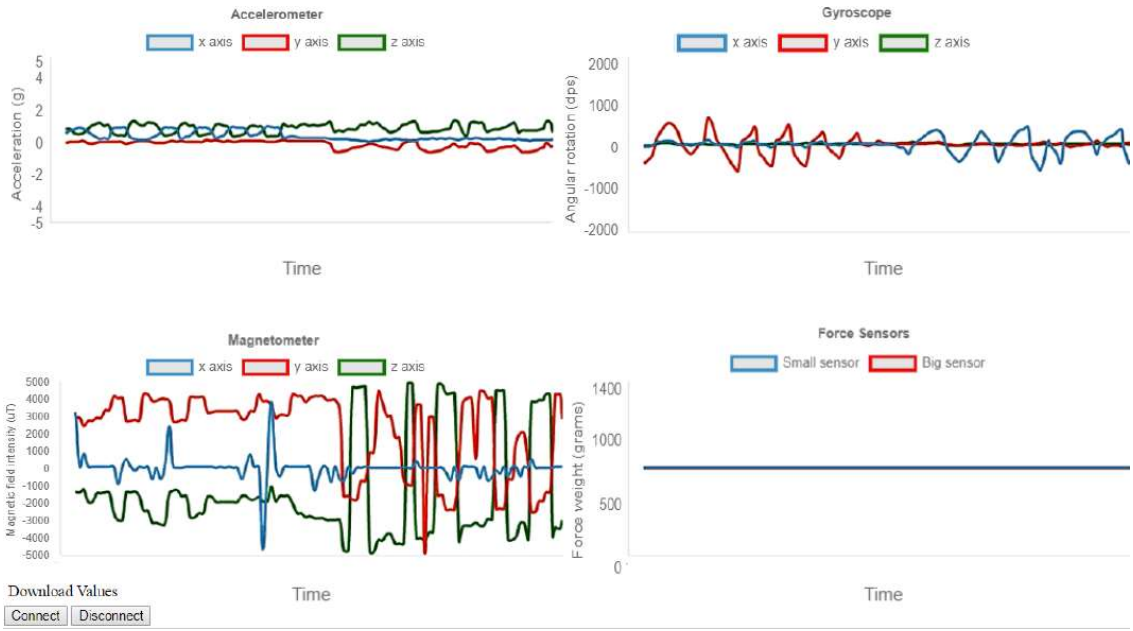

Figure 4.23 - Web application page.

The display details of the graphs, like labels, titles, colours and axes scales were set in the JavaScript file. Furthermore, in this file are the functions with the actions to perform when each one of the three buttons are clicked. When the "Connect" button is clicked, it shows up a window with a list of the possible Bluetooth devices to connect. After selecting the iHandU_v2 device, the desired service and characteristic are got through their respective Universally Unique Identifiers (UUIDs). Then, notifications for the desired characteristic are enabled and the sensors readings start. Each reading is converted from uint32 to float values. Finally, data are ready to be displayed in the respective graphs. The "Disconnect" button simply performs the disconnection of the Bluetooth Device. After disconnecting, if the "Download Values" button is clicked, the download of the CSV file to the computer with all the sensors read values occur.

This web application was really helpful during the firmware development and the sensors calibration. In particular, the accelerometer and gyroscope values in the CSV file were used to perform reproducibility tests of the inertial data, better explained in 5.1. This application also supported the force sensors calibration, enabling the real time reading of the force values. Furthermore, the calibration equations of these sensors must be introduced here, allowing for possible needed updates. Finally, in a situation of mass production of the system, this application can be useful to perform verification tests of the inertial data at the end of the production line.

The workflow diagram of the implemented JavaScript code is in Figure 4.24.

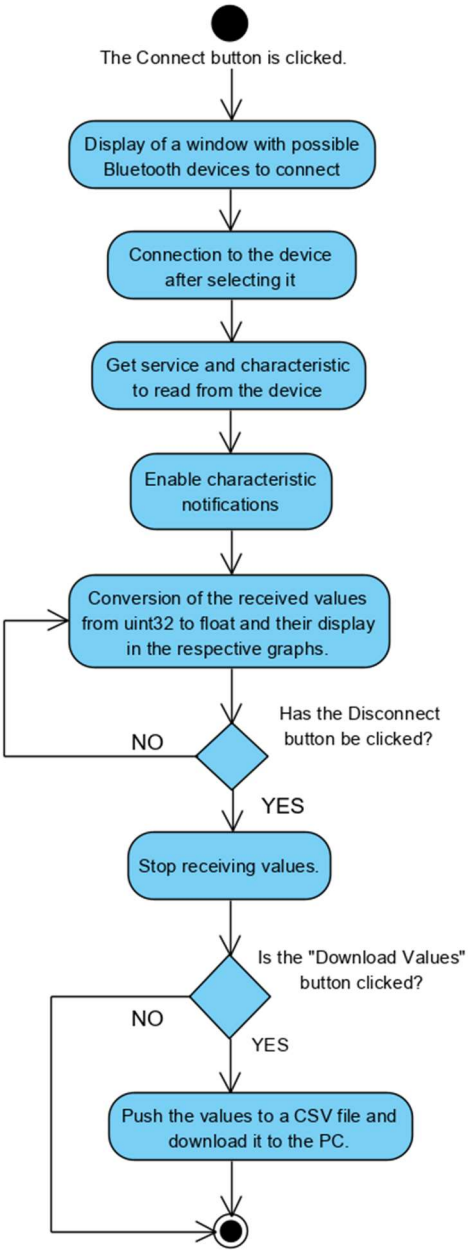

Figure 4.24 - Activity diagram of Web Application code.

4.7 Development of Device Reproducibility Tests Methods

The construction of two similar devices was important to guarantee the reproducibility of the inertial data collected by similar sensors implemented in different iHandU_v2 units. In order to evaluate the reproducibility and the reliability of the accelerometer and gyroscope data, the two developed units of the iHandU_v2 device were submitted to a damped pendulum movement. The

reproducibility tests consisted in the comparison between the theoretical and the experimental linear acceleration and angular velocity curves. To ensure reproducibility of data from different sensors, it is expected that the comparison factors between the experimental curves of each device with the theoretical curves be very similar. Further details about these tests performance are presented in 5.4.

In this topic, the tasks executed before being able to make the reproducibility tests are stated. The first task was to construct a pendulum, from which the theoretical values of linear acceleration and angular velocity can be determined. Thus, when subject to the pendulum movement, the developed iHandU_v2 units must provide similar results of linear acceleration and angular velocity as the theoretical ones. In this way, the theoretical motion equations of a damped pendulum were studied in order to obtain the theoretical graphs of the pendulum linear acceleration and angular velocity. These graphs are achieved through an algorithm implemented in Matlab. Due to the difficult of analytically determining the pendulum damping coefficient, an algorithm, also in Matlab, was developed to estimate this variable. Having experimentally determined the damping coefficient, the damped pendulum equation was solved and the theoretical graphs of linear acceleration and angular velocity in function of time were obtained. Furthermore, simple processing steps were made to the experimental curves, in order to be able to compare them with the theoretical ones.

In the following, the pendulum construction is firstly explained. Then, the motion equation of a damped pendulum is deducted. And, in the end of the topic, the algorithm to compute the damping coefficient for this system is clarified.

4.7.1 Calibration & Reproducibility Workbench: A Pendulum

When designing the pendulum, it was important to make sure that the iHandU_v2 device kept the same orientation when under the pendulum movement. Thus, a simple wire could not be used as the typical string of pendulum experiments. This because the wire can easily rotate on itself when in motion and can also go to different directions, changing the iHandU_v2 device orientation. The string problem was overcame by projecting a unique custom piece as pendulum (Figure 4.25). Of course, it is not a typical neither ideal pendulum, but its characteristics were taken into account on its motion equation deducted ahead. The pendulum system was envisioned together with BRAIN members, who helped in the pendulum design in a CAD software, to enable its printing in a 3D printer. To ensure the device keeps static in the pendulum, two hooks were included in the location where the device must be placed, which allow the iHandU_v2 device not to fall or move, since it is hold by elastics. Besides the 3D piece, i.e. the pendulum, more components were needed to construct the whole system. For making the pendulum rotate, a bearing placed inside a wooden board was used, where its external ring was glued to the wood to prevent its movement. The pendulum is then attached to the internal ring of the bearing that is free to rotate. To make the attachment, a screw, two washers and two nuts were used. A cardboard

with marked angles in relation to the pendulum direction in rest position was also included in the system to infer about the pendulum initial angular position. The pendulum setup is depicted in Figure 4.25.

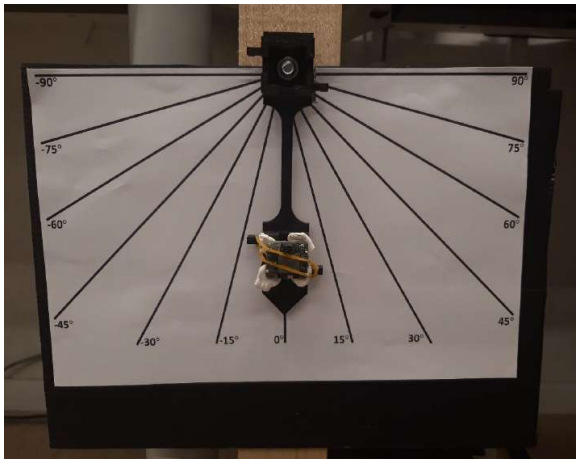

Figure 4.25 - Pendulum setup.

4.7.2 Pendulum Motion Equations

Since the system consists in a damped pendulum, the drag forces acting on the pendulum when it is in motion must be taken into account. There are five forces affecting this system: the force due to gravity (F_G), the force caused by the string (F_S), the bob drag force (F_{DB}), the string drag force (F_{DS}) and the bearing drag force ($F_{Dbear.}$). The forces diagram of the system is visible in Figure 4.26.

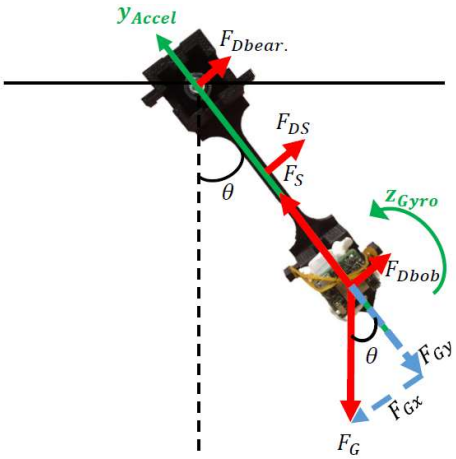

Figure 4.26 - Forces diagram of the pendulum system (not in scale).

The equation of motion of the pendulum can be given by 4.4. [122]

$$\sum \tau = I\alpha \tag{4.4}$$

Where the sum of all the torques (τ) acting on the system in relation to the support point is equal to the product of the variable I (moment of inertia of the pendulum about the support point) with α (angular acceleration of the pendulum about the support point).

Furthermore, it is known that the moment of inertia, I, can be defined as stated in 4.5. [122]

$$I = mL^2 \tag{4.5}$$

Where m is the mass of the bob and L is the total length of the pendulum.

So, taking into account the damped pendulum system above mentioned, its equation of motion is:

$$mL^2\alpha = \tau(F_G) + \tau\left(T_{String}\right) + \tau(F_{Dbear.}) + \tau\left(F_{Dstring}\right) + \tau(F_{Dbob}) \tag{4.6}$$

By definition, the torque of any force F is defined as: [123]

$$\tau(F) = \boldsymbol{F} \times \boldsymbol{r} = Fr\sin\theta \tag{4.7}$$

Where F is the force magnitude, r is the distance between the origin of the force $\boldsymbol{F}$ and the point of rotation and θ is the angle between the vectors $\boldsymbol{F}$ and $\boldsymbol{r}$.

In this way, through equation 4.7, it is possible to define the torque of each one of the forces acting on the system, as presented below:

$$\tau(F_G) = F_G L\sin\theta = mgL\sin\theta \tag{4.8}$$

$$\tau(F_s) = F_s L\sin 0 = 0 \tag{4.9}$$

$$\tau(F_{Dbear.}) = F_{Dbear.} L\sin\frac{\pi}{2} = F_{Dbear.} L \tag{4.10}$$

$$\tau\left(F_{Dstring}\right) = F_{Dstring} L\sin\frac{\pi}{2} = F_{Dstring} L \tag{4.11}$$

$$\tau(F_{Dbob}) = F_{Dbob} L\sin\frac{\pi}{2} = F_{Dbob} L \tag{4.12}$$

Where, g is the gravity constant ($g = 9.81\ m/s^2$).in

It is known that the magnitude of the drag force of a solid object moving in a fluid is proportional to its speed. [122] Moreover, it has been experimentally proved that for small speeds, the magnitude of the drag force is proportional to the first power of its speed. [122] Thus, the drag force of a solid object moving in a fluid at small speeds, F_D, is defined as in 4.13. [122]

$$F_D = Kv \tag{4.13}$$

Being K the damping coefficient.

Due to the complexity of theoretically determining the damping coefficient of a pendulum system, it is often determined experimentally. [122, 124, 125]

Thus, to achieve an estimation of the damping coefficient of this pendulum, explained in 4.7.3, a unique drag force, F_{Dtotal}, acting on the bob was considered. This force is proportional to the angular speed of the bob, $\dot{\theta}$, and it is defined according to equation 4.14.

$$F_{Dtotal} = K_{Total} L \dot{\theta} \tag{4.14}$$

Where K_{Total} is a proportionally constant accounting for the damping coefficient of the bob, of the string and of the bearing. In this way, the torque of the referred damping force would be:

$$\tau(F_{Dtotal}) = K_{Total} L^2 \dot{\theta} \tag{4.15}$$

The total damping coefficient, K_{Total}, was determined experimentally through a developed algorithm in Matlab, explained in 4.7.3.

Hence, before retaking the equation of motion, the forces diagram of the system must be updated to the one presented in Figure 4.27.

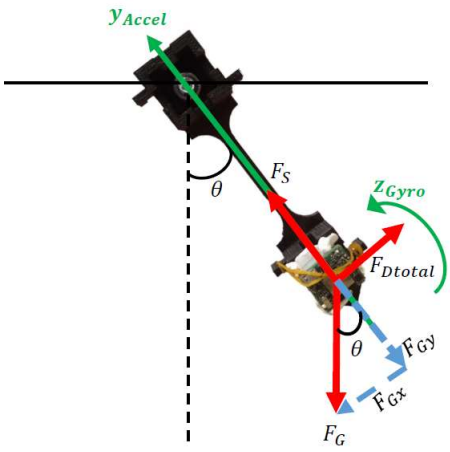

Figure 4.27 - Updated forces diagram for the pendulum (not in scale). Consider positive direction towards the top and to the left.

Now, retaking the equation of motion 4.6 and replacing the torques by its expressions, the angular acceleration of the bob, $\ddot{\theta}$, can be achieved through the following reasoning:

$$mL^2\ddot{\theta} = -mgL\sin\theta + 0 - K_{Total}L^2\dot{\theta} \Leftrightarrow \tag{4.16}$$

$$\Leftrightarrow \ddot{\theta} = -\left(\frac{g}{L}\right)\sin\theta - \frac{K_{Total}}{m}\dot{\theta} \quad \textbf{4.17}$$

Because the system is not an ideal pendulum, having a string with a not negligible mass and being a unique piece, some difficulties emerged when measuring the bob mass. Therefore, the damping coefficient of the system, K', which was determined experimentally in 4.7.3, also accounted for the bob mass, being defined as:

$$K' = \frac{K_{Total}}{m} \quad \textbf{4.18}$$

Thus, the equation of motion of the damped pendulum built in this master thesis is:

$$\ddot{\theta} = -\left(\frac{g}{L}\right)\sin\theta - K'\dot{\theta} \quad \textbf{4.19}$$

To solve this equation, a script on Matlab implementing the Runge-Kutta 4th order method [126], which enabled the edition of the initial conditions of the pendulum movement, i.e. initial angular position and angular velocity, the characteristics of the pendulum (length, mass of the bob and damping coefficient), the duration of the simulation and the sample rate, was used. By introducing these values in the script, the angular position θ and the angular velocity $\dot{\theta}$ of the damped pendulum are obtained in order of time.

Regarding to the angular velocity curve, $\dot{\theta}$, a units conversion from rad/s to dps was performed, thus matching the angular velocity units from the iHandU_v2 device. For comparison, experimental data from the gyroscope z direction, highlighted in Figure 4.27, as z_{Gyro}, was used, since it is the only direction where the angular velocity of the device is changing during the pendulum movement, due to its orientation when placed in the pendulum. On the other hand, the linear acceleration values were calculated from the angular position and velocity data. The y axis linear acceleration of the iHandU_v2 device, represented in Figure 4.27, as y_{Accel}, was used for comparison because it is the direction of the device with higher variation of linear acceleration during the pendulum movement and it is easier to determine analytically.

Along the referred y_{Accel} axis, the net force acting on the pendulum, F_{Ry}, is originated by the difference between the force of the string, F_S , and the gravity force in y, F_{Gy}. The F_S is a force always acting towards the centre of rotation of the pendulum, i.e. a centripetal force, being defined as: [127, 128]

$$F_s = m\frac{v^2}{r} \quad \textbf{4.20}$$

Where, m is the object mass, v is its linear acceleration and r is the movement radius.

With that being said, it can be concluded that:

$$F_{Ry} = F_S - F_{Gy} \quad \textbf{4.21}$$

Thus, the linear acceleration in y, a_y, can be determined as following:

$$ma_y = m\frac{v^2}{L} - (-mg\cos\theta) \Leftrightarrow \quad \textbf{4.22}$$

$$\Leftrightarrow a_y = L\dot{\theta}^2 + g\cos\theta \quad \textbf{4.23}$$

Where, F_{Ry} is the net force acting on the bob in the y axis direction of the accelerometer and a_y is its linear acceleration in y. In addition, the values of linear acceleration in y, a_y, were then converted from m/s^2 to g units. Figure 4.28 represents graphically the y axis gravity acceleration component, the centripetal acceleration component and the total linear acceleration acting on the y axis of the iHandU_v2 device.

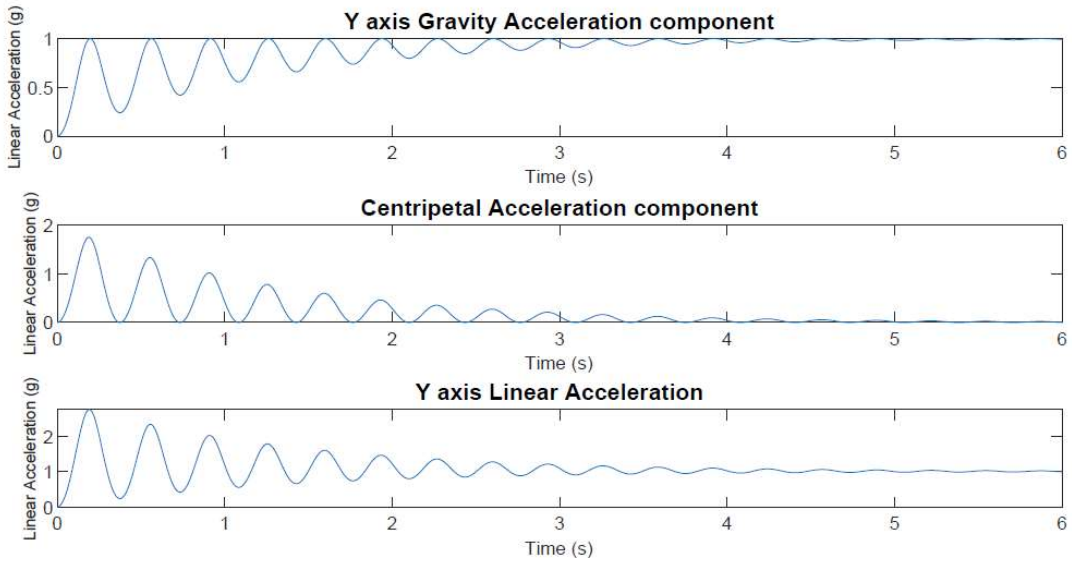

Figure 4.28 - Linear Acceleration in the iHandU_v2 device y axis. First the y axis gravity component, then the centripetal component and finally, the total Linear Acceleration in y.

4.7.3 Damping Coefficient Determination

As mentioned before, this system damping coefficient, K', was estimated experimentally, through an algorithm developed in Matlab.

From what was observed of the aforementioned equations, a typical damped pendulum graph of linear acceleration presents a decreasing amplitude along time. The higher the damping coefficient, the lower is the linear acceleration.

Since the goal of this damping coefficient algorithm is to achieve an estimation of the system damping coefficient, which is a constant of the damped pendulum system, there was no need to apply the algorithm to both linear acceleration and angular velocity curves. In fact, the damping coefficient was determined using only the linear acceleration curves. So, before

describing the developed algorithm, it is important to be aware that in the rest position of the pendulum, the linear acceleration in y is, theoretically one, due to the gravity effect.

Thus, the developed damping coefficient algorithm consists in calculating the difference between the first eleven intersections with one of the experimental and theoretical linear acceleration curves with different damping coefficient values. The damping coefficient giving the lower product between the mean and the standard deviation of the difference between the first eleven intersections with one of the theoretical and experimental curves must be the closest coefficient to the real damping coefficient of the system.

Before developing the algorithm, several theoretical linear acceleration curves computed with random damping coefficients were plotted in Matlab. This allowed to conclude that the theoretical and the experimental linear acceleration curves were more similar in terms of number of oscillations and wavelength when the damping coefficient was in a range of 0.2 to 2. In Figure 4.29 is represented the linear acceleration experimental curve and the theoretical linear acceleration curves achieved with damping coefficients equal to 0.2 and 2.

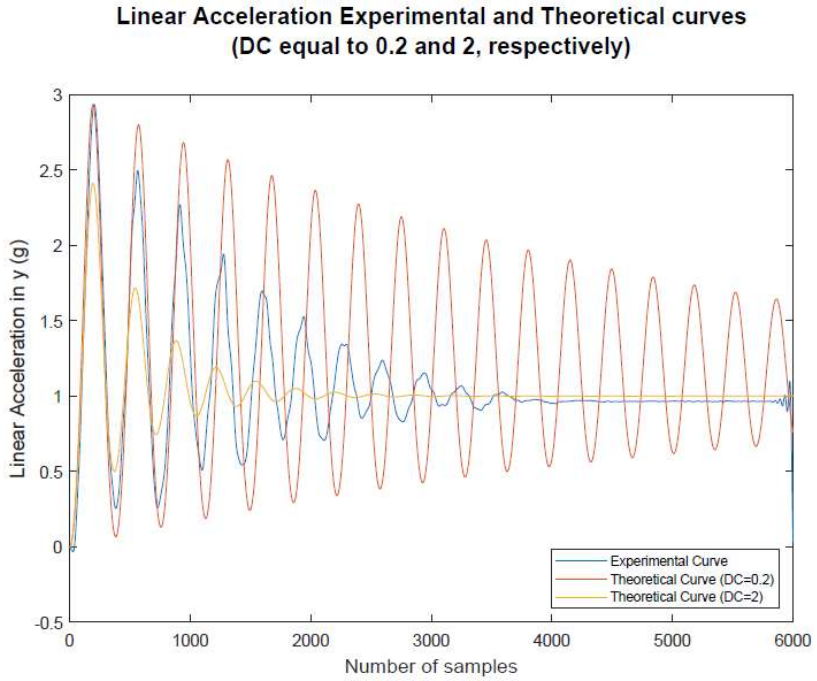

Figure 4.29 - Linear Acceleration in y experimental and theoretical curves with damping coefficients of 0.2 and 2, respectively.

The algorithm contains a *for* loop, where, in each iteration, the damping coefficient changes from 0.2 to 2, in steps of 0.05. A step of 0.05 was chosen after a few initial tests, where it was concluded that coefficients changing less than 0.05 did not originate theoretical linear acceleration curves with significant differences. At each iteration of the loop, the equation 4.19 is solved for the correspondent damping coefficient, and the linear acceleration values are computed according to equation 4.23. Then, the first eleven intersections with one of the theoretical curve are determined. Subsequently, the experimental curve is synchronized with the theoretical one, by

aligning their first peaks. The experimental curve is then up-sampled in order to both experimental and theoretical curves contain the same number of samples, needed for future comparison. At this point, the first eleven intersections with one of the experimental curve are determined. Finally, still in the loop, the difference between the correspondent theoretical and experimental intersections with one is computed and saved for each one of the tested damping coefficients.

For the acceleration curves, which were oscillating in turn of one, the first eleven intersections with one were computed as the mean value of the indexes, in time, of adjacent samples with amplitudes immediately higher and lower than one. The result of the developed function to find the linear acceleration curves intersections with one is visible in Figure 4.30, where it is represented a theoretical linear acceleration curve with damping coefficient equal to 1 and its respective first eleven intersections with one and the experimental linear acceleration curve and its respective first eleven intersections with one.

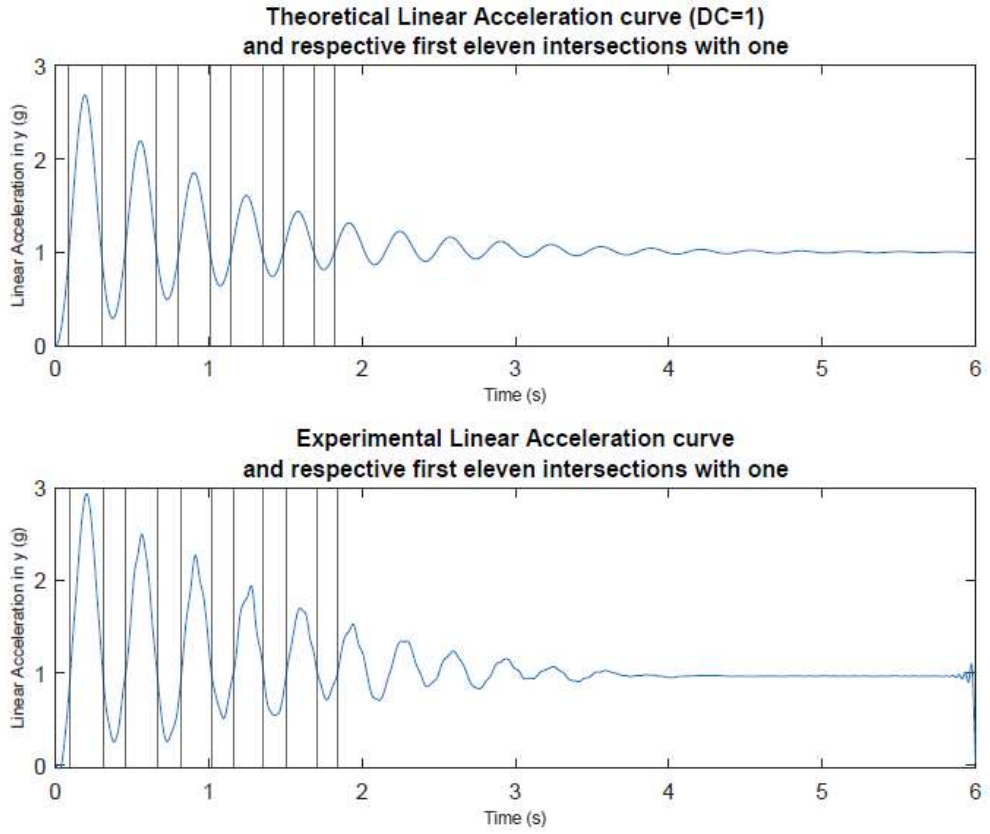

Figure 4.30 - Theoretical (DC=1) and Experimental Linear Acceleration in y curves with their respective first eleven intersections with one.

After the loop, the mean and the standard deviation of the obtained difference of the first eleven intersections with one between the experimental curve and each theoretical curve, obtained with different damping coefficients, were calculated. This allowed to plot error bars (Figure 4.31) relative to the referred differences achieved with different damping coefficients.

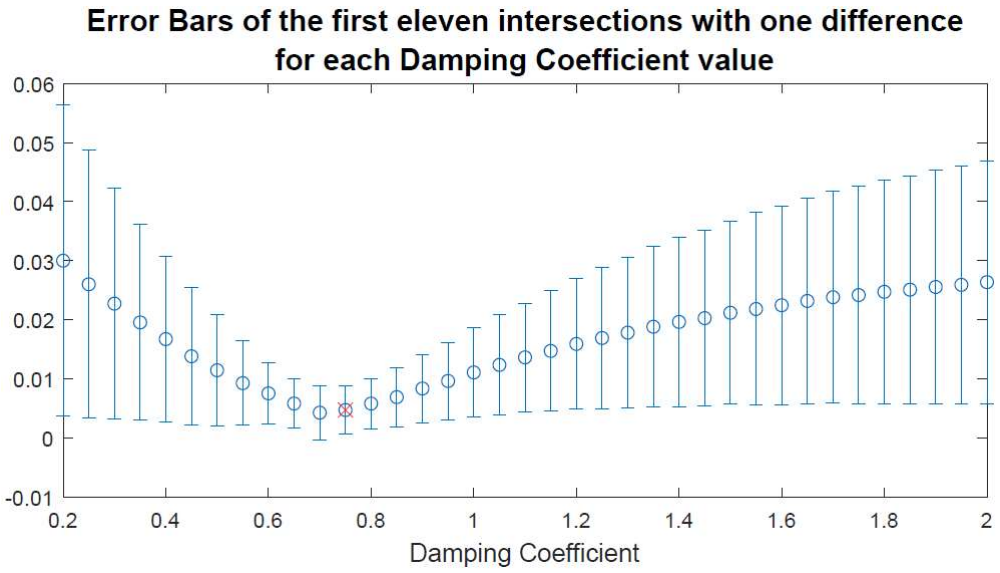

Figure 4.31 - Error bars of the difference between the first ten experimental and theoretical intersections with one.

With the error bars, it is intended to estimate the damping coefficient that balances the minimal mean difference and the minimal standard deviation. However, this damping coefficient was not easy to determine only from observation. Hence, it was chosen the coefficient for each the product between the mean and the standard deviation of the curves intersections with one difference was minimum. In the example shown in the Figure 4.31 the minimum product was achieved with a damping coefficient value of 0.75.

The activity diagram of the Damping Coefficient estimation algorithm is visible bellow (Figure 4.32).

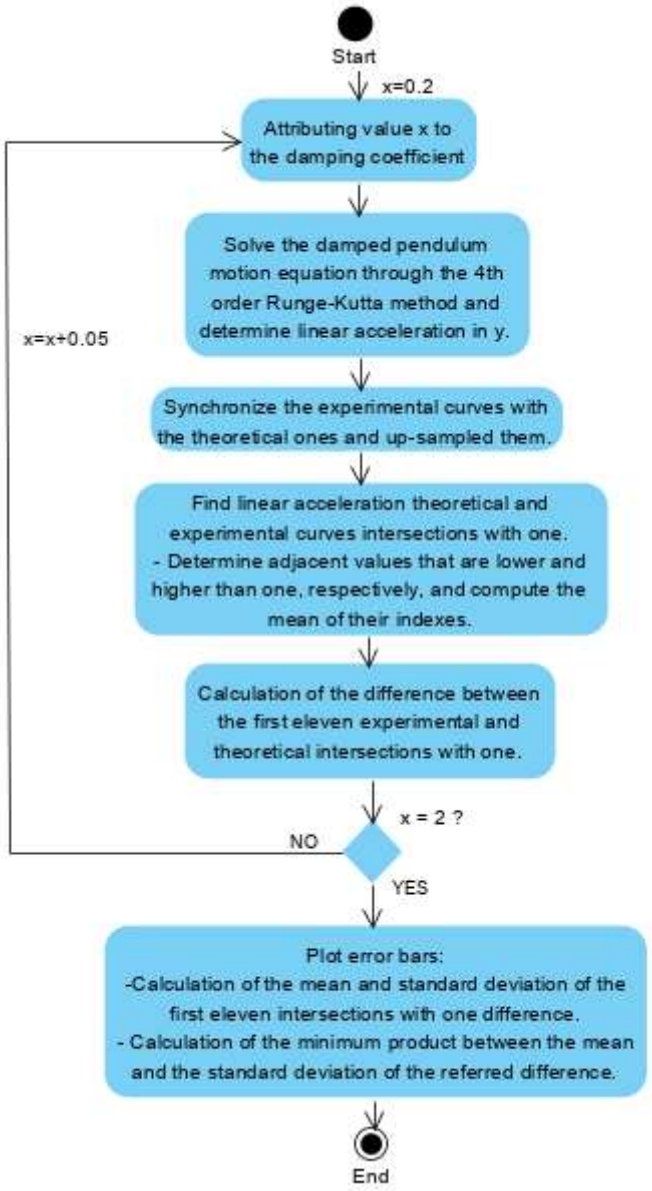

Figure 4.32 - Damping Coefficient Determination algorithm activity diagram.

This algorithm was performed with 100 trials of the same device. For each trial the damping coefficient which corresponds to the minimum product between the intersections with one difference mean and standard deviation was chosen. Then, the damping coefficient of the system was estimated by computing the mean value of the found damping coefficients:

$$Mean\ Damping\ Coefficient = 0.79$$

This value is used to obtain the theoretical linear acceleration and angular velocity curves needed for the reproducibility tests performance, described in 5.4.

5

5 Results and Discussion

As already mentioned, during the development phase of this project, some problems regarding to the hardware have emerged. The description of these errors and their respective resolutions are presented in the first topic of this chapter. After that, in topics 5.2 and 5.3, an analysis of the device power consumption and cost, respectively, is conducted, since it is part of this master thesis objectives to build a low power and low cost device. Subsequently, thanks to the production of two similar iHandU_v2 units, reproducibility tests of the inertial data, provided by their respective inertial sensors, were conducted, and presented in 5.4. In 5.5, the system achieved in this master thesis project is presented.

5.1 Hardware development errors and corrections

During the hardware development several difficulties were faced, that may be related to the lack of experience together with the complexity of the system hardware and the learning of new concepts, technologies and methodologies.

The problems can be divided in three main types: errors in the PCB design, I^2C adaptable voltage translator and voltage divider circuit. While the first type of problems, described in 5.1.1, were detected during the welding of the components, the two last problems were discovered when the communication between the ICM-20948 and the BGM111 was being developed. These two problems were discovered using the same method that consists in reading the WHO_AM_I register of the ICM-20948. To complete this test successfully, the exchange of data between the two components must be as expressed in Table 5.1 and Table 5.2.

WHO_AM_I Test:

Table 5.1 - WHO_AM_I test part 1: Select Bank Register Write Sequence, denominated in Table 5.3.

BGM111	Start	Address + W	Select Bank Reg.	Bank Reg.	Stop
ICM-20948		ACK	ACK	ACK	

Table 5.2 - WHO_AM_I test part 2: WHO_AM_I reset value Read Sequence, denominated in Table 5.3.

BGM111	Start	Address + W		WHO_AM_I Reg.		Start	Address + R			NACK	Stop
ICM-20948			ACK		ACK			ACK	WHO_AM_I Reset Value		

Table 5.3 - Hexadecimal values of the WHO_AM_I test bytes.

Address	0x68
Write bit (W)	0
Read bit (R)	1
Address + W	0xD0
Address + R	0xD1
Select Bank Reg.	0x7F
Bank Reg.	0x00
WHO_AM_I Reg.	0x00
WHO_AM_I Reset Value	0xEA

The use of these registers allowed to understand the two problems that existed in the digital communication, which are explained in 5.1.2 and 5.1.3.

5.1.1 Errors in PCB Design

During the welding of the components some missing connections were verified:

- The ground and the pad 2 of the battery.
- The ground and the pad 9 of the ICM-20948.
- The led D1 and the resistor R2.
- The resistor R2 and the capacitor C2.

These missing connections were easily solved with wrapping wire.

In addition, a capacitor connected to pin 5 of the voltage regulator was also missing, problem that was also solved with wrapping wire.

Finally it was put VCCIO voltage on pin 7 of the BGM111 instead of VCC Analog. As referred in a 4.3.1.4, VCC Analog was supposed to be the reference voltage for the analog force sensors connected on pin 5 and 6 of the BGM111. Due to this mistake, it was used VCC as reference, assuming the disadvantage of the possibility of existing noise.

These problems were already rectified in Altium Designer and the design of the corrected PCB is ready for future orders without these issues.

5.1.2 Voltage Translator

After solving the above mentioned errors, the connection between the ICM-20948 and the BGM111 was tested through the aforementioned WHO_AM_I test.

To see the exchange of data between these two components, the Seleae Logic software was firstly used. To work with this software, an adaptor with eight wires was needed. One of the wires must be connected to the ground of the board while the remainder seven can be connected to any point in the board, which the user intends to analyse. The adaptor is then connected to the computer through an USB cable. In this case, two wires were used to connect to the I^2C lines (SCL' and SDA') between the voltage translator and the BGM111, as represented in Figure 5.1.

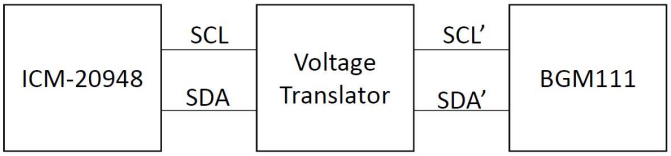

Figure 5.1 - I^2C lines schema as implemented in the iHandU_v2 device.

The Seleae Logic software displays the signals logical values and the corresponding hexadecimal numbers of each transferred byte. Using this software, it was realized that the connection with the ICM-20948 was not being obtained, since the inertial sensor was not acknowledging its address. The disadvantage of this software is that it not displays the signals with their real levels of voltage, but only with the high or low level. So, to debug the problem, the same I^2C communication lines were observed in the oscilloscope, as well as the SDA signal between the ICM-20948 and the voltage translator.

As referred in previous chapters, the voltage translator implemented on the system was the LSF204. However, this component was not the first option. Initially it was ordered and implemented in the hardware the TXB0104 voltage translator, since it had been already used in the lab, but for SPI communications, working perfectly with the BGM111. Hence, the signals in Figure 5.2 were acquired when the TXB0104 was implemented as voltage translator.

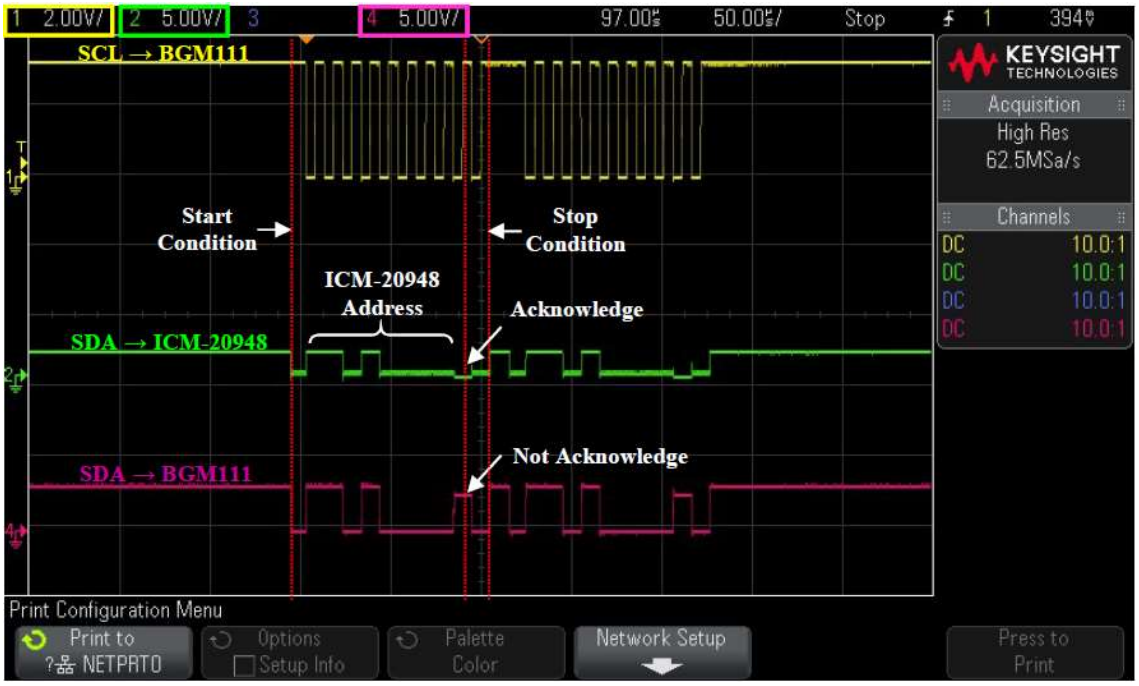

Figure 5.2 - I²C communication signals (TXB0104 implemented in the hardware). SCL (BGM111) in the first trace; SDA (ICM-20948) in the second trace; SDA' (BGM111) in the third trace.

The first trace is the clock signal measured in the clock (SCL) I²C line on the side of the BGM111. The second trace is the SDA signal measured on the side of the inertial sensor. Finally, the third trace, represents the SDA signal measured on the side of the BGM111.

From Figure 5.2 is possible to conclude that the ICM-20948 was actually acknowledging its address. Though, the low level signal was not passing to the BGM111 side. This means that the TXB0104 was not being able to maintain the signal low, when converting it to the BGM111.

It was not well understood why this happened. However, when this problem appeared, the TXB0104 datasheet was reviewed and, there, it was written that this component must not be used for I²C applications.

The solution for this problem consisted in finding another voltage translator, compatible with the needed requirements for the device and suitable for I²C communication. Furthermore, it was preferred that this voltage translator had the exactly same footprint as the first one, to allow its direct replacement on the PCB. The LSF204 was the only component found checking all these requirements and it was, therefore, implemented with success.

5.1.3 Voltage Divider circuit

Having changed the voltage translator, it was expected to obtain success when performed the WHO_AM_I test. However, the result was not the expected. The acknowledgment on the BGM111 side was being received in a first communication attempt very often. When this situation occurred, it was possible to see some of the following registers of the WHO_AM_I test, but never

until the end. At a certain point, the BGM111 received a not acknowledgement (NACK) and the communication ended abruptly.

Once again, the I²C communication lines were observed in the oscilloscope to check the voltages of the I²C lines. The following signals in Figure 5.3 match with the ones before mentioned.

Figure 5.3 - I²C communication signals (LSF204 implemented in the hardware). SCL (ICM-20948) in first trace; SDA (ICM-20948) in second trace; SDA (BGM111) in third trace.

First thing to highlight in Figure 5.3 is that the SDA signal on the ICM-20948 and on the BGM111 (second and third traces, respectively) have now the same properties, differing only in the voltage level, as is supposed to. This is the proof that the LSF204 is fitting well for the purpose of the system device.

Though, what also stands out in the image is the decreasing voltage level of the clock signal, in yellow. This signal is being measured on the clock I²C line on the side of the ICM-20948 and, therefore, should have a voltage level equal to VCCIO. With that being said, it can be concluded that VCCIO is decreasing during the exchange of data. To be sure of this statement, the fourth channel of the oscilloscope (third trace) was changed to display the VCCIO level in its source (Figure 5.4).

Figure 5.4 - I²C communication signals: SCL (ICM-20948) in yellow; SDA (ICM-20948) in green; VCCIO (source) in pink.

Through the above figure, it can be confirmed the decreasing of VCCIO during data transference.

In the datasheet of the ICM-20948 is written that an input voltage is considered low when in a range of -0.5 to 0.3*VCCIO, in volts. So, as VCCIO is decreasing, also is the maximum voltage to the signal be considered as low level. Moreover, in the SDA signals, first and second traces, is visible that the acknowledgement is occurring at an increasingly voltage. Furthermore, at the instant of 9th clock pulse of 4th byte transference, the SDA signal is higher than 0.3*VCCIO. Hence, the signal is interpreted as a not acknowledgement and the communication ends.

It should be recalled that ICM-20948 only accepts a VCCIO supply voltage in a range between 1.71V to 1.95V. So, when VCCIO decreases for values lower than 1.71V, the ICM-20948 stops communicating.

As mentioned in 4.2.5, VCCIO was created through a voltage divider circuit and not through the TPS71518 DCKR voltage regulator, as it is suggested to implement in a future device. The voltage divider circuit started to be designed, with two resistors of Ra = 100kΩ and Rb = 120kΩ and a voltage source equal to VCC (3.3V). Connecting Ra to VCC and Rb to the ground, it was obtained a VCCIO = 1.8V between the resistors. Such higher values of resistors were selected to limit the leaked current. But, in this case it seemed that the resistors were limiting too much the current and the reminder current was not even enough to perform the WHO_AM_I test with success.

Being aware of this situation, the resistor values were decreased. Several attempts were made with different resistors of decreasing values. After a few attempts, the WHO_AM_I test was finally successfully performed with resistor of Ra = 15Ω and Rb = 22Ω, as shown in Figure 5.5. Despite being not visualized in the oscilloscope the last three bits of the WHO_AM_I Reset value (010) and the NACK and Stop conditions, the WHO_AM_I reset value was seen in the Seleae software and received on the phone through Bluetooth.

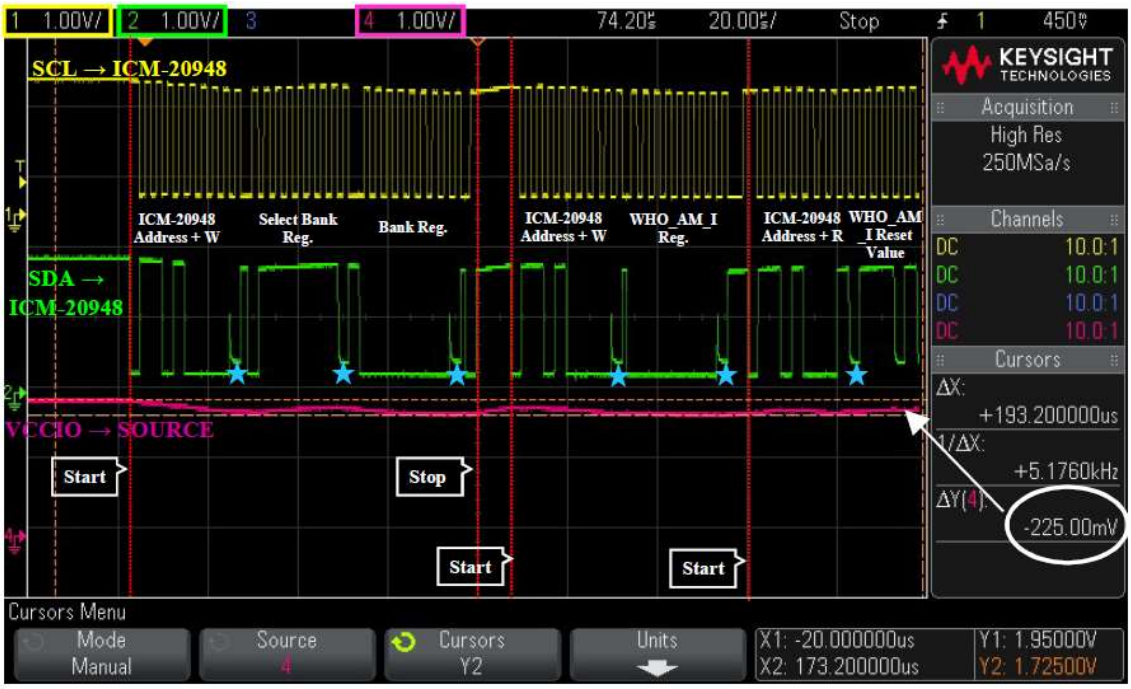

Figure 5.5 - I²C communication signals (Successful WHO_AM_I test). SCL (ICM-20948) in first trace; SDA (ICM-20948) in second trace; VCCIO (source) in third trace.

5.2 Analysis of wearable device power consumption

The Simplicity Studio software contains a useful tool, named Energy Profiler, to analyse the power consumption of a Silicone Labs device. This tool allow to see the current consumption in real time of a device connected to the software through the Blue Gecko Evaluation board, presented in 4.4. Furthermore it calculates the mean current consumed of the total signal recorded until the measurement instant and/or of a selected part of the signal. The Energy Profiler tool was one of the main reasons why Silicone Labs device was chosen to develop the firmware of the iHandU_v2 hardware.

As previously mentioned, the battery of the device was not implemented during the development of the firmware. In fact, the battery was integrated in the device only after finishing the firmware code and ensuring that the device was correctly programmed. At this time, the current consumption of the iHandU_v2 device was tested in the Simplicity Studio through the

Energy Profiler tool. Unfortunately, this tool presented saturated current consumption values for the developed iHandU_v2 device. To debug the problem, voltage values in different points of the board were measured with a multimeter. It was seen that the voltage provided by the TPS71533 DCKR, described in 4.2.5, was lower than the 3.3V needed to feed the remainder components. The reason must be the existence of a leakage of current in the implemented voltage divider circuit, described in 5.1.3. It is once again recalled that despite being presented a voltage regulator to create the VCCIO voltage supply in 4.2.5, this component was not implemented in the developed device. Instead, it was implemented a voltage divider circuit with very low resistors to create the VCCIO voltage (this is better explained in 5.1.3). Because the resistors are of very low values (15Ω and 22Ω), the current that is transferred by them may be more than the available one. Therefore the available current was being consumed too fast and the voltage regulator could not provide the 3.3V.

To overcome these circumstances and to execute a fair analysis of the device power consumption, the developed firmware was loaded in the BGM111 included in the Blue Gecko Module Wireless Starter Kit, mentioned in 4.4. In the notification, random float values instead of the values read by the sensors were sent. Thereby, it was possible to use the Energy Profiler to analyse the current consumption of the BGM111, which theoretically is one of the most current consumer components and, together with the ICM-20948, is the only one for which the current consumption changes during the device operation, as explained below. For the current consumption values of the remainder components, which are constant during the device operation, the values presented in their respective datasheets were used. These values were added to the ones resulting from the study of the BGM111 current consumption through the Energy Profiler.

When the device is on, the BGM111 can be in three modes:

- Discovering mode: The Bluetooth Module of the BGM111 is advertising while no other device is connected to it → 914.02 μA. (Figure 5.6)
- Connected mode: An external device is connected to the BGM111 → 711.15 μA (Figure 5.8)
- Transmitting mode: The BGM111 is sending data via Bluetooth to an external device → 1.34 mA. (Figure 5.9)

In each one of these modes, the current consumption is different but approximately constant.

The following figures present a part of the current consumption signal over time in the three different BGM111 modes. For a more reliable comparison, the mean values of current consumption in 10 seconds of each signal were selected.

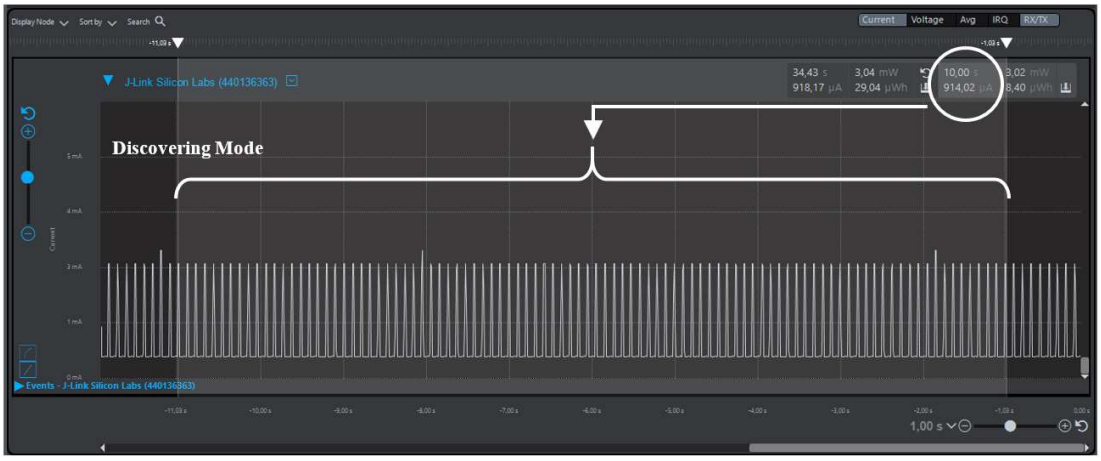

Figure 5.6 - BGM111 current consumption over time in Discovering Mode (914.02 µA).

Before presenting the current consumption signal of the BGM111 in Connected mode, is displayed in Figure 5.7 the part of the signal corresponding to the transition from the discovering mode to the connected mode. The peak of current, typical from this transition, is so fast that does not affect the overall current consumption of the device.

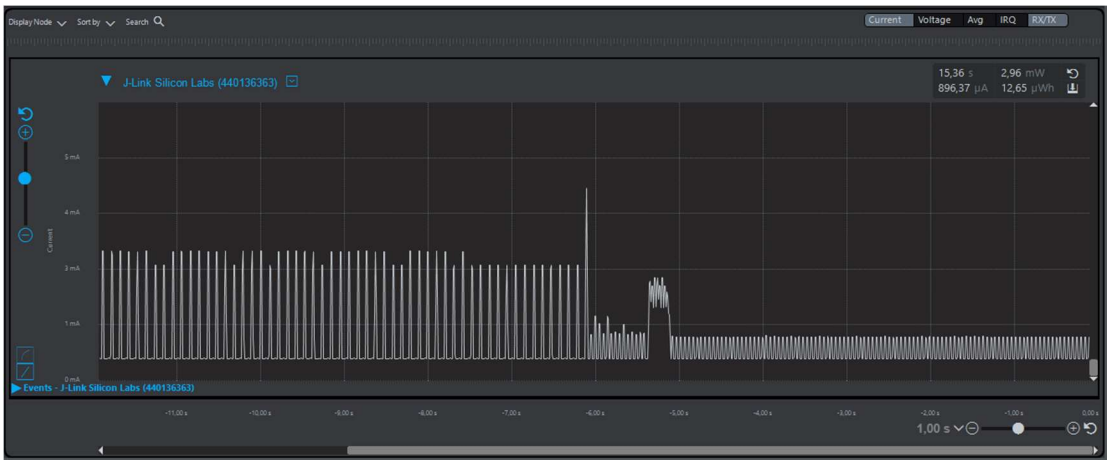

Figure 5.7 - BGM111 Current Consumption when in Transition.

Figure 5.8 corresponds to the current consumption signal when BGM111 is in connected mode.

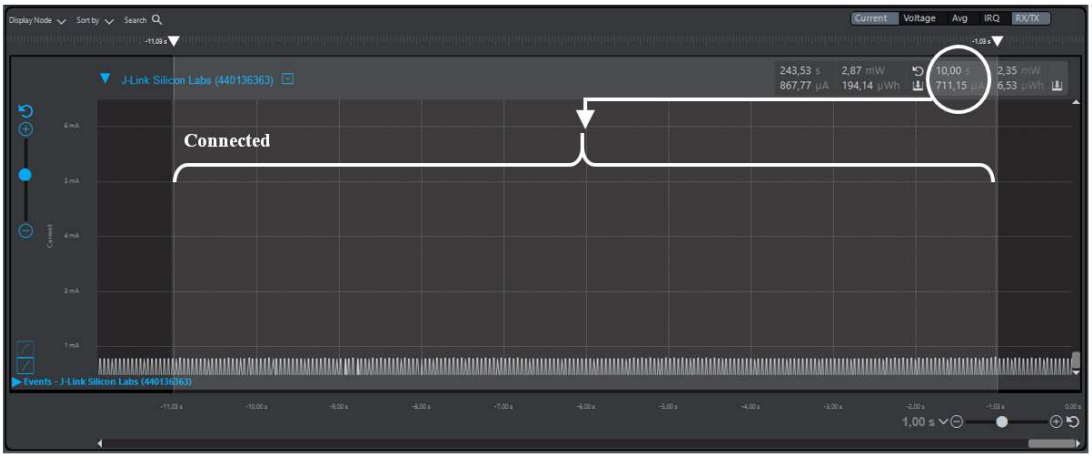

Figure 5.8 - BGM111 current consumption over time in Connected Mode (711.15 µA).

Table 5.4 displays the mean current consumption in 10 seconds during the Discovering and the Connected modes.

Table 5.4 - BGM111 10 seconds mean current consumption.

BGM11	
Mode	Mean current consumption in 10 seconds (µA)
Discovering mode	914.02
Connected mode	711.15

The current consumption in transmitting mode depends on the quantity of data, i.e. number of bytes, sent in one notification. In the case of this project, it was decided to send data from all the sensors in the same notification. This decision was made because the applications used to read from the Bluetooth didn't allowed to read data from two different services or characteristics at the same time. Recently, some members of the BRAIN group managed in implement this functionality. Therefore, power consumptions tests can be remade in the future without this limitation.

In this way, a study of the current consumption in dependence on the number of bytes sent in one notification was performed. The device contains 5 sensors: one accelerometer, one gyroscope, one magnetometer and two force sensors, which sensors reading frequency is of 50 Hz. As mentioned before, a unique reading of these 5 sensors give a total of 11 float numbers, which in bytes corresponds to 44 bytes. In conclusion, 44 bytes would be the minimum number of bytes sent in one notification. Additionally, it is important to refer that the GATT profile in Simplicity Studio sets a maximum number of possible bytes to send in one notification of 255.

Having this into account, it was measured the mean current consumption of the BGM111 in 10 seconds, when it was sent from 1 to 5 samples of each sensors in one notification, i.e. from 44 to 220 bytes. The measured values are visible in Table 5.5.

Table 5.5 - BGM111 10 seconds mean current consumption in Transmitting Mode depending on the number of samples per sensor sent.

BGM111 - Transmitting Mode			
Samples/ sensor	Number of bytes in one notification	Sending rate (Hz) (2200bytes/sec)	Mean current in 10 sec while transmitting (mA)
1	44	50.00	1.56
2	88	25.00	1.37
3	132	16.67	1.35
4	176	12.50	1.36
5	220	10.00	1.34

According to Table 5.5, the lowest current consumption is obtained when 5 samples per sensor are sent, corresponding to a total of 220 bytes per notification. Thus, this was the strategy implemented in the firmware of the device, obtaining a data sending frequency of 10 Hz. Figure 5.9 presents the current consumption signal over time in the transmitting mode of BGM111.

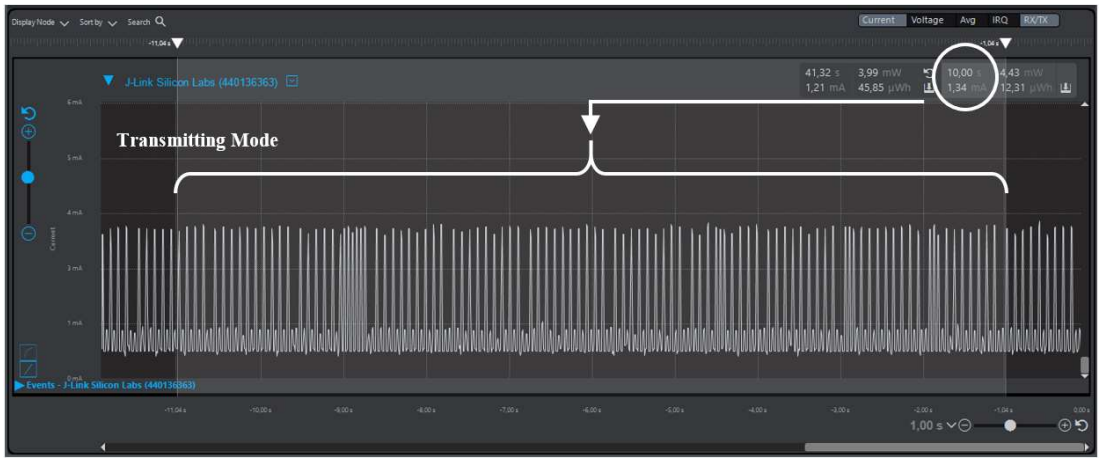

Figure 5.9 - BGM111 current consumption over time in Transmitting Mode (1.34 mA).

At this point, it was made a study of a typical DBS surgery routine at Hospital S. João. It is important to be aware of not only how long the BGM111 is in discovering, connected or transmitting modes as also how long the ICM-20948 is in sleep or 9-axis mode, since these are the two main components for which the current consumption changes while the device is operating. For this reason, Table 5.6 presents the theoretical current consumptions in sleep and 9-axis mode of the ICM-20948.

Table 5.6 - ICM-20948 current consumption.

ICM-20948		
Mode	**Theoretical current consumption (µA)**	**Time per surgery (min)**
Full-Chip Sleep Mode	8	210
9-Axis Mode	3110	30

A DBS surgery has a duration of about 4 hours. In this analysis, it was considered that the device is turned on in the beginning of the surgery and it is just turned off at the end. Furthermore, it was also considered that, during the surgery, ten wrist rigidity changes assessment sessions of three minutes each are made, being that the device would be in transmitting mode only during these sessions.

In order to estimate the duration of the iHandU_v2 device battery, it were considered the current consumptions of the iHandU_v2 device components during one hour of surgery, where will occur three wrist rigidity changes assessment sessions of three minutes each. Therefore, the BGM111 is in transmitting mode during 9 minutes, in discovering mode during 1 minute and in connected mode in the remainder 50 minutes. Table 5.7 presents the BGM111 and the ICM-20948 current consumptions during these periods in their different modes. The current consumption values were calculated by multiplying the time, in hours, they are in each mode, by the mean current consumption values of each mode presented in Table 5.5 and Table 5.6.

Table 5.7 - Surgery actions and respective BGM111 current consumptions in one hour of DBS surgery.

One hour of surgery						
Actions	**BGM111 Mode**	**ICM-20948 Mode**	**Time (hours)**	**Time (min)**	**BGM111 Current Consumption (mA)**	**ICM20948 Current Consumption (mA)**
Time between turn on the device and connect it	Discovering	-	0.02	1	0.0183	-
Waiting time	Connected	Full-Chip Sleep Mode	0.83	50	0.5903	0.0066
Total time of evaluation sessions	Transmitting	9-axis (DMP disabled)	0.15	9	0.2010	0.4665
Total component current consumption in one surgery (mA):					0.8095	0.4731

Finally, the current consumption of the device was estimated by summing up the achieved values of BGM111 and ICM-20948 current consumptions in one hour (Table 5.8) with the current consumption values of the remainder components, which were found on their respective datasheets.

Table 5.8 – Device Power Consumption in one hour of DBS surgery.

Device Power Consumption in one hour of a DBS surgery	
Component	**Current Consumption during one hour (mA)**
ICM-20948	0.4731
Force Sensors	1.0000
Voltage Translator	0.0037
Voltage Regulator 3.3V	0.0032
Voltage Regulator 1.8V	0.0032
BGM111	0.8095
Total device current consumption in one hour (mA):	2.2927

To conclude, the battery life of the device when it is used in surgery can now be calculated. Considering that the battery affords not 100% but 95% of its capacity, the available current is the one determined in 5.1.

$$Available\ current = 0.95 * 85mAh = 80.75mAh \quad \textbf{5.1}$$

Thus, an estimation of the battery duration can be concluded dividing its available current hour, in mAh, by the estimated device current consumption in one hour, in mA (5.2).

$$Battery\ life = \frac{80.75\ mAh}{2.29\ mA} \approx 35.26\ hours\ (9\ surgeries) \quad \textbf{5.2}$$

5.3 Analysis of device final cost

It is believed that the iHandU_v2 system has a huge potential to be commercialized, existing already this intention among the BRAIN members. Therefore, when projecting the iHandU_v2 device, an effort was made to minimize the total cost of the product as much as possible. This will allow a competitive position for the product in the market.

Having this into account, a cost analysis of the system hardware developed during this master thesis was made. Physically, the hardware comprises the PCB, the welded components and the textile band. Thus, in this topic, the needed quantities and respective unitary prices of each element of the system hardware are discriminated in Table 5.9.

. In particular, the 5th column, presents the unitary price for each element when bought in small quantities (lower than 10), since this was the case of this master thesis project. However, in a near future, it is intended to perform a mass production of the system, therefore, the 6th column already has an analysis of the elements unitary price when purchased in quantities of 100 units.

Table 5.9 - iHandU_v2 system cost analysis.

IHandU_v2 System Cost					
Element	**Description**	**Value**	**Quantity**	**Unitary price for produce 1 system (€)**	**Unitary price for produce 100 systems (€)**
Textile band	-	-	1	30.70[1]	11.13[2]
PCB	-	-	1	15.08	1.32
Battery	RJD2032C1	-	1	9.20	5.66
Battery Holder	3003	-	1	0.68	0.38
Battery Charger	MCP73831T-2ATI/OT	-	1	0.50	0.38
USB Connector	629105150921	-	1	1.80	1.38
Button	CUS 12-TB	-	1	1.09	0.61
Programmer	FTSH-105-01-F-D-K	-	1	2.52	1.65
MCU Bluetooth Integrated Module	BGM111	-	1	8.79	6.58
3.3V Voltage Regulator	TPS71533DCKR	-	1	0.76	0.50
1.8V Voltage Regulator	TPS71518DCKR	-	1	0.76	0.50
IMU Sensor	ICM-20948	-	1	6.19	3.30
Force Sensors	FSR Series 400	-	2	6.86	3.93
Voltage Translator	LSF0204DRUTR	-	1	1.14	0.74
Capacitors	GRM152C80G104ME19D	0,1 µF	6	0.11	0.05
	GRM152D80G474ME15D	0,47 µF	1	0.25	0.09
Resistors	CRCW0603100RFKEAC	100 Ω	2	0.09	0.01
	CRCW0100330RFREL	330 Ω	2	0.25	0.05
	CRCW04024K70FKEDC	4,7 kΩ	2	0.09	0.01

[1] (D. Dias 2019, personal communication, July)
[2] (D. Dias 2019, personal communication, July)

	CRCW04021 0K0FKEDC	10 kΩ	2	0.11	0.03
	CRCW04022 4K0FKEDC	24 kΩ	1	0.09	0.01
LEDS	SM0402BW C	Blue	1	0.56	0.32
	SM0402RC	Red	1	0.52	0.30
Inductor	BLM21PG22 0SN1D	-	1	0.10	0.04
Total Cost of each iHandU_v2 System Hardware:				88.24	39.97

According to Table 5.9 analysis, the system hardware cost developed during this master thesis, makes a total of 88.24€. However, when the production is made in large quantities, this cost has a reduction of about 55%, making a total of 39.97€. By analysing this result, it can be concluded that it is being faced an Economy of scale, i.e. there is a cost advantage in relation to the increase of production. [129] With that being said, when planning on commercializing the iHandU_v2 system, an economy of scale can be a competitive advantage in the market, making the system even more attractive in comparison to other commercialized medical systems.

5.4 Device Reproducibility & Calibration Accuracy Tests

To ensure the reproducibility and reliability of the accelerometer and gyroscope data provided by similar sensors implemented in different devices, two developed units of the iHandU_v2 device were tested. The devices were submitted to the movement of the damped pendulum presented in 4.7.1. Thanks to the developed Web Application, mentioned in 4.6, which allows for sensors data download, the experimental curves of y axis linear acceleration and z direction angular velocity of both iHandU_v2 units inertial sensors were obtained in Matlab. These curves were compared with the theoretical ones obtained in 4.7.2. Despite being expected a high approximation of the theoretical and experimental curves, it is of utmost importance that the comparison factors between the experimental curves of each device and the theoretical curves be very similar, thus ensuring the reproducibility of the devices.

A detailed explanation on how the theoretical and the experimental curves were compared to each other, as well as the achieved conclusion, are provided in the following topic.

5.4.1 Reproducibility tests

After estimating the system damping coefficient in 4.7.3, the experimental and the theoretical data of both, y axis linear acceleration and z direction angular velocity, can finally be compared. So, first, the theoretical data must be obtained. For this purpose, the movement initial

conditions, the characteristics of the pendulum and the simulation conditions must be set as explicit in Table 5.10.

Table 5.10 - Constants of the damped pendulum initial conditions, simulation conditions and characteristics.

Pendulum Conditions	
Length of the Pendulum	$\mathrm{L} = 0.105\ \mathrm{m}$
Damping Coefficient	$\mathrm{K}' = 0.79$
Initial angular position	$\theta_0 = \frac{\pi}{2}\ \mathrm{rad}$
Initial angular velocity	$\dot{\theta}_0 = 0\ \mathrm{rad/s}$
Duration of the simulation	$\Delta\mathrm{t} = 6\ \mathrm{s}$
Sample rate	$\mathrm{S} = 1000\ \mathrm{sample/s}$

The duration of the simulation was set according to the time pendulum takes to stop when under the initial conditions of angular position and velocity mentioned in Table 5.10. Regarding the sample rate for the theoretical data, several values were tested, starting from $50\ sample/s$, which is the sample rate at which the experimental values are being obtained, until increasingly higher values. A sample rate of $1000\ sample/s$ was chosen because it enabled the achievement of more accurate results in the data processing methods referred in 4.7.3.

After setting these constants, the motion equation of the pendulum, equation 4.19, is solved through the already mentioned script in Matlab implementing the Runge-Kutta 4th order method [126] and it is obtained the linear acceleration values, equation 4.23, in g, and the angular velocity values in dps, in y and z directions, respectively. The experimental curves of the two developed iHandU units were obtained thanks to the developed Web Application, presented in 4.6, that enabled their recording during the pendulum movement.

In order to compare the experimental linear acceleration and angular velocity data of the two iHandU units, fifty trials for each device were made. For each trial, two factors were computed to compare the experimental and the theoretical curves:

1) Mean Oscillation error: This error consists in the percentage difference between the first eleven intersections with one, for the experimental and theoretical linear acceleration curves, or with zero, for the experimental and theoretical angular velocity curves. To achieve the error, the algorithm starts by synchronizing the experimental curves with the respective theoretical ones, by aligning their first peaks, and up-sampling them so that they have the same number of samples as the theoretical ones. Then, the intersections of the experimental and theoretical curves are determined, using the method referred in 4.7.3.

Having determined the curves intersections, the oscillation error between the correspondent experimental and theoretical curves is finally calculated. To compute this error, the array of the difference between the first eleven intersections of the respective experimental and theoretical curves is found. Then, a moving average is applied to each three elements of the referred array and each average value is divided by the difference between the respective third and the first intersection of the experimental curves, i.e. the period of the experimental oscillations. Then the mean value of the obtained array is calculated, thus corresponding to the oscillation error of the tested curves.

2) Amplitude Correlation Coefficient: This is a coefficient that, when multiplied by the experimental curves amplitudes, causes their best approximation to the respective theoretical ones. To calculate this coefficient the sqrError function, [130] which computes the amplitudes difference between two curves, sample by sample, and the respective coefficients to approximate them, was applied to the y axis linear acceleration and z direction angular velocity experimental and theoretical curves. Then the fminsearch function, available on Matlab, was used to find the coefficients for which the sqrError function is minimum, thus minimizing the amplitudes difference between the experimental and the theoretical curves.

The activity diagram of the developed algorithm to obtain the two comparative factors of each trial performed with the two iHandU units is visible in Figure 5.10.

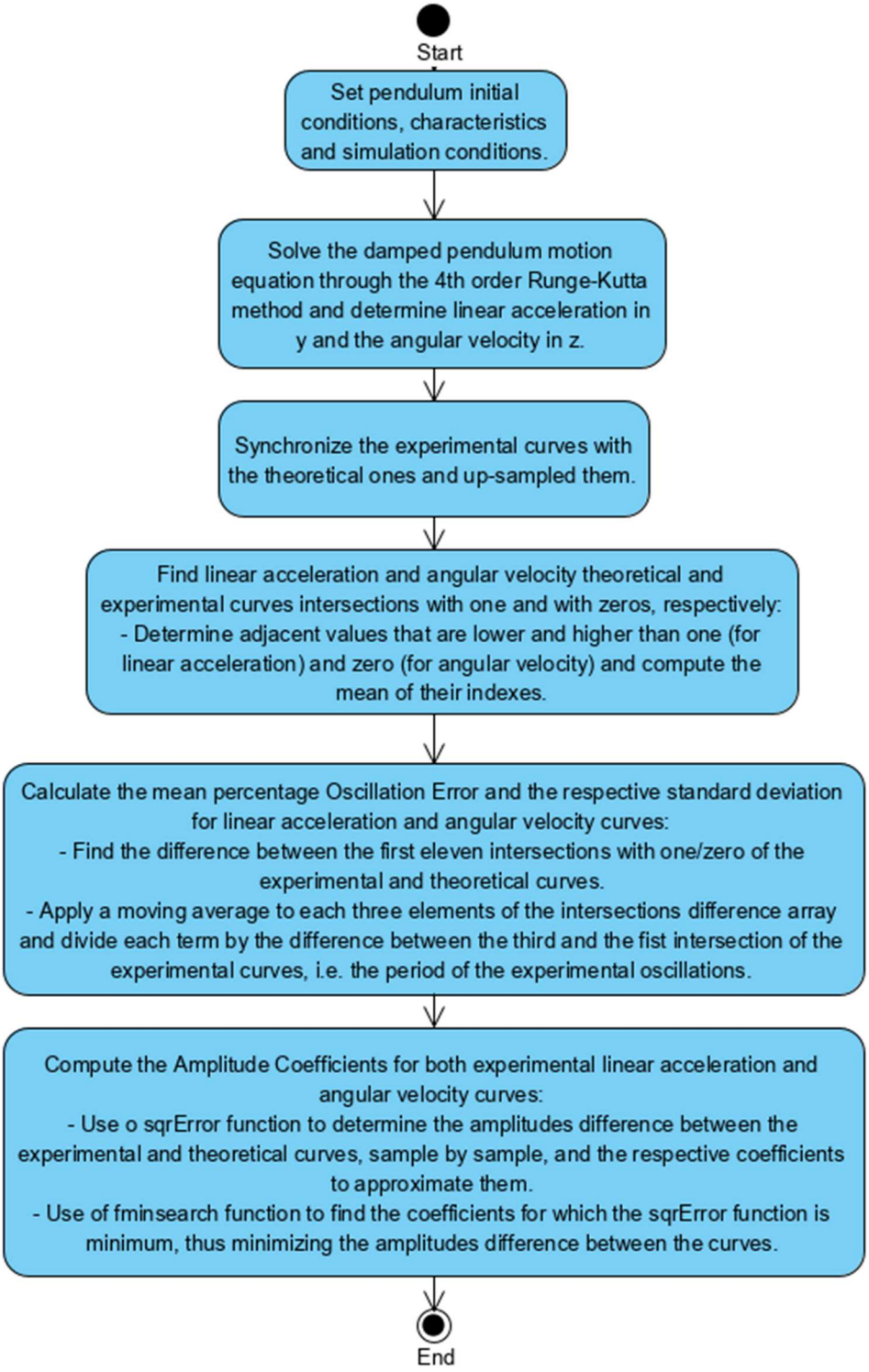

Figure 5.10 - Activity Diagram of Curves Comparison Algorithm.

To prove the reproducibility between the devices, a high similarity of the aforementioned two factors when they are measured with the two developed iHandU_v2 units is expected, i.e. mean oscillation errors below 5% and amplitude correlation coefficients around 1±0.05. Therefore, the described algorithm was applied to the accelerometer and gyroscope data provided

by the sensors of the two iHandU_v2 units produced during this master thesis. The mean results obtained with fifty trials for each produced device are explicit in Table 5.11. Furthermore, Figure 5.11 presents the theoretical and one of the experimental curves of y axis linear acceleration and z direction angular velocity, obtained with both devices.

Table 5.11 - Comparative factors between y axis Linear Acceleration and z direction Angular Velocity fifty experimental curves and their respective theoretical curves of different devices.

Curves	Device	Mean Oscillation Error ± Standard deviation (n=50)	Mean Amplitude Correlation Coefficient ± Standard deviation (n=50)
Linear Acceleration	D1	2.71 % ± 1,27 %	0.98 ± 0.02
	D2	3.79 % ± 1.99 %	1.05 ± 0.01
Angular Velocity	D1	1.43 % ± 0.79 %	0.95 ± 0.03
	D2	1.56 % ± 0.77 %	0.95± 0.02

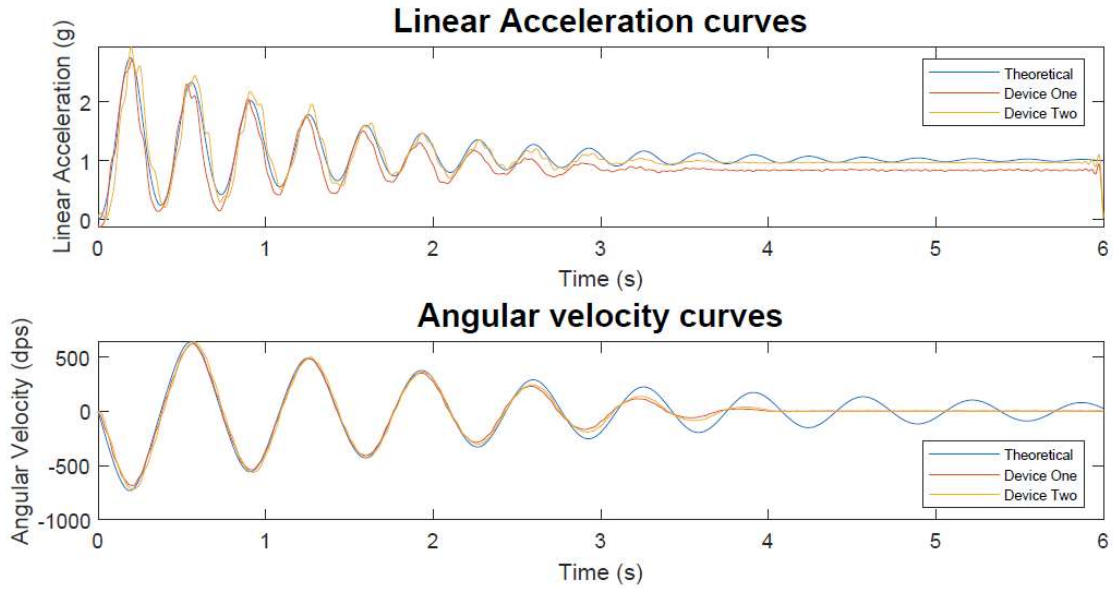

Figure 5.11 - Linear Acceleration and Angular Velocity Experimental and Theoretical curves.

By observing the linear accelerations curves in Figure 5.11, it can be concluded that, in this trial, the experimental linear acceleration curve from the device 2 is very close to the theoretical one. However, focusing on the linear acceleration trial obtained with the device 1 a slightly disparity between the amplitudes of the theoretical and experimental curves is seen. This disparity occurred because the device was not correctly positioned in the pendulum. In fact, the incorrect position of the device is proven in Figure 5.11 where it is visible that the experimental linear acceleration of the device 1 tends to a value lower than one, instead of tending to one, as it was supposed to.

Regarding to the Table 5.11 results, a mean oscillation error in the 3% was obtained for the linear acceleration curves of both devices, meaning that the timings at which the experimental

oscillations are occurring are very similar to the theoretical oscillation timings. Regarding the amplitudes, an amplitude correlation coefficient of practically one for both devices reveals the high amplitude correlation of the theoretical and experimental curves.

Furthermore, it is important to highlight the similarity between the linear acceleration data provided by the devices 1 and 2. The fact they present similar comparison factors of oscillation timings and amplitudes in relation to the same theoretical curve proves the reproducibility of the two iHandU units linear acceleration data.

Regarding to angular velocity data, a mean oscillation error in the 1% and amplitude correlation coefficients close to one for both devices demonstrate the high approximation of the experimental curves of both devices in relation to the theoretical ones. Therefore, since the two comparative factors are similar for both devices, also the reproducibility of the angular velocity data provided by the inertial sensors of the two iHandU_v2 units is guaranteed.

Along this master thesis, the pendulum system was only used to test the inertial data reproducibility of the developed iHandU_v2 units. However, this system has the potential of being used as a calibration tool also. In this particular case, the Amplitude Correlation Coefficient can be used to calibrate the angular velocity data provided by the developed devices with the data provided by the previous version device, which is being currently used in surgery. This prevents for possible errors obtained in the rigidity quantification algorithm, originated by using different devices.

5.5 Improved iHandU Wearable Health System

In this topic is presented the achieved iHandU system as result of the development phase described in 4.

The improved iHandU WHS can be divided in four main parts: the Hardware, the Textile Band, the Android Application and the Web Application (Figure 5.12)

The Hardware part of the system corresponds to the developed iHandU_v2 device. As mentioned in 5.1, some mistakes were made during the development of the iHandU_v2 hardware. In fact, the built hardware does not exactly correspond to the designs presented in 4.3. The built hardware contains the PCB design errors mentioned in 5.1.1 and a voltage circuit to create VCCIO instead of the suggested voltage regulator. Therefore, since the alterations of the PCB design in Altium were already made, according to what is presented in 4.3, it is proposed to produce new PCBs for the iHandU_v2 system. Also, the referred appropriate components must be ordered and soldered in the new boards. With these alterations it is expected that the 85mAh battery be enough to power properly the device. All these specification are also present in Annex I.

Despite the difficulties that emerged, the built device attained the improvements of low cost and inclusion of more advanced technology mentioned in the objectives of this master thesis.

The Textile Band produced in Petratex Company has the purpose of holding the hardware of the system on the patient's hand during DBS surgeries. A follow-up of the band design was made during this project. With the ideas of Eng. Duarte Dias, the achieved band provides the maximum comfort and meets the requirements of surgical environments through its characteristics described in Annex III.

Thus, the developed wearable device comprises the following components welded in a 2.1cm x 2.4cm PCB:

- 9 axis inertial sensor (ICM-20948)
- Resistive force sensors (FSR series 400)
- MCU integrated BLE module (BGM111)
- MCU Programmer (FTSH-105-01-F-D-K)
- Rechargeable battery (RJD2048)
- Battery Holder (Keystone Electronics Corp. 3003)
- Battery Charger (MCP73831T-2ATI/OT)
- Micro USB Connector (USB629105105921)
- Button (CUS - 12TB)
- Voltage Regulator (TPS71533 DCKR)
- Voltage Translator (LSF0204)

With this device is possible to transmit raw data from the three inertial sensors (accelerometer, gyroscope and magnetometer), instead of broadcasting only accelerometer and gyroscope data as in the previous device, and from the two resistive force sensors, through BLE, for the two interfacing parts of the achieved system: Android Application and Web Application.

The Android Application of the previous iHandU system was updated by a member of the BRAIN group to integrate the improved iHandU hardware. In this way, the rigidity changes quantification algorithm of the previous iHandU system can now use data of this new hardware, being able to be part of the iHandU system during DBS surgery. Despite it is receiving and recording data from the five sensors, the Android Application only represents graphically the y-axis gyroscope data of the patient's hand kinematics, needed for rigidity evaluation during DBS surgery, together with the computed percentage of rigidity improvement. Therefore, the android application is intended to be used during DBS surgeries only.

Having this into account, there was the need of developing the fourth and last part of this system: a Web Cross Platform Application. This web application allows for real-time visualization of data from the five sensors implemented in the new hardware and their respective recording in a CSV file. This part of the system acted as a debug platform during the project development, enabling to ensure the reliability of the data through its visualization. Furthermore, it was very useful for the performance of the reproducibility tests, referred in 5.1.

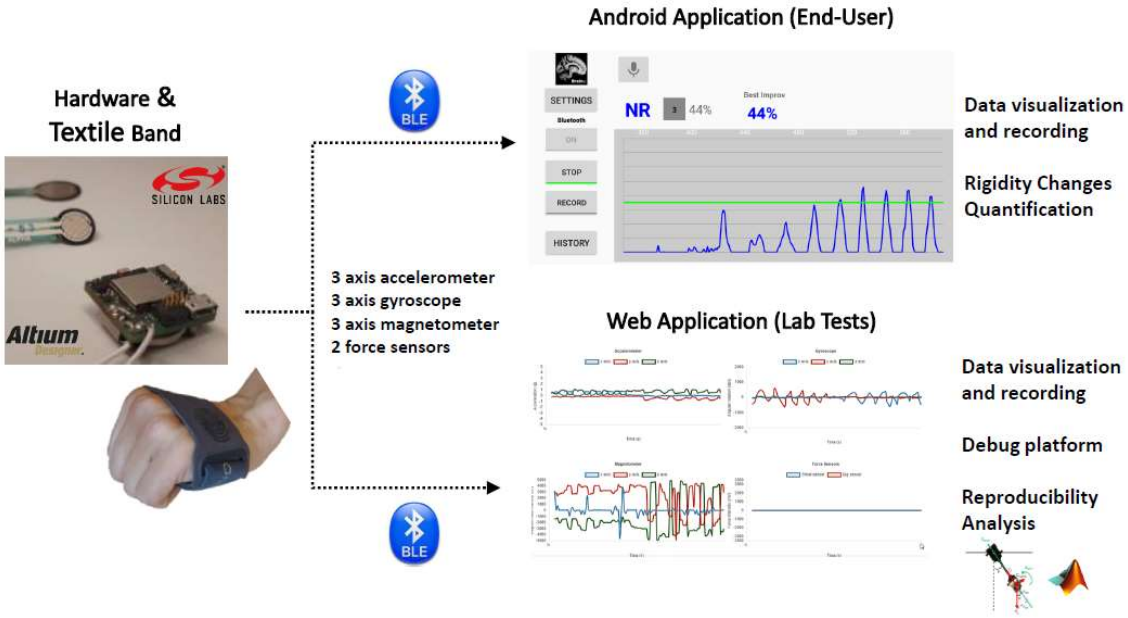

Figure 5.12 - Improved iHandU Wearable Health System.

6

6 Conclusions and Future work

In Biomedical Engineering, we learn the importance of merging technology and health, believing that this union can bring a panoply of advantages for the future. The evolution of wearable devices applied to healthcare has been growing at a high rate. In fact, healthcare specialists truly appreciate this field of technology, perceiving it as an essential support to improve healthcare quality.

The iHandU system has been quite successful in trials that are currently being conducted at Hospital S. João, Porto, Portugal. On BRAIN's side and from the doctors' point of view, it is believed that this system has the potential for not only support doctors during DBS surgery procedures, as well as being used on the patients' follow-up.

During this master thesis, efforts have been made to provide a better contribution for the iHandU device. In comparison to the previous version, the iHandU_v2 device consists in a six times less bulky and almost four times lighter hardware (Figure 6.1) with cutting-edge technology implemented, allowing it to achieve a 13 times reduction of power consumption. Moreover, data from additional sensors (magnetometer and force), besides the already existing data from the accelerometer and gyroscope, are now available in a unique device.

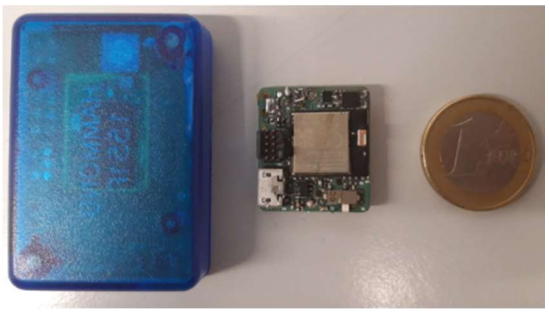

Figure 6.1 - Previous and current versions of the iHandU device.

Another important enhancement in relation to the previous iHandU hardware was the production of the textile band, which was conducted by Eng. Duarte Dias in partnership with Petratex Company. The previous band, did not fulfil the needed requirements to be used in the operating room, neither guaranteed the maximum comfort for the patient. Furthermore, a

calibration and reproducibility system and a web application for data visualization and debug had also enriched the iHandU system.

Though, despite the system with the iHandU_v2 device has not been yet tested in surgery, some improvements may already be suggested, as detailed below.

To start, a new device with no PCB design errors, the ones mentioned in 5.1.1, and with the correct components, replacement of the voltage divider circuit by a voltage regulator, must be produced. With this intention, the PCB designs free of mistakes and with the most appropriated components were already remade, being ready to order.

A doctors' validation of the iHandU_v2 system being used during DBS surgeries must also be performed. Specifically, their input about the band characteristics with the iHandU_v2 device integrated, to ensure the band comfort, easiness in use and surgical environment adaption is of utmost importance. Different positions for the force sensors must be tested in clinical trials, in order to achieve the most profitable placement and disposition of these sensors in the band.

Also, the performance of more rigorous reproducibility tests to the IMUs is suggested. Some characteristics of the pendulum, as its shape and length, must be redesigned in order for its movement to be more in line with what is described in the theoretical equations. In addition, the use of the pendulum as a calibration tool for the iHandU system is also proposed. The Amplitude Correlation Coefficient resulting of the comparison between the theoretical and the previous iHandU device data may be used as reference to calibrate the iHandU_v2 units, thus ensuring data homogeneity with the previous version of device. Moreover, the integration of the reproducibility and calibration tests algorithms could be integrated in the developed Web Application, contributing for a uniform and easy to use system.

Focusing on the rigidity quantification algorithm, it is proposed to test if the inclusion of the new sensors data provided by the developed hardware improves the results of the rigidity quantification algorithm. In fact, there is some research made by BRAIN members on using data fusion algorithms, mentioned in 3.2.4, to represent the hand orientation with data from the three inertial sensors: accelerometer, gyroscope and magnetometer. For now, the iHandU algorithm uses only data from y axis of the gyroscope. What is proposed is to test if the information of the other sensors, including the force sensors, can bring some advantages for the rigidity quantification.

By last, there are some improvements that can still be made on the system hardware and on the textile band. These are discussed in Annex IV due to confidentiality purposes.

Bibliography

[1] M. S. Okun and P. R. Zeilman, Parkinson's Disease: Guide to Deep Brain Stimulation Therapy, 2017. [Online]. Available: https://parkinson.org.

[2] S. K. Patrick, A. A. Denington, M. J. Gauthier, D. M. Gillard, and A. Prochazka, "Quantification of the UPDRS rigidity scale," *IEEE transactions on neural systems and rehabilitation engineering*, vol. 9, no. 1, pp. 31-41, 2001.

[3] P. Costa, M. J. Rosas, R. Vaz, and J. P. Cunha, "Wrist rigidity assessment during Deep Brain Stimulation surgery," in *Engineering in Medicine and Biology Society (EMBC), 2015 37th Annual International Conference of the IEEE*. 2015, pp. 3423-3426: IEEE.

[4] S. Assis, P. Costa, M. J. Rosas, R. Vaz, and J. P. S. Cunha, "An adaptive model approach for quantitative wrist rigidity evaluation during deep brain stimulation surgery," in *Engineering in Medicine and Biology Society (EMBC), 2016 IEEE 38th Annual International Conference of the*. 2016, pp. 5809-5812: IEEE.

[5] E. M. Lopes *et al.*, "iHandU: Towards the Validation of a Wrist Rigidity Estimation for Intraoperative DBS Electrode Position Optimization," in *2019 9th International IEEE/EMBS Conference on Neural Engineering (NER)*. 2019, pp. 449-452: IEEE.

[6] J. P. T. D. S. CUNHA and P. COSTA, "Wrist rigidity assessment device for use in deep brain stimulation surgery," 2016. Patent Application No: WO2016166702A1.

[7] C. O. Oluigbo, A. Salma, and A. R. Rezai, "Deep brain stimulation for neurological disorders," *IEEE reviews in biomedical engineering*, vol. 5, pp. 88-99, 2012. doi: 10.1109/RBME.2012.2197745.

[8] Medtronic. 2018. *Deep Brain Stimulation Systems Healthcare Professionals*. Accessed on: 1st February 2019. [Online]. Available: https://www.medtronic.com

[9] O.-B. Tysnes and A. Storstein, "Epidemiology of Parkinson's disease," *Journal of Neural Transmission*, vol. 124, no. 8, pp. 901-905, 2017. doi: 10.1007/s00702-017-1686-y.

[10] Tanja Schub and O. Avital, "Parkinson Disease," *Cinahl Information Systems*, 2018.

[11] P. s. R. A. Group. *The Glossary of Parkinson's disease*. Accessed on: 1st February 2019. [Online]. Available: http://prag.site

[12] F. v. d. Berg. 2018. *How Does The Brain Control Movement?* Accessed on: 1st February 2018. [Online]. Available: https://www.forbes.com

[13] P. Rizek, N. Kumar, and M. S. Jog, "An update on the diagnosis and treatment of Parkinson disease," *Cmaj,* vol. 188, no. 16, pp. 1157-1165, 2016. doi: 10.1503/cmaj.151179.

[14] Y. Kwon *et al.*, "Quantitative evaluation of parkinsonian rigidity during intra-operative deep brain stimulation," *Bio-medical materials and engineering,* vol. 24, no. 6, pp. 2273-2281, 2014. doi: 10.3233/BME-141040.

[15] M. Clinic. 2018. *Deep brain stimulation (DBS)*. Accessed on: 4th February 2019. [Online]. Available: https://mayfieldclinic.com

[16] E. R. Fahn S, "Unified Parkinson's Disease Rating Scale," *Recent Developments in Parkinson's Disease,* vol. 2, 2006.

[17] Y. Şengül *et al.*, "Essential Tremor and Alexithymia," *Turkish Journal of Neurology,* vol. 24, no. 3, pp. 248-251, 2018. doi: 10.4274/tnd.98216

[18] M. Deborah A Burke. 2018. *Essential Tremor*. Accessed on: 12th January 2019. [Online]. Available: https://emedicine.medscape.com

[19] Y. F. Roy V. Sillitoe, Charles Watson, "Cerebellum," in *The Mouse Nervous System*, G. P. Charles Watson, Luis Puelles, Ed., ed: Academic Press, 2012, pp. 360-397, doi: 10.1016/B978-0-12-369497-3.10011-1.

[20] I. SAS. 2004. *Dentate nucleus*. Accessed on: 4th February 2019. [Online]. Available: https://www.imaios.com

[21] D. Haubenberger and M. Hallett, "Essential tremor," *New England Journal of Medicine,* vol. 378, no. 19, pp. 1802-1810, 2018. doi: 10.1056/NEJMcp1707928.

[22] L. Mertz, "Taking on essential tremor: new tools and approaches offer patients increased treatment options," *IEEE pulse,* vol. 7, no. 3, pp. 20-25, 2016. doi: 10.1109/MPUL.2016.2538481.

[23] R. J. Elble, "The essential tremor rating assessment scale," *J Neurol Neuromed,* vol. 1, no. 4, pp. 34-38, 2016.

[24] B. K. Park *et al.*, "Analysis of viscoelastic properties of wrist joint for quantification of parkinsonian rigidity," *IEEE Transactions on Neural Systems and Rehabilitation Engineering,* vol. 19, no. 2, pp. 167-176, 2011. doi: 10.1109/TNSRE.2010.20.

[25] H. Dai, B. Otten, J. H. Mehrkens, and L. D'Angelo, "A portable system for quantitative assessment of parkinsonian rigidity," in *Engineering in Medicine and Biology Society (EMBC), 2013 35th Annual International Conference of the IEEE*. 2013, pp. 6591-6594: IEEE.

[26] G. A. f. M. Health. *The Elbow*. Accessed on: 14th January 2019. [Online]. Available: http://bjdonline.org

[27] H. Dai, B. Otten, J. H. Mehrkens, L. T. D'Angelo, and T. C. Lueth, "A novel glove monitoring system used to quantify neurological symptoms during deep-brain stimulation surgery," *IEEE Sensors Journal,* vol. 13, no. 9, pp. 3193-3202, 2013. doi: 10.1109/JSEN.2013.2271775.

[28] M. B. Shapiro, D. E. Vaillancourt, M. M. Sturman, L. V. Metman, R. A. Bakay, and D. M. Corcos, "Effects of STN DBS on rigidity in Parkinson's disease," *IEEE Transactions on Neural Systems and Rehabilitation Engineering,* vol. 15, no. 2, pp. 173-181, 2007. doi: 10.1109/TNSRE.2007.896997.

[29] M. Hăgan, A. Constantinescu, and O. Geman, "Tremor analysis in neurological disorders using intelligent clothes," in *E-Health and Bioengineering Conference (EHB), 2015*. 2015, pp. 1-4: IEEE.

[30] N. I. o. N. D. a. Stroke. 2018. *Tremor Fact Sheet*. Accessed on: 14th January 2019. [Online]. Available: https://www.ninds.nih.gov

[31] H. Dai, P. Zhang, and T. C. Lueth, "Quantitative assessment of parkinsonian tremor based on an inertial measurement unit," *Sensors,* vol. 15, no. 10, pp. 25055-25071, 2015. doi: 10.3390/s151025055.

[32] J. P. Giuffrida, D. E. Riley, B. N. Maddux, and D. A. Heldman, "Clinically deployable Kinesia™ technology for automated tremor assessment," *Movement disorders: official journal of the Movement Disorder Society,* vol. 24, no. 5, pp. 723-730, 2009. doi: 10.1002/mds.22445.

[33] A. Salarian, H. Russmann, C. Wider, P. R. Burkhard, F. J. Vingerhoets, and K. Aminian, "Quantification of tremor and bradykinesia in Parkinson's disease using a novel ambulatory monitoring system," *IEEE Transactions on Biomedical Engineering,* vol. 54, no. 2, pp. 313-322, 2007. doi: 10.1109/TBME.2006.886670.

[34] T. Q. Mentzel *et al.*, "Reliability and validity of an instrument for the assessment of bradykinesia," *Psychiatry research,* vol. 238, pp. 189-195, 2016. doi: 10.1016/j.psychres.2016.02.011.

[35] G. Rao *et al.*, "Does This Patient Have Parkinson Disease?," *JAMA,* vol. 289, no. 3, pp. 347-353, 2003. doi: 10.1001/jama.289.3.347.

[36] H. Dai and L. D'Angelo, "A portable system for quantitative assessment of parkinsonian bradykinesia during deep-brain stimulation surgery," in *Advances in Biomedical Engineering (ICABME), 2013 2nd International Conference on*. 2013, pp. 77-80: IEEE.

[37] Farlex. *Pronation*. Accessed on: 14th January 2019. [Online]. Available: https://medical-dictionary.thefreedictionary.com

[38] K. Niazmand, K. Tonn, A. Kalaras, U. M. Fietzek, J.-H. Mehrkens, and T. C. Lueth, "Quantitative evaluation of Parkinson's disease using sensor based smart glove," in *Computer-Based Medical Systems (CBMS), 2011 24th International Symposium on*. 2011, pp. 1-8: IEEE.

[39] B. P. Printy *et al.*, "Smartphone application for classification of motor impairment severity in Parkinson's disease," in *Engineering in Medicine and Biology Society (EMBC), 2014 36th Annual International Conference of the IEEE*. 2014, pp. 2686-2689: IEEE.

[40] H. Dai, H. Lin, and T. C. Lueth, "Quantitative assessment of parkinsonian bradykinesia based on an inertial measurement unit," *Biomedical engineering online,* vol. 14, no. 1, p. 68, 2015. doi: 10.1186/s12938-015-0067-8.

[41] Y. Tian, X. Meng, D. Tao, D. Liu, and C. Feng, "Upper limb motion tracking with the integration of IMU and Kinect," *Neurocomputing,* vol. 159, pp. 207-218, 2015. doi: 10.1016/j.neucom.2015.01.071.

[42] C. Castiblanco, C. Parra, and J. Colorado, "Individual hand motion classification through EMG pattern recognition: Supervise and unsupervised methods," in *Signal Processing, Images and Artificial Vision (STSIVA), 2016 XXI Symposium on*. 2016, pp. 1-6: IEEE.

[43] S. Karimimehr, P. Ghaderi, and M. E. Andani, "Hand kinematics estimation using non-invasive surface sensors: a linear system identification approach," in *Biomedical Engineering (ICBME), 2015 22nd Iranian Conference on*. 2015, pp. 239-244: IEEE.

[44] G. A. G. Ricardez *et al.*, "Wearable Device to Record Hand Motions based on EMG and Visual Information," in *2018 14th IEEE/ASME International Conference on Mechatronic and Embedded Systems and Applications (MESA)*. 2018, pp. 1-6: IEEE.

[45] X. Li, R. Wen, Z. Shen, Z. Wang, K. D. K. Luk, and Y. Hu, "A Wearable Detector for Simultaneous Finger Joint Motion Measurement," *IEEE transactions on biomedical circuits and systems,* vol. 12, no. 3, pp. 644-654, 2018. doi: 10.1109/TBCAS.2018.2810182.

[46] S. Yao, L. Vargas, X. Hu, and Y. Zhu, "A Novel Finger Kinematic Tracking Method Based on Skin-Like Wearable Strain Sensors," *IEEE Sensors Journal,* vol. 18, no. 7, pp. 3010-3015, 2018. doi: 10.1109/JSEN.2018.2802421.

[47] N. Carbonaro, G. Dalle Mura, F. Lorussi, R. Paradiso, D. De Rossi, and A. Tognetti, "Exploiting wearable goniometer technology for motion sensing gloves," *IEEE journal of biomedical and health informatics,* vol. 18, no. 6, pp. 1788-1795, 2014. doi: 10.1109/JBHI.2014.2324293.

[48] S. Ciotti, E. Battaglia, N. Carbonaro, A. Bicchi, A. Tognetti, and M. Bianchi, "A synergy-based optimally designed sensing glove for functional grasp recognition," *Sensors,* vol. 16, no. 6, p. 811, 2016. doi: 10.3390/s16060811.

[49] C.-S. Fahn and H. Sun, "Development of a fingertip glove equipped with magnetic tracking sensors," *Sensors,* vol. 10, no. 2, pp. 1119-1140, 2010. doi: 10.3390/s100201119.

[50] Y. Ma, Z.-H. Mao, W. Jia, C. Li, J. Yang, and M. Sun, "Magnetic hand tracking for human-computer interface," *IEEE Transactions on Magnetics,* vol. 47, no. 5, pp. 970-973, 2011. doi: 10.1109/TMAG.2010.2076.

[51] E. Fujiwara, D. Y. Miyatake, M. F. M. Santos, and C. K. Suzuki, "Development of a glove-based optical fiber sensor for applications in human-robot interaction," in *Proceedings of the 8th ACM/IEEE International Conference on Human-robot Interaction*. 2013, pp. 123-124: IEEE Press.

[52] Y. Koyama, M. Nishiyama, and K. Watanabe, "Smart textile with plain weave structure using hetero-core optical fiber sensor and wool threads," in *2018 International Conference on Intelligent Autonomous Systems (ICoIAS)*. 2018, pp. 18-22: IEEE.

[53] A. F. da Silva, A. F. Gonçalves, P. M. Mendes, and J. H. Correia, "FBG sensing glove for monitoring hand posture," *IEEE Sensors Journal,* vol. 11, no. 10, pp. 2442-2448, 2011. doi: 10.1109/JSEN.2011.2138132.

[54] A. Atrsaei, H. Salarieh, A. Alasty, and M. Abediny, "Human Arm Motion Tracking by Inertial/Magnetic Sensors Using Unscented Kalman Filter and Relative Motion Constraint," *Journal of Intelligent & Robotic Systems,* vol. 90, no. 1-2, pp. 161-170, 2018. doi: 10.1007/s10846-017-0645-z.

[55] N. Ahmad, R. A. R. Ghazilla, N. M. Khairi, and V. Kasi, "Reviews on various inertial measurement unit (IMU) sensor applications," *International Journal of Signal Processing Systems,* vol. 1, no. 2, pp. 256-262, 2013. doi: 10.12720/ijsps.1.2.256-262.

[56] A. H. Moreira, S. Queirós, J. Fonseca, P. L. Rodrigues, N. F. Rodrigues, and J. L. Vilaça, "Real-time hand tracking for rehabilitation and character

animation," in *Serious Games and Applications for Health (SeGAH), 2014 IEEE 3rd International Conference on*. 2014, pp. 1-8: IEEE.

[57] A. Mohan, G. Tharion, R. Kumar, and S. Devasahayam, "An instrumented glove for monitoring hand function," *Review of Scientific Instruments,* vol. 89, no. 10, 2018. doi: 10.1063/1.5038601.

[58] B. O'Flynn *et al.*, "Integrated smart glove for hand motion monitoring," in *The Sixth International Conference on Sensor Device Technologies and Applications*. 2015.

[59] E. L. Schaeffer, D. Y. Liu, J. Guerin, M. Ahn, S. Lee, and W. F. Asaad, "A low-cost solution for quantification of movement during DBS surgery," *Journal of neuroscience methods,* vol. 303, pp. 136-145, 2018. doi: 10.1016/j.jneumeth.2018.03.013.

[60] A. G. Rabelo *et al.*, "Objective Assessment of Bradykinesia Estimated from the Wrist Extension in Older Adults and Patients with Parkinson's Disease," *Annals of biomedical engineering,* vol. 45, no. 11, pp. 2614-2625, 2017. doi: 10.1007/s10439-017-1908-3.

[61] P.-C. Hsiao, S.-Y. Yang, B.-S. Lin, I.-J. Lee, and W. Chou, "Data glove embedded with 9-axis IMU and force sensing sensors for evaluation of hand function," in *2015 37th annual international conference of the IEEE Engineering in Medicine and Biology Society (EMBC)*. 2015, pp. 4631-4634: IEEE.

[62] H. G. Kortier, V. I. Sluiter, D. Roetenberg, and P. H. Veltink, "Assessment of hand kinematics using inertial and magnetic sensors," *Journal of neuroengineering and rehabilitation,* vol. 11, no. 70, 2014. doi: 10.1186/1743-0003-11-70.

[63] A. M. Almassri *et al.*, "Pressure sensor: state of the art, design, and application for robotic hand," *Journal of Sensors,* vol. 2015, 2015. doi: http://dx.doi.org/10.1155/2015/846487.

[64] G. De Pasquale, L. Mastrototaro, L. Pia, and D. Burin, "Wearable system with embedded force sensors for neurologic rehabilitation trainings," in *2018 Symposium on Design, Test, Integration & Packaging of MEMS and MOEMS (DTIP)*. 2018, pp. 1-4: IEEE. doi: 10.1109/DTIP.2018.8394187

[65] S. K. Bahadır, "Identification and Modeling of Sensing Capability of Force Sensing Resistor Integrated to E-Textile Structure," *IEEE Sensors Journal,* vol. 18, no. 23, pp. 9770-9780, 2018. doi: 10.1109/JSEN.2018.2871396.

[66] M. Sakr and C. Menon, "Study on the force myography sensors placement for robust hand force estimation," in *2017 IEEE International Conference on Systems, Man, and Cybernetics (SMC)*. 2017, pp. 1387-1392: IEEE.

[67] D. P. Cotton, P. H. Chappell, A. Cranny, N. M. White, and S. P. Beeby, "A novel thick-film piezoelectric slip sensor for a prosthetic hand," *IEEE sensors journal,* vol. 7, no. 5, pp. 752-761, 2007. doi: 10.1109/JSEN.2007.894912.

[68] Y. Wang, K. Xi, G. Liang, M. Mei, and Z. Chen, "A flexible capacitive tactile sensor array for prosthetic hand real-time contact force measurement," in *2014 IEEE International Conference on Information and Automation (ICIA)*. 2014, pp. 937-942: IEEE.

[69] R. V. A.S. Assis, M.J. Rosas, C. Chamadoira, P. Costa and J.P. Silva Cunha, "O-FUN-16 - A Real-Time Intra-Operatory System For Rigidity Evaluation During Deep Brain Stimulation Surgery," presented at the Neurocirugía, Orlando, FL, USA, 2016. doi: 10.1109/EMBC.2016.7592048

[70] S. Jhajharia, S. Pal, and S. Verma, "Wearable computing and its application," *International Journal of Computer Science and Information Technologies,* vol. 5, no. 4, pp. 5700-5704, 2014.

[71] E. E. Egbogah and A. O. Fapojuwo, "A survey of system architecture requirements for health care-based wireless sensor networks," *Sensors,* vol. 11, no. 5, pp. 4875-4898, 2011. doi: 10.3390/s110504875.

[72] D. Dias and J. Paulo Silva Cunha, "Wearable health devices—vital sign monitoring, systems and technologies," *Sensors,* vol. 18, no. 8, 2018. doi: 10.3390/s18082414.

[73] O. Ogunduyile, O. O. Olugbara, and M. Lall, "Development of wearable systems for ubiquitous healthcare service provisioning," *APCBEE procedia,* vol. 7, pp. 163-168, 2013. doi: 10.1016/j.apcbee.2013.08.028.

[74] T. H. Laine, C. Lee, and H. Suk, "Mobile gateway for ubiquitous health care system using zigbee and bluetooth," in *Innovative Mobile and Internet Services in Ubiquitous Computing (IMIS), 2014 Eighth International Conference on*. 2014, pp. 139-145: IEEE. doi: 10.1109/IMIS.2014.17

[75] V. Custodio, F. Herrera, G. López, and J. Moreno, "A review on architectures and communications technologies for wearable health-monitoring systems," *Sensors,* vol. 12, no. 10, pp. 13907-13946, 2012. doi: 10.3390/s121013907.

[76] T. Hughes-Riley, T. Dias, and C. Cork, "A historical review of the development of electronic textiles," *Fibers,* vol. 6, no. 2, 2018. doi: 10.3390/fib6020034.

[77] R. Negra, I. Jemili, and A. Belghith, "Wireless body area networks: Applications and technologies," *Procedia Computer Science,* vol. 83, pp. 1274-1281, 2016. doi: 10.1016/j.procs.2016.04.266

[78] M. Stoppa and A. Chiolerio, "Wearable electronics and smart textiles: a critical review," *Sensors,* vol. 14, no. 7, pp. 11957-11992, 2014. doi: 10.3390/s140711957.

[79] C. Zysset *et al.*, "Textile integrated sensors and actuators for near-infrared spectroscopy," *Optics express,* vol. 21, no. 3, pp. 3213-3224, 2013.

[80] S.-W. Kang *et al.*, "The Development of an IMU Integrated Clothes for Postural Monitoring Using Conductive Yarn and Interconnecting Technology," *Sensors,* vol. 17, no. 11, pp. 1-10, 2017. doi: 10.3390/s17112560.

[81] X. An and G. Stylios, "A Hybrid Textile Electrode for Electrocardiogram (ECG) Measurement and Motion Tracking," *Materials,* vol. 11, no. 10, 2018. doi: 10.3390/ma11101887.

[82] C. Mummadi *et al.*, "Real-Time and Embedded Detection of Hand Gestures with an IMU-Based Glove," in *Informatics*. 2018, vol. 5, no. 2, p. 28: Multidisciplinary Digital Publishing Institute. doi: 10.3390/informatics5020028

[83] J. Connolly, J. Condell, B. O'Flynn, J. T. Sanchez, and P. Gardiner, "IMU sensor-based electronic goniometric glove for clinical finger movement analysis," *IEEE Sensors Journal,* vol. 18, no. 3, pp. 1273-1281, 2017. doi: 10.1109/JSEN.2017.2776262.

[84] M. Andrejašic, "Mems accelerometers," in *University of Ljubljana. Faculty for mathematics and physics, Department of physics, Seminar*. 2008.

[85] M. T. Todaro, L. Sileo, and M. De Vittorio, "Magnetic field sensors based on microelectromechanical systems (MEMS) technology," in *Magnetic Sensors-Principles and Applications*: InTech, 2012.

[86] M. Kok, J. D. Hol, and T. B. Schön, "Using inertial sensors for position and orientation estimation," vol. 11, Foundations and Trends in Signal Processing: Journal, 2017, pp. 1-153. [Online]. Available.

[87] T. E. o. E. Britannica. *Coriolis force*. Accessed on: 20th January 2019. [Online]. Available: https://www.britannica.com

[88] R. Antonello and R. Oboe, "MEMS Gyroscopes for Consumers and Industrial Applications," in *Microsensors*, P. I. Minin, Ed.: InTech, 2011.

[89] T. B. Amanda Bristow, Stephen Nary, "MEMS Tuning-Fork Gyroscope Final Report."

[90] T. C. Shubham Kandekar, Abhay Chopde, Yashwant Kapgate, "Anatomy of MEMS Capacitive Accelerometer," *International Journal for Research in Applied Science & Engineering Technology (IJRASET),* vol. 6, no. VIII, 2018.

[91] T. K. Bhattacharyya and A. L. Roy, "MEMS piezoresistive accelerometers," in *Micro and smart devices and systems*: Springer, New Delhi, 2014, pp. 19-34, doi: 10.1007/978-81-322-1913-2_2.

[92] A. Albarbar and S. Teay, "MEMS Accelerometers: Testing and Practical Approach for Smart Sensing and Machinery Diagnostics," in *Advanced Mechatronics and MEMS Devices II*: Springer, 2017, pp. 19-40, doi: https://doi.org/10.1007/978-3-319-32180-6_2.

[93] A. Albarbar, A. Badri, J. K. Sinha, and A. Starr, "Performance evaluation of MEMS accelerometers," *Measurement,* vol. 42, no. 5, pp. 790-795, 2009. doi: 10.1016/j.measurement.2008.12.002.

[94] D. T. Tran, "A Piezoresistive Acceleration Sensor: from System to Physical Levels," *Sensors & Transducers,* vol. 145, no. 10, 2012.

[95] G. Yugandhar, G. V. Rao, and K. S. Rao, "Modeling and simulation of piezoelectric MEMS sensor," *Materials Today: Proceedings,* vol. 2, no. 4-5, pp. 1595-1602, 2015. doi: 10.1016/j.matpr.2015.07.086.

[96] K.-Y. K. J.M.W. Brownjohn, N. De Battista,, "Sensor Technologies for Civil Infrastructures," in *Applications in Structural Health Monitoring* vol. 56, J. P. L. M.L. Wang, H. Sohn, Ed., M. L. Wang, J.P. Lynch, H. Sohn ed: Woodhead Publishing, 2014, pp. 207-233.

[97] Y. Cai, Y. Zhao, X. Ding, and J. Fennelly, "Magnetometer basics for mobile phone applications," *Electron. Prod.(Garden City, New York),* vol. 54, no. 2, 2012.

[98] T. E. o. E. Britannica. *Lorentz force*. Accessed on: 20th January 2019. [Online]. Available: https://www.britannica.com

[99] P. webmaster. 2018. *The Hall Effect*. Accessed on: 20th January 2019. [Online]. Available: https://www.nist.gov

[100] C. Buffa, G. Langfelder, A. Longoni, A. Frangi, and E. Lasalandra, "Compact MEMS magnetometers for inertial measurement units," in *Sensors, 2012 IEEE*. 2012, pp. 1-4: IEEE.

[101] A. Edelstein, "Advances in magnetometry," *Journal of Physics: Condensed Matter,* vol. 19, no. 16, p. 165217, 2007. doi: 10.1088/0953-8984/19/16/165217.

[102] J. Zhao, "A Review of Wearable IMU (Inertial-Measurement-Unit)-based Pose Estimation and Drift Reduction Technologies," in *Journal of Physics: Conference Series*. 2018, vol. 1087, no. 4, pp. 1-7: IOP Publishing. doi: 10.1088/1742-6596/1087/4/042003

[103] C. G. C. B. M. L. T.H., "Coordinate Systems and Transformations," Unmanned Rotorcraft Systems, Springer, Ed., 2011. [Online]. Available.

[104] S. Zhang, S. Yu, C. Liu, X. Yuan, and S. Liu, "A dual-linear kalman filter for real-time orientation determination system using low-cost MEMS sensors," *Sensors,* vol. 16, no. 264, 2016. doi: 10.3390/s16020264.

[105] G. Cai, B. M. Chen, and T. H. Lee, "Coordinate Systems and Transformations " in *Unmanned rotorcraft systems*, ed: Springer, London, 2011, doi: 10.1007/978-0-85729-635-1_2.

[106] H. Fourati, N. Manamanni, L. Afilal, and Y. Handrich, "Complementary observer for body segments motion capturing by inertial and magnetic sensors," *IEEE/ASME Transactions on Mechatronics,* vol. 19, no. 1, pp. 149-157, 2014. doi: 10.1109/TMECH.2012.2225151.

[107] S. Zhang, W. Jin, and Y. Zhang, "Implementation and complexity analysis of orientation estimation algorithms for human body motion tracking using low-cost sensors," in *Frontiers of Sensors Technologies (ICFST), 2017 2nd International Conference on*. 2017, pp. 49-54: IEEE.

[108] J. L. Marins, X. Yun, E. R. Bachmann, R. B. McGhee, and M. J. Zyda, "An extended Kalman filter for quaternion-based orientation estimation using MARG sensors," in *Intelligent Robots and Systems, 2001. Proceedings. 2001 IEEE/RSJ International Conference on*. 2001, vol. 4, pp. 2003-2011: IEEE.

[109] L. D. Tran, "Data Fusion with 9 Degrees of Freedom Inertial Measurement Unit To Determine Object's Orientation," ed, 2017.

[110] F. Leens. (2009) An Introduction to I2C and SPI Protocols. *IEEE Instrumentation & Measurement Magazine*.

[111] F. Leens, "An introduction to I 2 C and SPI protocols," *IEEE Instrumentation & Measurement Magazine,* vol. 12, no. 1, pp. 8-13, 2009.

[112] E. Garage. *Comparison between serial communication protocols (SPI, I2C & USART)*. Accessed on: 24th January 2019. [Online]. Available: https://www.engineersgarage.com

[113] Elprocus. *Overview on Electronic Communication Protocols*. Accessed on: 24th January 2019. [Online]. Available: https://www.elprocus.com

[114] J. Beningo. 2015. *USART vs UART: Know the difference*. Accessed on: 12th September 2019. [Online]. Available: https://www.edn.com

[115] Elprocus. *AVR Microcontroller (Atmel 8) Serial Communication USART Configuration*. Accessed on: 12th September 2019. [Online]. Available: https://www.elprocus.com

[116] S. Labs, "Designing for Bluetooth Low Energy Applications," Available: www.silabs.com

[117] K. Townsend, "Introduction to Bluetooth Low Energy," *Adafruit Industries,* 2018.

[118] PCBcart. *Printed Circuit Board Introduction & PCB Types*. Accessed on: 24th August 2019. [Online]. Available: https://www.pcbcart.com

[119] BuildElectronicCircuits. 2018. *Kicad vs Eagle – Which one is best? [2018 comparison]*. Accessed on: 24th August 2019. [Online]. Available: https://www.build-electronic-circuits.com

[120] S. F. Circuits. *The Ultimate PCB Design Software Comparison Guide Comparing the Top 6 PCB CAD Programs*. Accessed on: 24th August 2019. [Online]. Available: https://www.sfcircuits.com

[121] B. University. 2010. *Is Lithium-ion the Ideal Battery?* Accessed on: 26th February. [Online]. Available: https://batteryuniversity.com

[122] P. Mohazzabi and S. P. Shankar, "Damping of a simple pendulum due to drag on its string," *Journal of Applied Mathematics and Physics,* vol. 5, no. 1, pp. 122-130, 2017. doi: 10.4236/jamp.2017.51013.

[123] K. Academy. 2018. *What is torque?* Accessed on: 10th August 2019. [Online]. Available: https://study.com

[124] E. Gandino, S. Marchesiello, A. Bellino, A. Fasana, and L. Garibaldi, "Damping effects induced by a mass moving along a pendulum," *Shock and Vibration,* vol. 2014, 2014. doi: 10.1155/2014/314527.

[125] L. A. Ladino and H. S. Rondón, "Determining the damping coefficient of a simple pendulum oscillating in air," *Physics Education,* vol. 52, no. 3, 2017. doi: 10.1088/1361-6552/aa6431.

[126] S. S. Kolukula. 2011. *Simulation of Nonlinear Simple Pendulum*. Accessed on: 28th August 2019. [Online]. Available: https://www.mathworks.com

[127] T. P. Classroom. *Pendulum Motion*. Accessed on: 25th September 2019. [Online]. Available: https://www.physicsclassroom.com

[128] M. Lieberherr, "Figuring the acceleration of the simple pendulum," *The Physics Teacher,* vol. 49, no. 9, pp. 576-577, 2011. doi: 10.1119/1.3661108.

[129] W. Kenton. 2019. *Economies of Scale*. Accessed on: 21st August 2019. [Online]. Available: https://www.investopedia.com

[130] foglerit. 2012. *how to find out the scaling factors to match two curves in matlab?* Accessed on: 22nd August 2019. [Online]. Available: https://stackoverflow.com

Annex I iHandU_v2 Production Documentation

Accounting for the possibility of reproducing other iHandU_v2 units, this annex provides the documentation about the developed hardware and firmware of the iHandU_v2 device. This information allows a quick understanding of the produced device and, therefore, its easier reproduction.

Hardware Documentation

In order to reproduce the iHandU_v2 hardware, the following information are needed:

- Bill of Materials
- Schematics
- PCB designs
- Gerber files
- Assembly Designs

These documents are available in https://drive.inesctec.pt/s/WQefzXpPGMMZfZ8

Firmware Documentation

The iHandU_v2 device firmware was developed in the Simplicity Studio IDE provided by Silicon Labs Company. The code is available in https://drive.inesctec.pt/s/g5NNjmsHQD9E2jA

To load the code on the iHandU_v2 device, the Blue Gecko Module Wireless Starter Kit, provided by Silicone Labs Company must be used, by following the next steps:

1. Connect the iHandU_v2 device to the main board, using the debug cable. And power the board by connecting it to the computer through an USB cable.
2. Open the Simplicity Studio IDE in the Simplicity IDE tab.
3. Build and flash the code.

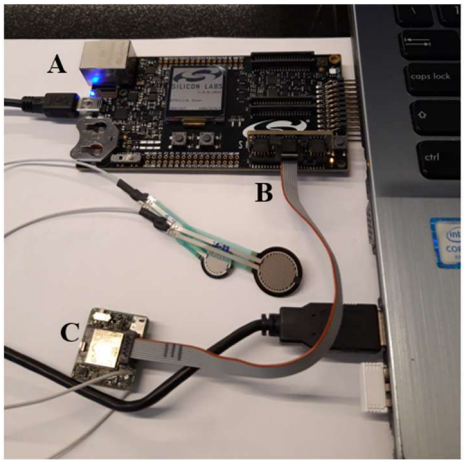

Figure I.1 - System setup to load the firmware on the iHandU_v2 device.

Annex II Reproducibility Tests Guidelines

When aiming to perform a large scale production of a system, it is of utmost importance to guarantee the system reproducibility, i.e. it must be ensured that all the developed systems will have the same behaviour when under identical conditions. Therefore, after developing several iHandU_v2 units, reproducibility tests of their inertial data (linear acceleration and angular velocity) must be executed.

In order to perform these tests, a pendulum, from which the movement characteristics are known, was constructed. The developed iHandU_v2 units must be subject to the pendulum movement and their linear acceleration and angular velocity data must be compared with the theoretical one in a Matlab algorithm developed for this purpose. The algorithm will present as output, two comparison factors, referred in 5.4.1, between the theoretical and the experimental data. A successful reproducibility test occurs when the comparison factors of the tested units are similar.

Assembly

1. Mount the pendulum system in a vertical support.
2. Glue the cardboard with the angles marked from -90° to 90° to the wooden board and aligning the 0° position with the triangular tip of the pendulum.
3. Place the iHandU_v2 unit in a vertical position allowing further small adjustments (Secure the device using an elastic that can be attached to the pendulum hooks).
4. Turn on the device and connect it to the web platform interface according to the instructions described on topic: BLE communication with the iHandU_v2 device.
5. Visualizing the real-time data, adjust the device position until achieve a linear acceleration of one in the y axis of the accelerometer.

The device is now ready for pendulum testing. Follow the steps mentioned on the Pendulum Movement Performance topic.

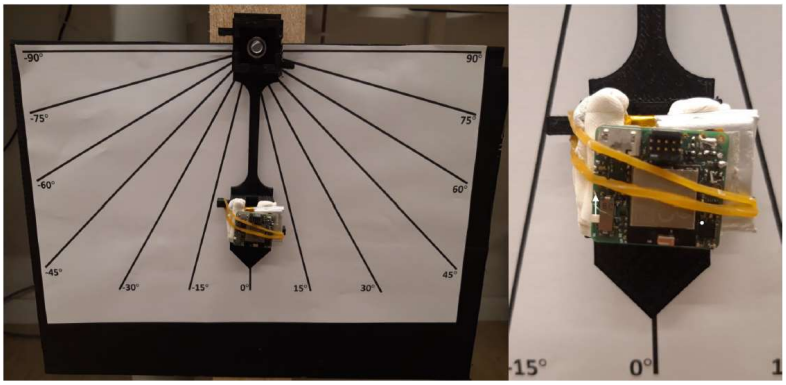

Figure II.1 - Assembly of the pendulum system.

BLE communication with the iHandU_v2 device

1. Go to the Bluetooth Internals page on the chrome browser.
   Link: chrome://bluetooth-internals/#devices
2. Click 'Start Scan'. A list of the visible devices will appear.
3. Find the iHandU_v2 device, named iHandU_v2, and click inspect. A page with a status box of the device presenting its name, address, GATT connection status, RSSI signal and services will be opened. The device is connected when it appears Connected in the status box.
4. Open the Web Application interface to observe in real time and to download the iHandU_v2 sensors data.
   Available in: https://drive.inesctec.pt/s/nrMdsnRnaP6QSFC
5. At the bottom left of the page, click 'Connect'. A list of the visible Bluetooth devices to connect will show up.
6. Select the iHandU_v2 device and click 'Synchronize'. The device is now transmitting.

Pendulum Movement Performance

1. Move the triangular tip of the pendulum to the 90° position of the cardboard and release the pendulum.
2. When the pendulum stops, click 'Disconnect' on the Web Application interface (click also the 'Disconnect' button on the Bluetooth Internals web page, to stop communicating with the device).
3. Click 'Download Values' to download the sensors data in a CSV format.
4. Open the Matlab algorithm to perform the comparison of the download linear acceleration and angular velocity values with the respective pendulum theoretical values.
   Available in: https://drive.inesctec.pt/s/oC5obZDqxoHz62H
5. Copy the downloaded CSV file with the sensors data, named 'DeviceValues', to the same folder of the Matlab files.
6. Open the Main Matlab file and run its first section.
7. Check the comparison factors for linear acceleration values (a and b) and for angular velocity values (c and d):
   a. AccelOscErrorMean & AccelOscErrorSD
   b. AccelAmpCoefMean & AccelAmpCoefSD
   c. GyroOscErrorMean & GyroOscErrorSD
   d. GyroAmpCoefMean & GyroAmpCoefSD

Annex III Textile Band Development (Confidential)

In this annex a detailed description about the development of the textile band is presented. The textile development was made in partnership with Petratex Company based on the ideas of Eng. Duarte Dias, a member of the BRAIN group. A follow up of the referred development was made during this master thesis, since the band must be adapted to developed hardware.

The textile materials used to produce the band were suggested by the Petratex specialists. On the patient side, i.e. on the side that is in contact with the patient's hand, the band is made of cotton, conferring high comfort to the patient. Oppositely, on the doctor side, side in contact with the doctor's hand, the band is made of polyamide giving it the needed elasticity.

Six iterations of the band were sketched. Once the new hardware was not ready yet, the iterations were intended for the first version hardware of the iHandU system. However, it was already included a place to add the force sensors to the system.

Each iteration of the band suffered several modifications after being tested in surgery. These modifications were based on the ideas of Eng. Duarte Dias, who accounted with the opinion of two colleagues who follow the surgeries weekly and with the doctors input. Moreover, it were studied numerous recorded videos where the bands were being used during surgeries with different doctors. While watching these videos, it was concluded that doctors not only are not consistent in the way they grab the patients' hand, as also they not always perform the same movement to evaluate the wrist rigidity. Hence, the production of textile band that unconsciously impose a universal method to doctors grab the patients' hand and perform the evaluation movement was intended. Some details in the design of the band can help in the achievement of this objective.

Despite the inconsistency in grabbing the patient's hand, Figure III.1 shows the most common performed grabbing of the doctors in Hospital S. João, Porto, Portugal. Therefore, the band was designed according to this grabbing.

Figure III.1 - Most common way doctors grab the patient's hand to perform the wrist evaluation during the DBS surgery. (D. Dias 2019, personal communication, May)

To better understand the following description of the band evolution, Figure III.2 presents the format of the band and the reference point used to locate its other components.

The narrow area is to be positioned between the thumb and the index finger. This narrowing was made on the top and on the bottom of the band to allow the band use in the right and left hands.

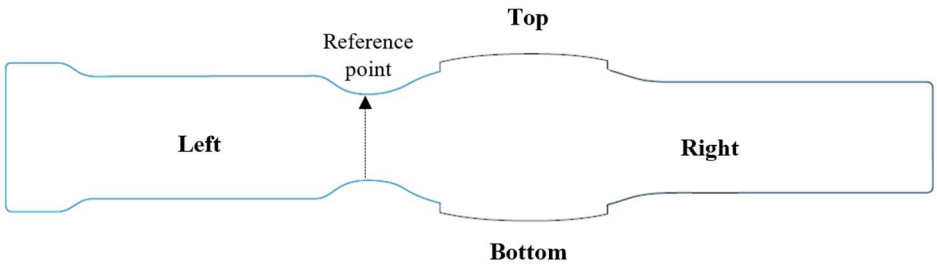

Figure III.2 - References to locate band's components. (D. Dias 2019, personal communication, January)

The first iteration of the band is quite simple (Figure III.3).

On the patient side, the band contains two pockets: one for the PCB and other for the force sensors. The pockets are linked by an opening that crosses the narrow area of the band. The wire of the force sensors will cross this opening to connect to the PCB. The PCB pocket is open on the top side, to allow the insertion of the device. The force sensors pocket, oppositely, is opened laterally.

On the doctor side are the attaching elements: a smaller and a larger piece of male and female, respectively, velcro is on the right and a buckle is positioned at the left end. This buckle is an external metal piece.

During the next iterations several adjustments of size were made. Both, the band and its pockets, suffered alterations until reach the optimal size. Actually, the band length was the most difficult dimension to set, since the production of a band suitable for smaller and bigger hands was intended. Also the velcros dimensions and the distance between them changed several times along the six iterations.

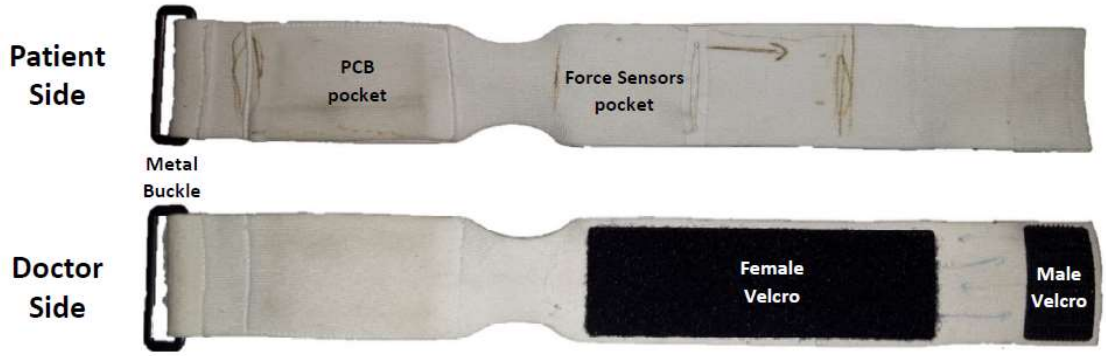

Figure III.3 - First iteration of the band. (D. Dias 2019, personal communication, January)

Next, will be described the remainder main changes of the band from iteration to iteration.

From 1st to 2nd iteration (Figure III.4):

- The PCB and the force Sensors pockets switched sides. This swap was mandatory for the band to close on top of the PCB pocket and not on top of the force sensors pocket, since the later must be sensitive to the touch.
- The entry of the PBC pocket is now lateral. This prevents the hardware from leaving the pocket during the wrist rigidity evaluation. In addition, it was made a hole positioned on the place of the on/off button of the device, to allow turn on and off the device without taking it off the band. The hardware will be inserted in a way that the charger entry will be facing the PCB pocket entry.
- In the patient side were added two silicone strips to prevent the band from leaving the patient hand during the joint evaluation.

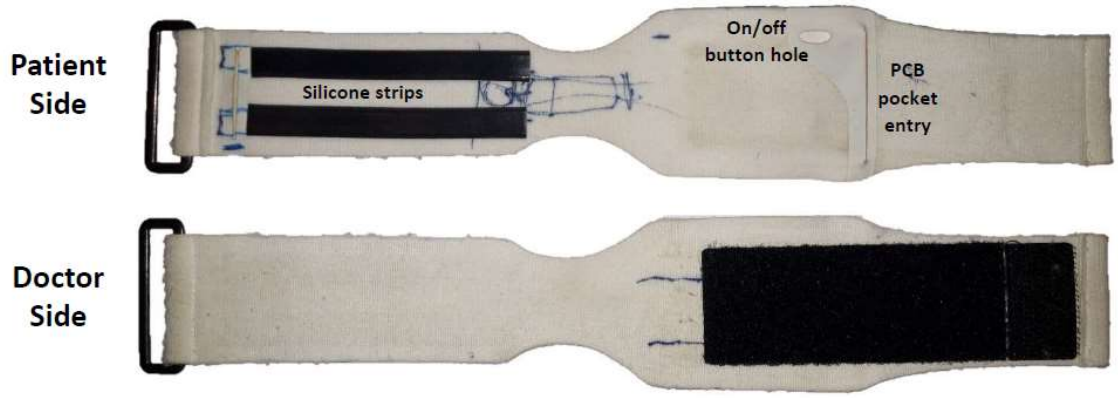

Figure III.4 - Second iteration of the band. (D. Dias 2019, personal communication, February)

From 2nd to 3rd iteration (Figure III.5):

- The entry of the force sensors pocket changed location to the middle allowing the silicone strips extend until the buckle. Therefore, a third silicone strip to prevent even more the band from leaving the patients' hand was added.
- The buckle is now made of PVC and involved by the textile.
- On the right tip, a thick strip was added to make difficult its exit of the band when introduced in the buckle (closed mode).
- An error was made when putting the turn on/off button opening on the bottom of the PCB pocket instead of putting it on the top.
- The corners of the PCB pocket were smoothed to provide a better design and more comfort to the patient when the band is in use.

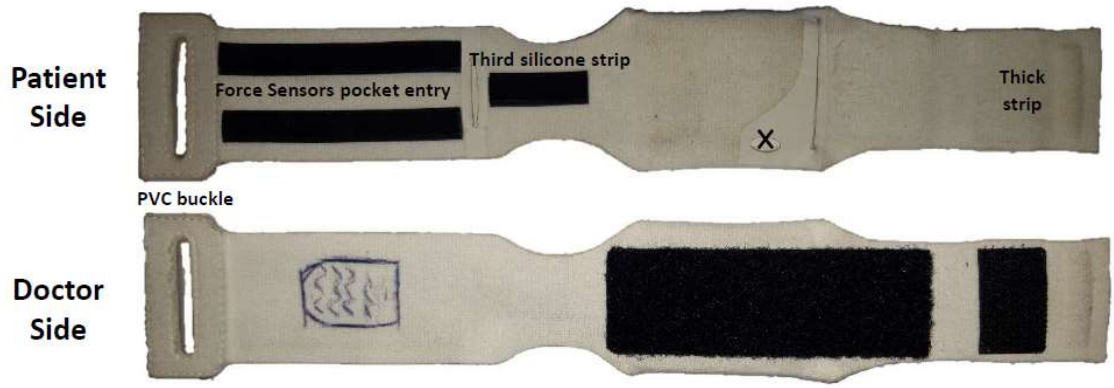

Figure III.5 - Third iteration of the band. (D. Dias 2019, personal communication, March)

From 3rd to 4th iteration (Figure III.6):

- The corners of the buckle and of the left tip of the band were smoothed.
- The buckle is thinner and smaller. Furthermore, its opening changed to a triangular shape. A triangular shape buckle difficult even more the exit of the band tip when the band is closed, without preventing it from exit through the larger side when it is pretended.
- The thickness of the strip on the left tip increased.

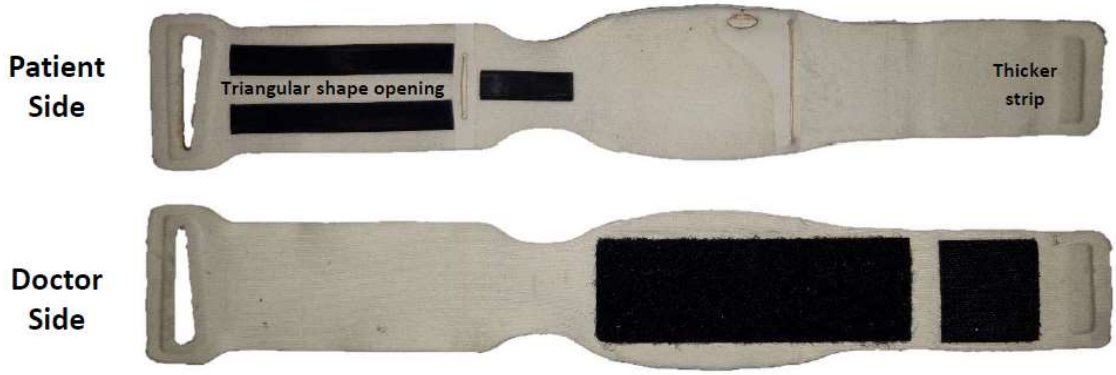

Figure III.6 - Forth iteration of the band. (D. Dias 2019, personal communication, April)

From 4th to 5th iteration (Figure III.7):

- The colour of the band was changed to dark blue to avoid the easily appearance of stains.
- On the doctor side was added a fingerprint made of tiny silicone strips covering the force sensors pocket. This was made to unconsciously take the doctors to put their finger there when grabbing the patient's hand.

Figure III.7 - Fifth iteration of the band. (D. Dias 2019, personal communication, May)

From 5th to 6th iteration (Figure III.8):

- It was added a second fingerprint on top of the force sensors pocket. Thus, doctors can grab the patients' hand with their right or left hand.

Figure III.8 - Sixth iteration of the band. (D. Dias 2019, personal communication, June)

Finally, the final version of the band was achieved with the 6th iteration. This band already contains a label with care instructions. When putting the band, it is important to make sure that the PCB pocket is in the palm of the patient hand and the force sensors pocket is on the back of the patient hand.

The final result of the band was very appreciated by the doctors and worked really well on surgery.

Annex IV Proposed Improved Textile (Confidential)

In this annex, some proposed alterations to perform in a future iteration of the textile band are stated. While some of the proposed alterations are related with the dimensions and characteristics of the PCB pocket, since this PCB is much smaller than its previous version, the others are improvements, suggested by Eng. Duarte Dias, to enhance the usability of the system and become it more technological advanced. With these alterations, it is believed that the system will achieve its best potential, and therefore it will be ready to be used in clinical environment.

Alterations to the PCB pocket:

- Reduce the dimensions of the PCB pocket in a way that it would tightly involve the new PCB.
- Add two transparent windows to the PCB pocket, to be able to see LEDs turning on and off, in different modes of the device.

Other improvements: (D. Dias 2019, personal communication, September)

- Addition of snap buttons to connect the force sensors to the PCB, instead of directly soldering them to the PCB. This would facilitate not only the removal of the hardware from the band when it needs to be washed, as well as the possibility to rapidly switch this hardware for other bands. Thus, three snap buttons will be required: one for VCC Analog voltage (feed voltage of both sensors) and one for each output of the force sensors. The minimal size of snap buttons found is of 7 mm diameter. However, even if the band have to slightly increase size, this technique will benefit the system.
- Replace the co-axial cables that connect the force sensors to the PCB by conductive textile routes. This will make the system more clean, practical and technologically advanced.

Figure IV.1 exhibits how snap buttons and the connection with force sensors would be implemented in a future version of the iHandU device.

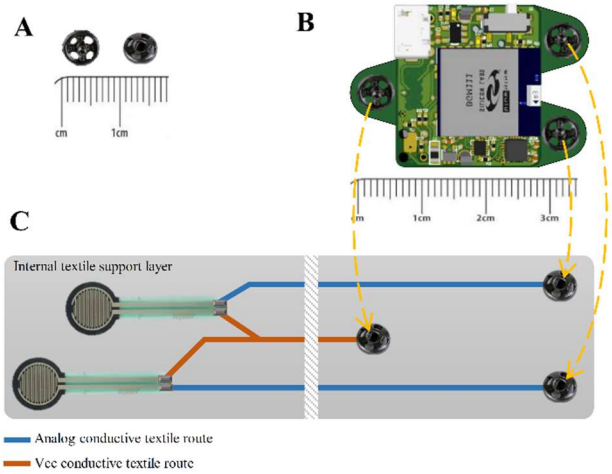

Figure IV.1 - Proposed system for future iHandU version. (D. Dias 2019, personal communication, September)